Temperature monitoring and diagnostic system for a forced-cooled electrochemical energy storage string

Author:
Budihartoputri, Vita Lystianingrum

Publication Date:
2016

DOI:
https://doi.org/10.26190/unsworks/19207

License:
https://creativecommons.org/licenses/by-nc-nd/3.0/au/
Link to license to see what you are allowed to do with this resource.

Downloaded from http://hdl.handle.net/1959.4/56907 in https://unsworks.unsw.edu.au on 2024-05-04

Temperature Monitoring and Diagnostic System for a Forced-cooled Electrochemical Energy Storage String

Vita Lystianingrum

A thesis submitted in partial fulfilment of the requirements
for the degree of
Doctor of Philosophy

School of Electrical Engineering and Telecommunications
Faculty of Engineering
The University of New South Wales
Sydney, New South Wales, Australia

November 2016

PLEASE TYPE

THE UNIVERSITY OF NEW SOUTH WALES
Thesis/Dissertation Sheet

Surname or Family name: Lystianingrum

First name: Vita Other name/s: Vita Lystianingrum Budihartoputri

Abbreviation for degree as given in the University calendar: Ph.D

School: School of Electrical Engineering and Telecommunications Faculty: Faculty of Engineering

Title: Temperature Monitoring and Diagnostic System for a Forced-cooled Electrochemical Energy Storage String

Abstract 350 words maximum: (PLEASE TYPE)

Operating temperature is one of the most critical factors affecting performance and life expectancy of a device. Hence, temperature monitoring and management has been an important area widely researched in various applications, including electrochemical energy storage devices such as batteries and supercapacitors (SCs). In an energy storage string or module consisting of a number of cells, a significant variation in temperature distribution could exist. However, monitoring the whole module temperature is often hindered by hardware and cost limitations, and typically, only a limited number of temperature sensors are employed.

This thesis proposes a model-based temperature monitoring and diagnostic system for a forced-cooled electrochemical energy storage string using a limited number of sensors. While the lumped thermal model for a single cylindrical battery or SC cell has been covered in literature, the multicell model has not been investigated in detail or experimentally validated. Hence, the lumped multicell thermal model of an energy storage string was developed and experimentally validated. The multicell model was subsequently used to study, compare, and assess different observability criteria based on observability Gramian in order to find optimal placement of a limited number of sensors for temperature monitoring.

A multiple model estimator (MME) is also proposed as a viable solution to monitor temperature of all cells as well as to detect and localise an abnormally overheating cell, with the limited number of temperature sensors. Performance of the proposed MME is analysed and experimentally evaluated using an SC string setup.

Lastly, the disturbance detectability criteria based on cross-Gramian matrix were used to analyse optimal placement of a limited number of sensors for the MME-based abnormal overheating diagnostic system. Performance evaluation of the estimation and detection deduced the suitability of particular observability and abnormal overheating detectability criteria for sensor placement in the string.

Declaration relating to disposition of project thesis/dissertation

I hereby grant to the University of New South Wales or its agents the right to archive and to make available my thesis or dissertation in whole or in part in the University libraries in all forms of media, now or here after known, subject to the provisions of the Copyright Act 1968. I retain all property rights, such as patent rights. I also retain the right to use in future works (such as articles or books) all or part of this thesis or dissertation.
I also authorise University Microfilms to use the 350 word abstract of my thesis in Dissertation Abstracts International (this is applicable to doctoral theses only).

[Original signatures are on the master copy version]

…….....…… …….....…… ……..……..…
Signature Witness Date

The University recognises that there may be exceptional circumstances requiring restrictions on copying or conditions on use. Requests for restriction for a period of up to 2 years must be made in writing. Requests for a longer period of restriction may be considered in exceptional circumstances and require the approval of the Dean of Graduate Research.

FOR OFFICE USE ONLY Date of completion of requirements for Award:

Copyright Statement

"I hereby grant the University of New South Wales or its agents the right to archive and to make available my thesis or dissertation in whole or part in the University libraries in all forms of media, now or here after known, subject to the provisions of the Copyright Act 1968. I retain all proprietary rights, such as patent rights. I also retain the right to use in future works (such as articles or books) all or part of this thesis or dissertation. I also authorise University Microfilms to use the 350 word abstract of my thesis in Dissertation Abstract International (this is applicable to doctoral theses only). I have either used no substantial portions of copyright material in my thesis or I have obtained permission to use copyright material; where permission has not been granted I have applied/will apply for a partial restriction of the digital copy of my thesis or dissertation."

[Original signature is on the master copy version]

Signed:……..

Date:……

Authenticity Statement

"'I certify that the Library deposit digital copy is a direct equivalent of the final officially approved version of my thesis. No emendation of content has occurred and if there are any minor variations in formatting, they are the result of the conversion to digital format."

[Original signature is on the master copy version]

Signed:……..

Date:……

Originality Statement

"I hereby declare that this submission is my own work and to the best of my knowledge it contains no materials previously published or written by another person, or substantial proportions of material which have been accepted for the award of any other degree or diploma at UNSW or any other educational institution, except where due acknowledgement is made in the thesis. Any contribution made to the research by others, with whom I have worked at UNSW or elsewhere, is explicitly acknowledged in the thesis. I also declare that the intellectual content of this thesis is the product of my own work, except to the extent that assistance from others in the project's design and conception or in style, presentation and linguistic expression is acknowledged."

[Original signature is on the master copy version]

Signed:.....

Date: .....

Abstract

Operating temperature is one of the most critical factors affecting performance and life expectancy of a device. Hence, temperature monitoring and management has been an important area widely researched in various applications, including electrochemical energy storage devices such as batteries and supercapacitors (SCs). In an energy storage string or module consisting of a number of cells, a significant variation in temperature distribution could exist. However, monitoring the whole module temperature is often hindered by hardware and cost limitations, and typically, only a limited number of temperature sensors are employed.

This thesis proposes a model-based temperature monitoring and diagnostic system for a forced-cooled electrochemical energy storage string using a limited number of sensors. While the lumped thermal model for a single cylindrical battery or SC cell has been covered in literature, the multicell model has not been investigated in detail or experimentally validated. Hence, the lumped multicell thermal model of an energy storage string was developed and experimentally validated. The multicell model was subsequently used to study, compare, and assess different observability criteria based on observability Gramian in order to find optimal placement of a limited number of sensors for temperature monitoring.

A multiple model estimator (MME) is also proposed as a viable solution to monitor temperature of all cells as well as to detect and localise an abnormally overheating cell, with the limited number of temperature sensors. Performance of the proposed MME is analysed and experimentally evaluated using an SC string setup.

Lastly, the disturbance detectability criteria based on cross-Gramian matrix were used to analyse optimal placement of a limited number of sensors for the MME-based abnormal overheating diagnostic system. Performance evaluation of

the estimation and detection deduced the suitability of particular observability and abnormal overheating detectability criteria for sensor placement in the string.

Acknowledgements

First of all, I would like to acknowledge the financial support from the Government of Indonesia through the Directorate General of Higher Education (DIKTI) scholarship for my PhD program at the University of New South Wales (UNSW).

My sincere gratitude goes to my supervisors Prof. Vassilios G. Agelidis and Dr. Branislav Hredzak for the encouragement, assistance, and patience they have provided during my studies. Working with them has given me valuable experience both in academical and non-academical aspects of life.

I would also like to thank Dr. Baburaj Karanayil and Mr. Subash Puthanveetil from the Australian Energy Research Institute (AERI) and the School of Electrical Engineering and Telecommunications (EET) UNSW for assisting me in designing and procurement as well as building and commissioning the experimental setup. Special thanks also go to Dr. Vivien S. Djanali at the Department of Mechanical Engineering, Institut Teknologi Sepuluh Nopember (ITS) Indonesia, for the pleasant discussions and the opportunity to work together on the topic of thermal dynamics and heat transfer.

I also thank all the people at the AERI and the School of EET, UNSW, as well as those at the ITS, for their support and cooperation.

To all my friends and fellow postgraduate students in Sydney, thank you for the friendship and for making this journey enjoyable and memorable.

Finally, very special thanks to my family for their prayer and support. To my husband and fellow PhD candidate Irfan, and my son Hanif, thank you for your endless love, support and understanding. Thank you for struggling together with me all this time.

~ To all lovely children struggling together with their PhD-student mums or dads,

I dedicate this thesis to you ~

Contents

List of Tables

List of Figures

List of Abbreviations and Acronyms

Acronyms	Definition
CFM	Cubic feet per minute
ESR	Equivalent series resistance
Li-ion	Lithium ion
MIMO	Multiple input multiple output
MM	Multiple model
MME	Multiple model estimator
RMS	Root mean square
RMSE	Root-mean-squared error
SC	Supercapacitor
SISO	Single input single output

List of Symbols

Symbol	Definition
a	representation of a mode in the multiple model estimator
$\mathbf{A}$	state matrix
$\mathbf{A}_c$	state matrix (continuous time)
$\mathbf{B}$	input matrix
$\mathbf{B}_c$	input matrix (continuous time)
$\mathbf{B}_d$	disturbance-related input matrix
$\mathbf{C}$	output matrix
C_c	heat capacity of the jelly roll inside the cell [JK^{-1} or J $°C^{-1}$]
$\mathbf{C}_d$	disturbance-related output matrix
c_v	specific heat capacity [$J(kg\ K)^{-1}$]
C_s	heat capacity of the cell casing [JK^{-1} or J $°C^{-1}$]
$\mathbf{d}$	disturbance vector
$\mathbf{G}$	noise gain matrix relating the process noise to the state variables
I	battery cell or string current [A]
$\mathbf{I}$	identity matrix
i	model index
j	cell index
K	convergence factor
k	time step index
$\dot{M}$	mass flow rate [$kg\ s^{-1}$]
m	multiplication of probability and expected disturbance
n	number of states
nd	number of augmented disturbance states
nu	number of input
ny	number of output
p	probability
$\mathbf{Q}_w$	covariance matrix of process noise
$\mathbf{Q}_\xi$	covariance matrix of white noise driving the disturbance
$\mathbf{r}$	residual
R	cell internal resistance [Ω]
$\mathbf{R}$	covariance matrix of measurement noise
R_c	cell lumped thermal conduction resistance [KW^{-1} or $°CW^{-1}$]

R_{cc}	cell connection lumped thermal conduction resistance [KW^{-1} or $°CW^{-1}$]
R_u	cell lumped thermal convection resistance [KW^{-1} or $°CW^{-1}$]
$\mathbf{S}$	residual covariance
T_c	cell core temperature [°C]
T_s	cell surface temperature [°C]
T_f	cell ambient temperature [°C]
$\mathbf{u}$	input vector
$\dot{V}$	volumetric flow rate [$m^3\ s^{-1}$]
$\mathbf{v}$	measurement noise vector
$\mathbf{w}$	process noise vector
$\mathbf{W}_C$	controllability Gramian matrix
$\mathbf{W}_{CO}$	cross-Gramian matrix
$\mathbf{W}_O$	observability Gramian matrix
$\mathbf{x}$	state vector
y (or $\mathbf{y}$)	output (or output vector)

Greek

ξ	white noise driving the disturbance
ρ	density [$kg\ m^{-3}$]
σ	matrix singular values

Chapter 1. Introduction

1.1. Background and motivation

The reliability of any electrical energy system depends on each of its part, and the reliability of each part correspondingly depends on each of its component. Understanding the lifetime issues of a particular component or device of energy system could lead to efforts and solutions to improve system reliability.

For any electrical / electronic components and devices, the operating temperature is one of the most critical factors which affect their performance as well as their life expectancy. Consequently, the performance and the reliability of any bigger system which is comprised of these smaller parts are also contingent to temperature. For that reason, temperature monitoring and management has been an important area which is widely researched, covering various components and applications such as processors or integrated circuits (ICs) [1, 2], power MOSFETs in power electronics converters [3, 4], electric machines and transformers [5, 6], as well as energy storage systems utilising fuel cells [7], batteries, and/or supercapacitors (SCs) [8, 9].

Among different energy storage system, the one with the most varying applications is the electrochemical energy storage type, which includes batteries, capacitors, fuel cells, and their combinations. Battery-based storage uses range from small-scale portable electronic devices, to large-scale systems such as transportation and grid applications [8, 10]. Recently, its counterpart in the electrochemical storage families, SCs, have also gained much attention as the sole energy source [9, 11-13] or as hybrid storage by combinations with battery of fuel cells [14-16].

With this bigger and more important role of the electrochemical storage devices, it is understandable that many researches have been addressing the

lifetime issues of these electrochemical storage systems, more particularly the thermal aspects. Temperature monitoring and management system has been one vital feature which is most likely to be included in any storage management system [17, 18].

While electrochemical storage cells –henceforth will be referred to as simply "cells"– have various voltage and power ratings, it is common that particular applications with high operating voltage require a number of cells to be connected in series. A number of high-voltage battery or SC modules, strings, or stacks are commercially available with an operating voltage up to few hundreds volts for applications in transportation and (uninterruptible power supply) UPS [19-21]. With their relatively high value of current, heat generated from these modules cannot be neglected. Cooling fans are commonly installed with the modules to keep the operating temperature within safe limits. However, air flowing from one side of the module will create temperature non-uniformity across the module during operation. This temperature variation can be significant as it is caused not only by the cooling fan, but also by other factors such as module geometry and cells configuration [18, 22, 23].

Typically, only one or a limited number of temperature sensors are included in a module, located at the spot expected to be of the highest temperature. Although this temperature reading can be considered as representation for the whole module, in fact it is desirable to have the information of each cell's temperature. The temperature non-uniformity relates to aging non-uniformity; hence, the information of actual temperature distribution is useful for the module health diagnostic system. For a module with temperature management system, the temperature variation needs to be known to adjust the cooling system for keeping the variation within the limit [22]. Furthermore, in the case of abnormal or localised overheating in a particular cell, the individual cell temperature information can also be useful for the abnormality detection .

On the other hand, placing temperature sensor in each cell is at present still impractical and uneconomical, as it involves considerable hardware necessities.

One way to solve this challenge is to estimate the module temperature variation based on a thermal model.

This thesis specifically focuses on a temperature monitoring system for a string of cylindrical electrochemical storage cells, with specific additional features such as limited number of temperature sensors and abnormal overheating detection capability.

1.2. Literature review: Temperature monitoring and diagnostics of electrochemical energy storage string

1.2.1. Thermal model of cylindrical electrochemical energy storage string

Prediction and analysis of thermal behaviour of a particular device or element is essential from the point of view of monitoring and diagnostics. There are various techniques for analysing thermal behaviour, such as using lumped-parameter thermal model (or lumped thermal model), finite element analysis (FEA), or numerical techniques such as computational fluid dynamics (CFD). The lumped thermal model uses a thermal network circuit which is analogous to an electrical circuit, with parts such as thermal resistance and thermal capacitance. While FEA and CFD provide solution for the analysis of more complex geometry and heat transfer problem, the high computational cost and time become their disadvantage [8]. On the other hand, lumped thermal model is often used for application requiring simple and fast computation, such as real-time thermal monitoring and management. It also has comparable result to other complex model such as CFD-based model [24]. Hence, the work in this thesis focuses on the lumped thermal model, which will often be referred to as simply "thermal model" in the remainder of this thesis.

Unlike single SC thermal model, SC string / module thermal model has only been covered in few references. Al Sakka *et al.* [9] proposed an inline arranged SC module thermal model with air cooling in axial direction but without experimental results, while in [25] a thermal model for a staggered arranged SC

stack with transversal direction cooling was proposed and validated. In [24], both the lumped thermal model and CFD-based model of forced-cooled battery string with cylindrical cells model were built. The results were compared and were found to be in good agreement. In [18], this lumped thermal model was improved and the state-space form was built. However, the experimental validation of the proposed model was not presented in either of the papers [18, 24].

In [25], as the paper focused on sizing and ageing purpose, only the steady-state temperature was of interest and used for the comparison of the model with the experimental results. For the real-time monitoring and diagnostic purposes, the temperature has to be available at all times.

1.2.2. Sensor placement for electrochemical energy storage string temperature estimation

Optimal sensor placement for estimation purpose has been presented in references either as a brief part or a detailed discussion related to different applications ranging from chemical processes [26-29], architecture and structural engineering [30, 31], as well as for temperature estimation of processors or integrated circuits [1, 32, 33], power plants [34], fuel cell [35], and electrochemical storage systems [8, 18, 36, 37].

Wolf *et al.* [37] classified the placement optimisation criteria into two categories: "open-loop" and "closed-loop". Open-loop criteria are typically based on metrics related to the observation or observability of the system. Closed-loop methods are usually based on metrics related to the performance of the system, such as estimation error or disturbance rejection. Falling into the first category are battery string sensor placement based on the observability matrix in [18], battery cell sensor placement based on observability Gramian-based measure and eigenmode projection method in [36], and battery pack sensor placement based on the modal observability in [37]. While sensor placement based on estimation error for stacked battery pouched cells in [8] falls into the second category.

Very limited references on sensor placement for electrochemical storage string denote further research opportunities in various directions. For example, sensor placement strategy for storage systems with different dimensions and configurations, or evaluating suitability of various observability criteria as the basis for sensor placement.

It is also interesting to note that very few references evaluate the correlation between the aforementioned two optimisation bases. Among the few references is [26], in which the validity of the sensor placement optimised by the observability Gramian criteria are evaluated using the estimator performance, and [38], which analytically established the relationship between the observability Gramian and the error covariance matrix.

1.2.3. Diagnostics in electrochemical energy storage string

Although this thesis specifically focuses on the internal-short-circuit-induced temperature abnormality diagnostics for an electrochemical storage string, a summary on relevant references covering general topic of diagnostics in electrochemical storage is presented to give a broader view.

Generally, two kinds of diagnostic feature are covered by the references researching batteries and/or SCs: state of health (SoH) or simply called health diagnosis, and fault or failure diagnosis. Some events typically considered as fault or failure are overcharge, overdischarge, short circuit, and overtemperature [39-44]. Other conditions which are actually related to the health or age of the device, such as capacity decay or internal resistance increase, are often also referred to as fault or failure modes [45, 46].

The most common method found in the literature for the aforementioned diagnostics is to set a threshold for certain parameter(s) and detect a particular event when the parameter value is exceeding the threshold. For example, in [13, 45], parameters extracted from the SC equivalent circuit such as the internal resistance and capacitance are used as the health (or failure) indicator. Another example is [40] which detects an overcharge or overdischarge condition based on

voltage thresholds. The threshold–detection (or decision) scheme could also be implemented in fuzzy membership functions, such as presented in [47]. For a system represented in state-space model, the threshold of the residual (the difference between the model output and the real system output) could be used as well. A technique called "multiple model" (MM) scheme [42, 48], commonly applied for fault detection and identification (FDI), define a number of modes (models) associated with particular fault modes and associate the system condition to one of the mode by comparing residuals of each mode.

Overcharge, overdischarge, and overtemperature could be detected in a quite straightforward way based on measurement of voltage, current, and/or temperature. However, a short circuit event, especially internal short circuit or "soft-short" fault, could be more challenging to detect directly based on those three basic parameters [39, 41, 43, 49, 50]. There could be situations such as very small short circuit which does not occur continuously [41, 43, 50, 51] or high current situation which might not easily be discriminated from the high operating current [40, 49, 52].

The aforementioned threshold-based detection method is still employed for addressing such soft-short fault. One example is reference [39], where the electrical parameters threshold is set based on the coupled electro-thermal simulation of internal short circuit at different locations and severities in a prismatic large-format Li-ion battery. In [41], the internal short circuit event is approached using external short circuit experiment employing a shorting resistance valued from 1 to 100 Ω to obtain short-circuit-associated parameters from the electrical equivalent circuit, while reference [40] reported the internal short circuit experiment using press drill penetration for setting the electrical and thermal parameters threshold for short circuit detection.

Despite few references have reported short circuit experiments, challenges still exist in this research area. An isolated mechanical short circuit that could emulate internal short circuit leading to a particular incident is difficult to create

[53] and the short circuit event is hardly reproducible for each trial [54]. The experiment itself also poses fire and explosion risk.

Another thing worth to note is that SCs thermal-related failure modes have not been analysed in details in many references, especially compared to batteries. Generally, they are considered less prone to thermal hazard due to their lower energy density, lower internal resistance, and less chemical involved. However, some references mentioned that the batteries and SCs still share some commonality in construction and susceptibility to failure modes including short circuits [55]. Some references also cited few factors of SCs which could be hazardous in a temperature increase and could lead to thermal runaway, such as the use of organic solvents [56] and/or the use of particular electrolyte [57, 58]. Furthermore, with the recent research reporting higher energy density SCs (up to 85 Wh kg^{-1} [59, 60]), it is expected that the related higher thermal risk will become an issue too for SCs application.

From the viewpoint of limited number of sensors for the string parameter monitoring, so far no references have linked the string diagnostic feature with the optimal number and placements of sensor, which is in fact one of the focuses of this thesis.

1.3. Scope and contributions

The types of electrochemical energy storage considered in this thesis are batteries and SCs, while the shape of the cell considered in this thesis is a cylindrical cell. The string is forced-cooled and consists of serially connected cells.

The diagnostic feature considered in this thesis is related only to the detection of cell temperature abnormality in the string.

Hence, the contributions of this thesis are:

1. Proposal and experimental validation of a lumped thermal model of forced-cooled electrochemical storage string consisting of cylindrical cells.
2. Analysis of the observability Gramian as the basis for optimal placement of temperature sensors in a string for temperature monitoring.

3. Proposal to apply multiple model (MM)-based detection method for detecting cell abnormal overheating in a string with a limited number of temperature sensors.
4. Analysis of cross-Gramian as the basis for optimal placement of temperature sensors in the string regarding the cell abnormal overheating detectability.

1.4. List of publications

The material in this thesis has been published in the following publications:

Journal papers:

1. V. Lystianingrum, B. Hredzak, and V. G. Agelidis, "Multiple model estimator based detection of abnormal cell overheating in a Li-ion battery string with minimum number of temperature sensors," Journal of Power Sources, Elsevier, vol. 273, pp. 1171-1181, 1/1/ 2015 [61].
2. V. Lystianingrum, B. Hredzak, V. G. Agelidis, and V. S. Djanali, "On Estimating Instantaneous Temperature of a Supercapacitor String Using an Observer Based on Experimentally Validated Lumped Thermal Model," IEEE Transactions on Energy Conversion, vol. PP, pp. 1-11, 2015 [62].
3. V. Lystianingrum, B. Hredzak, and V. G. Agelidis, "Multiple-Model-Based Overheating Detection in a Supercapacitors String," IEEE Transactions on Energy Conversion, vol. PP, pp. 1-1, 2016 [63].

Conference papers:

1. V. Lystianingrum, V. G. Agelidis, and B. Hredzak, "State of health and life estimation methods for supercapacitors," in Power Engineering Conference (AUPEC), 2013 Australasian Universities, 2013, pp. 1-7 [64].
2. V. Lystianingrum, B. Hredzak, V. G. Agelidis, and V. S. Djanali, "Observability degree criteria evaluation for temperature observability in a battery string towards optimal thermal sensors placement," in

Intelligent Sensors, Sensor Networks, and Information Processing (ISSNIP), 2014 IEEE Ninth International Conf., 2014, pp. 1-6 [65].

3. V. Lystianingrum, B. Hredzak, and V. G. Agelidis, "Abnormal Overheating Detectability Analysis Based on Cross-Gramian for a Superacapacitors String," in Power & Energy Society General Meeting, 2016 IEEE, 2016 [66].

The publications are associated with the part or whole of the chapters of this thesis as follows:

Chapters	**Publications**
Chapter 1. Introduction	[64]
Chapter 2. Thermal Model of Electrochemical Energy Storage String Consisting of Cylindrical Cells	[62]
Chapter 3. Observability-Analysis-Based Optimal Sensor Placement for String Temperature Estimation	[62, 65]
Chapter 4. Multiple-Model-Estimator-Based Detection of Cell Abnormal Overheating	[61]
Chapter 5. Experimentation and Further Exploration of MME-Based Overheating Detection	[63]
Chapter 6. Abnormal Overheating Detectability Analysis Based on Cross-Gramian	[66]

1.5. Thesis outline

This thesis is organised as follows:

- Chapter 1: This chapter explains the background and motivation of this thesis. A concise review covering previous researches relevant to the electrochemical storage temperature monitoring and diagnostics is

given. A list of the scope and contributions of this thesis, as well as published materials from this thesis, are also presented.

- Chapter 2: This chapter discusses the thermal model of both single cell and forced-cooled multicell (string) of electrochemical storage as well as the model experimental validation using a forced-cooled SC string.
- Chapter 3: In this chapter, observability analysis for the purpose of optimal sensor numbers and placement for the string temperature monitoring is discussed. The observability Gramian-based measures (criteria) applicability as the basis for optimal placement of temperature sensors in the string is also evaluated via simulation of battery string and experiment using the SC string.
- Chapter 4: This chapter expands the functionality of string temperature monitoring with limited number of temperature sensors to the ability of abnormal overheating detection. Multiple model estimation (MME) method as well as abnormal overheating modelling as unknown disturbance is proposed.
- Chapter 5: In this chapter, the proposed MME method is evaluated experimentally and further details related to the MME parameters influence to the detection are explored.
- Chapter 6: This chapter links the Gramian matrix-based sensor placement in chapter 3 and the abnormal overheating detection functionality in chapter 4. Instead of observability Gramian matrix, the cross-Gramian matrix is used for analysing disturbance (abnormal overheating) detectability in both battery string and SC string.
- Chapter 7: This chapter summarises and concludes this thesis as well as discusses possible future research directions from this thesis work.

Chapter 2. Thermal Model of Electrochemical Energy Storage String Consisting of Cylindrical Cells

2.1. Introduction

In this chapter, the thermal model of single electrochemical storage cell and its multicell development are presented, specifically for cylindrical battery and SC cells. As can be seen in Figure 2.1 and Figure 2.2, cylindrical battery and SC cells have similar structures. The general assumption for heat generation in both structures is also identical, with which for the high current application the reversible entropic heating is negligible compared to the far more dominant irreversible Joule heating [24, 67]. Thus, from the thermal modelling point of view they could be modelled in a similar way and therefore, in this chapter as well as in the remainder of this thesis, the references related to both cylindrical battery and SC cells are considered.

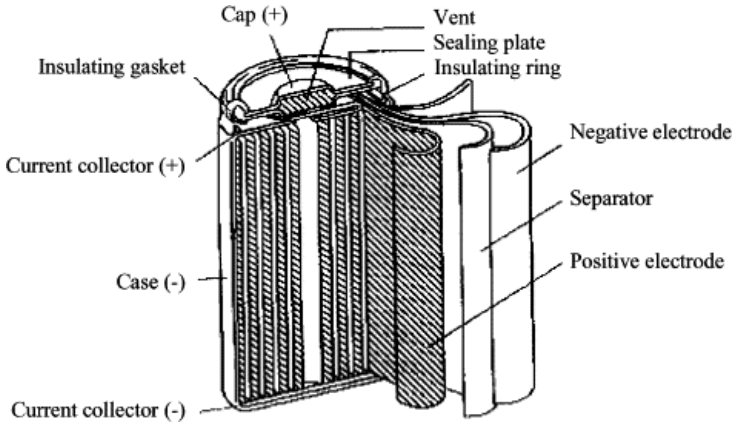

Figure 2.1. Structure of cylindrical battery cell [68][1].

[1]Reprinted with permission for reuse in thesis – print and electronic formats, worldwide distribution. © 2001 Elsevier.

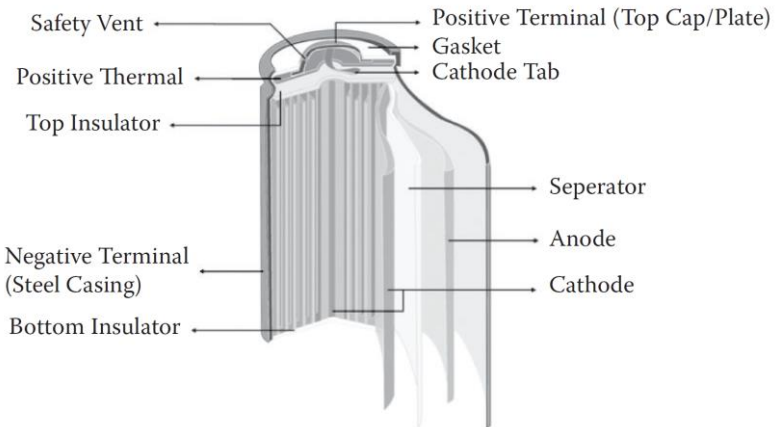

Figure 2.2. Structure of cylindrical SC cell [69][2].

The battery and SC cell considered in this thesis are the 8-Ah A123 32157 $LiFePO_4$/graphite battery and the 650-F Maxwell BCAP0650, respectively. How the two cells compare in terms of dimensions is illustrated in Figure 2.3.

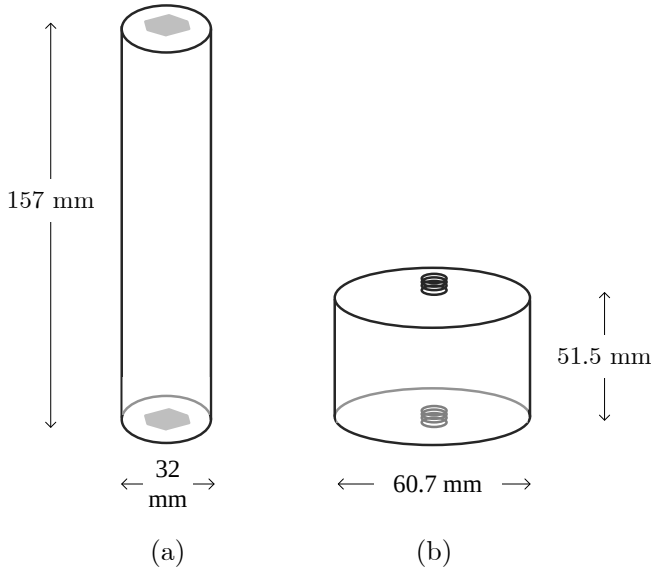

Figure 2.3. (a) Dimensions of A123 32157 battery cell. (b) Dimensions of Maxwell BCAP0650 SC cell.

[2]Reprinted with permission for reuse in thesis – print and electronic formats, worldwide distribution. © 2013 Taylor & Francis, LLC.

The remainder of this chapter is organised as follows. First, the theory of lumped thermal model and its development for string thermal modelling are presented in Section 2.2. The parameters for the string thermal model are then derived in Section 2.3 based on a built setup of a forced-cooled string consisting of eight Maxwell BCAP0650 SC cells, and the model is further validated in Section 2.4. The summary of this chapter is given in Section 2.5.

2.2. Lumped thermal model

In a lumped thermal model, the components of the modelled element are lumped into a number of nodes, in which the thermal properties are supposed to be uniform. More detailed models (high fidelity models) represent an element with high number of nodes and therefore are able to predict detailed temperature distribution throughout an element. However, this understandably comes with the disadvantages of higher computational cost.

In [25], a single SC cell is represented by two thermal nodes: the internal or core temperature node (and represented in the paper as the terminal node) and the surface (case) temperature node. This is similar to the single Li-ion battery cell model in [18, 70], whose elements were lumped into core temperature node and surface temperature node. This two thermal-node lumped model sees that a cylindrical cell consists of two isothermal volumes, i.e., the internal part represented by core temperature node T_c , and the outer part represented by surface temperature node T_s , as shown in Figure 2.4. It has less computational cost compared to the high fidelity model while still provides the ability to capture the critical core temperature [71] This work particularly discusses the two lumped-node cell thermal model, and it will be used to represent both cells shown in Figure 2.3.

T_c is the core temperature node that corresponds to the internal elements of the cell with a heat capacity (thermal capacitance) C_c. T_s is the surface temperature node that corresponds to the casing elements of the cell with a thermal capacitance C_s.

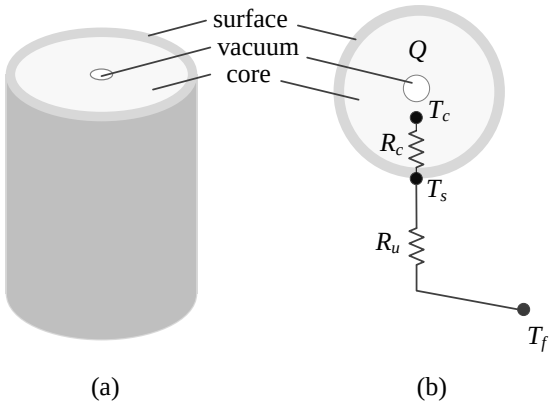

Figure 2.4. (a) A cylindrical cell lumped construction. (b) Corresponding thermal nodes and thermal resistances.

The heat transfer is considered as conduction from the T_c node to the T_s node with a conduction thermal resistance R_c, and by convection from T_c node to the T_f node (ambient temperature node) with a convection thermal resistance R_u. Q is the heat generated by the cell. As heat capacity is proportional to the size of an element, different cell size (such as shown in Figure 2.3) would have different values of the thermal model parameters.

Although the heat generated in the internal part of the cell can be divided into irreversible heating –which is related to Joule (ohmic) losses and reaction heat– and reversible heating –related to entropic–, it is common to approximate the heat generation as exclusively Joule heating, as this is the most dominant heat generated, especially for high current applications such as electric vehicle. This consideration is also taken in this work, in which the heat Q generated by each cell is approximated as the Joule loss I^2R where I is the current and R is the cell internal resistance.

We consider a string consisting of cylindrical cells in an inline (aligned) arrangement. The thermal model is derived from the heat balance equation considering single row of cells in the module shown in Figure 2.5 and two adjacent cells shown in Figure 2.6 [18, 24]. As each cell is connected by a tab, the thermal resistance for cell-to-cell heat conduction via the tab as well as other possible connections is lumped as R_{cc}. In our work, it is assumed that the heat

transfer via the connecting tab dominates this cell-to-cell conduction term. Therefore, in this work, R_{cc} is only related to the connecting tab.

Based on [25] and experimental data given in [72], the T_c node measurement can be represented by the terminal temperature measurement, also considering the fact that the axial thermal resistance is very low [24, 72][3]. Hence, R_{cc} could be modelled either connecting two cells at their two T_c nodes (assuming heat conduction from terminal to terminal); or at their two T_s nodes (assuming heat conduction from surface to surface). We choose the first assumption which better reflects the built experimental setup. Other assumptions for our model are that no balancing circuit is installed and the cooling air flow is constant.

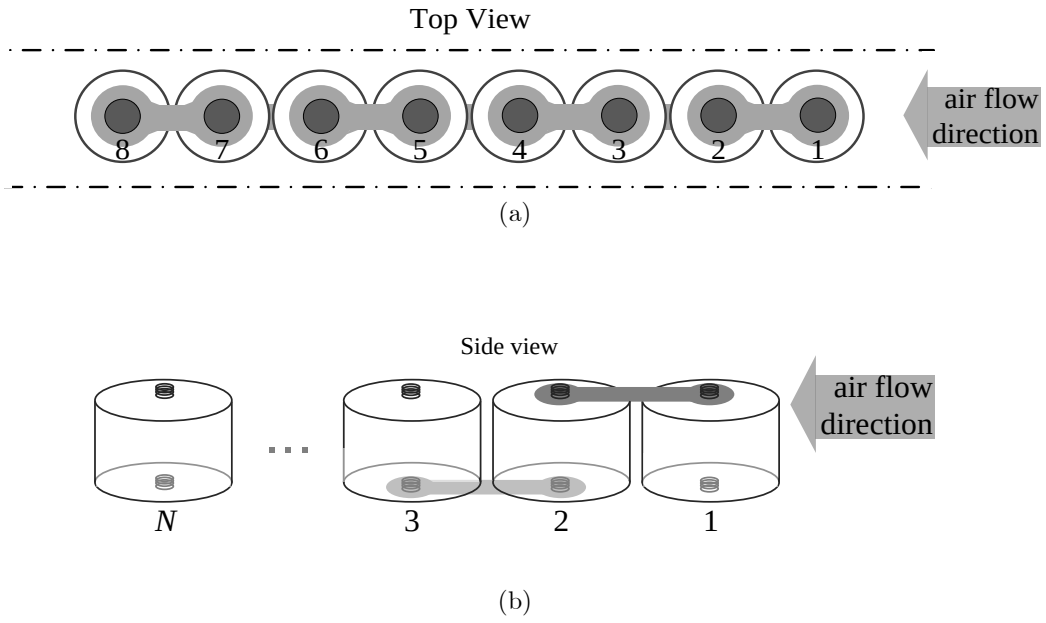

Figure 2.5: Single row of forced-cooled series connected cylindrical storage cells. (a) Top view, showing 8 cells. (b) Side view, showing N cells.

[3] For example, an SC cell with 33-mm outside diameter and 61.5-mm length in [72] has calculated radial and axial thermal conductivity of 0.5 W $m^{-1}K^{-1}$ and 210 W $m^{-1}K^{-1}$, respectively.

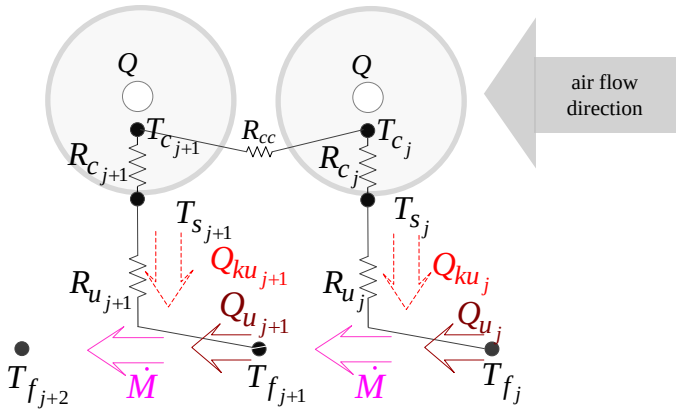

Figure 2.6. Thermal nodes and thermal resistances of two adjacent cells.

The jth cell heat balance equation between heat generated in the internal part and heat transferred to the surface is shown in (2.1), while the heat balance equation between the surface and the ambience is shown in (2.2) [18, 71]:

$$C_c \frac{dT_{c_j}}{dt} = \begin{cases} I^2R - \dfrac{T_{c_j} - T_{s_j}}{R_{c_j}} - \dfrac{T_{c_j} - T_{c_{j+1}}}{R_{cc}}, & j = 1 \\ I^2R - \dfrac{T_{c_j} - T_{s_j}}{R_{c_j}} - \dfrac{T_{c_j} - T_{c_{j-1}}}{R_{cc}} - \dfrac{T_{c_j} - T_{c_{j+1}}}{R_{cc}}, & j = 2, \ldots, N-1 \\ I^2R - \dfrac{T_{c_j} - T_{s_j}}{R_{c_j}} - \dfrac{T_{c_j} - T_{c_{j-1}}}{R_{cc}}, & j = N \end{cases} \quad (2.1)$$

$$C_s \frac{dT_{s_j}}{dt} = \frac{T_{c_j} - T_{s_j}}{R_{c_j}} - \frac{T_{s_j} - T_{f_j}}{R_{u_j}} \quad (2.2)$$

As for the heat balance equation related to coolant (fluid) stream flowing over a cell, we consider Q_{ku_j}, the heat taken from the jth cell via convection (i.e., the $\left(T_{s_j} - T_{f_j}\right) / R_{u_j}$ part in (2.2)) and Q_{u_j}, the heat transferred by the flow from an ambient temperature node T_{f_j}, also shown in Figure 2.6. The heat balance equation can be given as [24, 73]:

$$Q_{ku_j} + Q_{u_j} = Q_{u_{j+1}} \quad (2.3)$$

where

$$Q_{u_{j+1}} - Q_{u_j} = \left(\rho\, c_p \dot{V}\right)\left(T_{f_{j+1}} - T_{f_j}\right) = \left(\dot{M}\, c_p\right)\left(T_{f_{j+1}} - T_{f_j}\right) \tag{2.4}$$

ρ is the air density, c_p is the air specific heat capacity, $\dot{V}$ is the air volumetric flow rate, and $\dot{M}$ is the air mass flow rate, all related to the cooling air.

Combining (2.3) and (2.4) yields

$$\begin{aligned} T_{f_{j+1}} &= T_{f_j} + Q_{ku_j} \cdot \frac{1}{\dot{M}\, c_p} \\ &= T_{f_j} + \frac{T_{s_j} - T_{f_j}}{R_{u_j} \dot{M}\, c_p} \end{aligned} \tag{2.5}$$

To analyse the string thermal behaviour, the thermal model in the mathematical equations form could be solved. Alternatively, a corresponding thermal network could be built and simulated in an electric circuit simulator such as SPICE or Simulink, as the network is based on the electric circuit analogy. The analogy of thermal and electrical parameters is listed in Table 2.1, while the corresponding thermal network of the N-cell string is shown in in Figure 2.7.

To the author's knowledge so far, thermal network representation of the heat transfer by coolant flow, particularly transversal flow considered in this thesis, has not been explicitly shown or discussed in the references related to lumped thermal model of the electrochemical storage string [18, 24, 25, 71]. In Figure 2.7, this heat transfer is modelled as a current-controlled voltage source with the value of $Q_{ku_j} \cdot \frac{1}{\dot{M}\, c_p}$. This is based on the fact that the coolant flow is causing temperature difference between T_{f_j} and $T_{f_{j+1}}$ nodes, and this temperature difference is caused by Q_{ku_j} (i.e. heat-flow-controlled temperature difference). The same representation approach was proposed and used in thermal modelling of other devices [74-77], and it is concluded here that this representation is also suitable for the electrochemical storage string thermal modelling. The thermal network in Figure 2.7 has been built and tested in Simulink using the same validation date as in Section 2.4 and gave the same validation result.

Table 2.1. Analogy of thermal and electrical parameters.

Thermal parameters	Electrical parameters
Heat flux [W]	Current [A]
Temperature difference [K or °C]	Potential difference [V]
Heat capacity (thermal capacitance) [JK^{-1} or $J\ °C^{-1}$]	Electrical capacitance [C]
Thermal resistance [KW^{-1} or $°CW^{-1}$]	Electrical resistance [Ω]

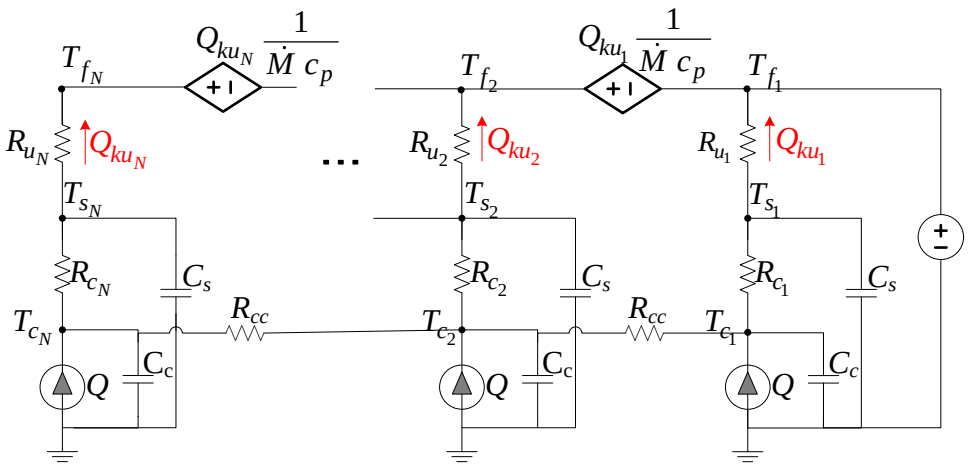

Figure 2.7. Lumped-parameter thermal model of a string consisting of N cells in thermal network form (referring to Figure 2.5, cell 1 is at the right side and cell N is at the left side).

Alternatively, the thermal model can be built in the state-space model form, which is the model used in the remainder of the thesis. The state-space model (as also presented in [18, 71]) is as follows[4]:

$$\dot{\mathbf{x}} = \mathbf{A}_c\mathbf{x} + \mathbf{B}_c\mathbf{u}, \quad \mathbf{y} = \mathbf{C}\mathbf{x} \tag{2.6}$$

[4]In this thesis, subscript "c" in the notation of matrices **A** and **B** denotes "continuous time" and is used to distinguish them to their discrete-time counterparts (matrices **A** and **B**).

where

$$\mathbf{x} = \begin{bmatrix} T_{c_1} & T_{s_1} & T_{c_2} & T_{s_2} & \dots & T_{c_N} & T_{s_N} \end{bmatrix}^T \tag{2.7}$$

$$\mathbf{u} = \begin{bmatrix} I^2 & T_{f_1} \end{bmatrix}^T \tag{2.8}$$

$$\mathbf{B}_c = \begin{bmatrix} \frac{R}{C_c} & 0 \\ 0 & \frac{1}{R_{u_1} C_s} \\ \frac{R}{C_c} & 0 \\ 0 & \frac{1}{R_{u_2} C_s}\left(1 - \frac{1}{R_{u_1} C_f}\right) \\ \vdots & \vdots \\ \frac{R}{C_c} & 0 \\ 0 & \frac{1}{R_{u_N} C_s}\prod_{i=1}^{N-1}\left(1 - \frac{1}{R_{u_i} C_f}\right) \end{bmatrix} \tag{2.9}$$

$$
\mathbf{A}_c = \begin{bmatrix}
-\left(\frac{1}{R_{c_1}C_c} + \frac{1}{R_{cc}C_c}\right) & \frac{1}{R_{c_1}C_c} & 0 & \frac{1}{R_{cc}C_c} & \cdots & 0 & 0 \\
\frac{1}{R_{c_1}C_s} & -\left(\frac{1}{R_{c_1}C_s} + \frac{1}{R_{u_1}C_s}\right) & 0 & 0 & \cdots & \cdots & 0 \\
\frac{1}{R_{cc}C_c} & 0 & -\left(\frac{1}{R_{c_2}C_c} + \frac{2}{R_{cc}C_c}\right) & \frac{1}{R_{c_2}C_c} & \cdots & \cdots & 0 \\
0 & \frac{1}{R_{u_1}R_{u_2}C_fC_s} & \frac{1}{R_{c_2}C_s} & -\left(\frac{1}{R_{c_2}C_s} + \frac{1}{R_{u_2}C_s}\right) & \cdots & \ddots & \vdots \\
\vdots & \vdots & \vdots & \vdots & \cdots & -\left(\frac{1}{R_{c_N}C_c} + \frac{1}{R_{cc}C_c}\right) & \frac{1}{R_{c_N}C_c} \\
0 & 0 & 0 & 0 & \cdots & \frac{1}{R_{c_N}C_s} & -\left(\frac{1}{R_{c_N}C_s} + \frac{1}{R_{u_N}C_s}\right)
\end{bmatrix}
$$

(2.10)

The output vector **y** corresponds to state vector **x** via the output matrix **C**. The **C** matrix relates to the measurement of particular states (e.g. temperature sensor measuring particular temperature nodes). Whether a temperature node is measured or not is indicated in the **C** matrix as "1" or "0", respectively. The **C** matrix of an N-cell string will have $2N$ columns and the number of rows as many as the number of measurements. For example, the **C** matrix of a 2-cell string with measurement of the surface temperature of cell 1 and cell 2 is

$$\mathbf{C} = \begin{bmatrix} 0 & 1 & 0 & 0 \\ 0 & 0 & 0 & 1 \end{bmatrix} \tag{2.11}$$

Hence, for the analysis of optimal sensor placement in the subsequent chapters, the thermal model in state-space form would be useful and thus would be used throughout the thesis.

2.3. Thermal model parameters

2.3.1. Supercapacitor string setup

The experimental setup for validating the thermal model consists of eight serially connected 650-F Maxwell BCAP0650 SC cells. Three thermocouples are placed in each cell measuring nodes T_c, T_s, and T_f. The core temperature node T_c measurement is represented by the terminal temperature measurement, considering the fact that the axial thermal resistance is very low [24, 25, 72]. The string is enclosed and a fan is installed at one side of the enclosure. The SC testing system Arbin BT-ML is controlled by a personal computer. The picture of the built setup and the dimensions are shown in Figure 2.8 and Figure 2.9, respectively. The general specifications of the SC can be found in Table 2.2. For a complete specification and explanation list, please refer to the SC datasheet ([78]).

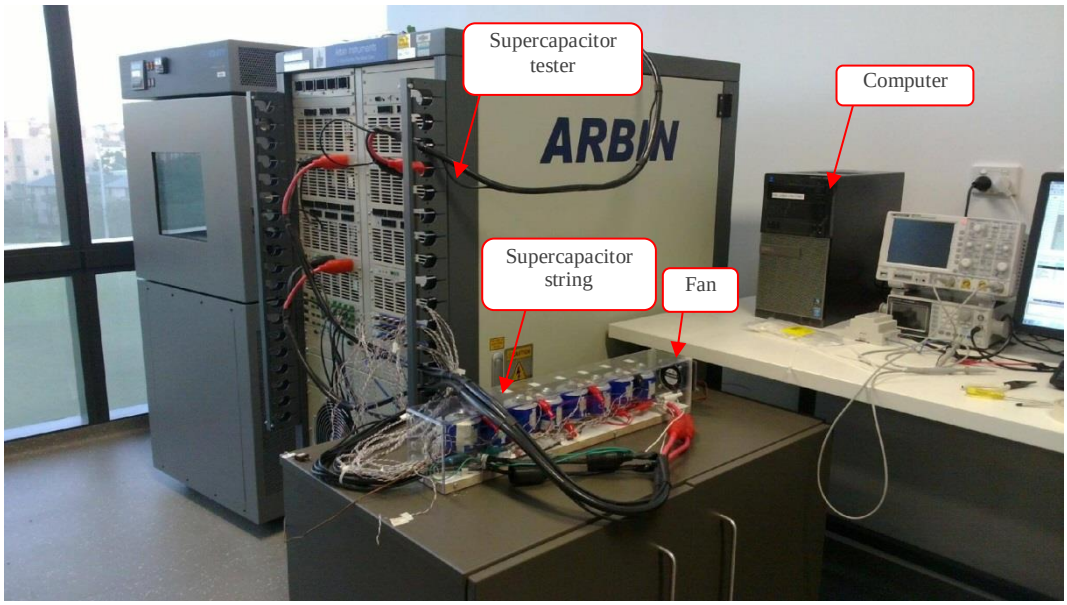

(a)

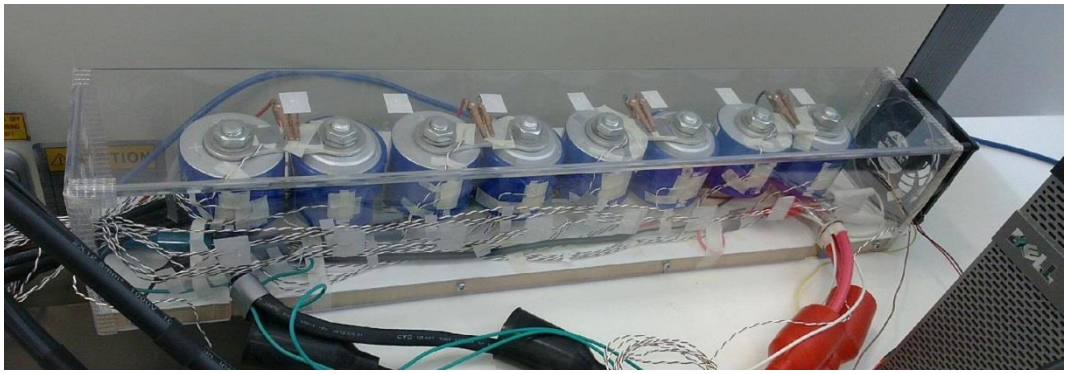

(b)

Figure 2.8. (a) Laboratory setup. (b) Supercapacitor string ($N = 8$).

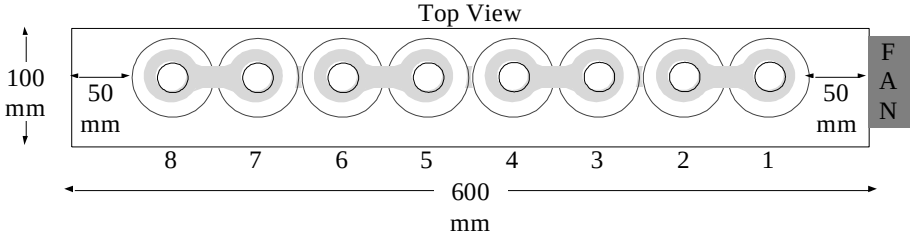

Figure 2.9. Experimental setup dimension.

Table 2.2. Maxwell BCAP0650 general specifications [78]

Parameters	Value
Rated capacitance	650 F
Maximum ESR_{DC} initial	0.8 mΩ
Rated voltage	2.7 V
Maximum continuous current ($\Delta T = 40$ °C)	88 A_{RMS}
Minimum operating temperature range (cell case temperature)	-40 °C
Maximum operating temperature range (cell case temperature)	65 °C

2.3.2. Determination of thermal model parameters

The information of each cell's temperature is given by the three temperature nodes of each cell in the string (T_c, T_s, and T_f). Despite the fact that the thermal parameters can be derived analytically from the material properties, it is more preferrable to identify the parameters empirically as for some specific geometries it is simpler and more accurate, as was done in [8, 9, 25, 70, 72]. Furthermore, some thermal parameters such as R_u and R_c for each individual cell are identified since the value of the temperature nodes are highly dependent on these parameters.

As our purpose is to simulate common commercially available string with a single speed cooling fan such as in [19, 20], the measurements for thermal parameters determination was done for an enclosed SC string cooled by a fan with a speed corresponding to approximately 34.1 cubic feet per minute (CFM). This value is selected based on a comparison with Maxwell's commercial 125-V SC module (consisting of six by eight 3000-F SC cells with the same cell diameter and twice the cell length as the Maxwell BCAP0650; cooled by two DC fans, 277 CFM each) [19, 79].

For parameterisation, a constant current charge-discharge cycle of 85 A was applied, cycling the SC string from the lower voltage limit (half the rated voltage) to the upper voltage limit (the rated voltage). The string was cycled until a thermal steady-state was achieved (see Figure 2.10).

2.3.2.1. Cell convection thermal resistance (R_u) and conduction thermal resistance (R_c)

R_u is related to the heat transfer via convection. As its value relates to the convection heat transfer coefficient that depends on the characteristics of the local air flow, it is highly dependent on the position of the cell in the module. Some literature on heat and mass transfer as well as heat exchanger such as [80, 81] provide correlations and expressions based on experimental results. However, instead of the mean or overall heat transfer, in this work, the point of interest is the local or individual heat transfer coefficient at particular spot, because we are interested in each cell's temperature nodes. Moreover, the common correlations and available expressions typically refer to typical tube banks configuration for heat exchanger, whose dimension and space are not similar to the tube dimension and space of our SC string. The local heat transfer coefficient could be found mathematically, as proposed recently by [23] for a forced-cooled staggered SC stack, provided that the local properties of the related parameters such as air velocity or air temperature are known, which could be difficult.

Sensitivity analysis performed by [25] and [82] also showed that R_u and the directly related parameters to R_u such as air speed and convection coefficient had the greatest sensitivity index value. This means that these parameters have the largest influence on the output of the thermal model, which is the temperature. Hence, individual R_u of each cell was derived based on experimental results. On the other hand, the variation of R_c for each cell should not be as large as R_u since it is more related to the cell materials. However, for better model accuracy, both R_u and R_c of individual cell are identified here.

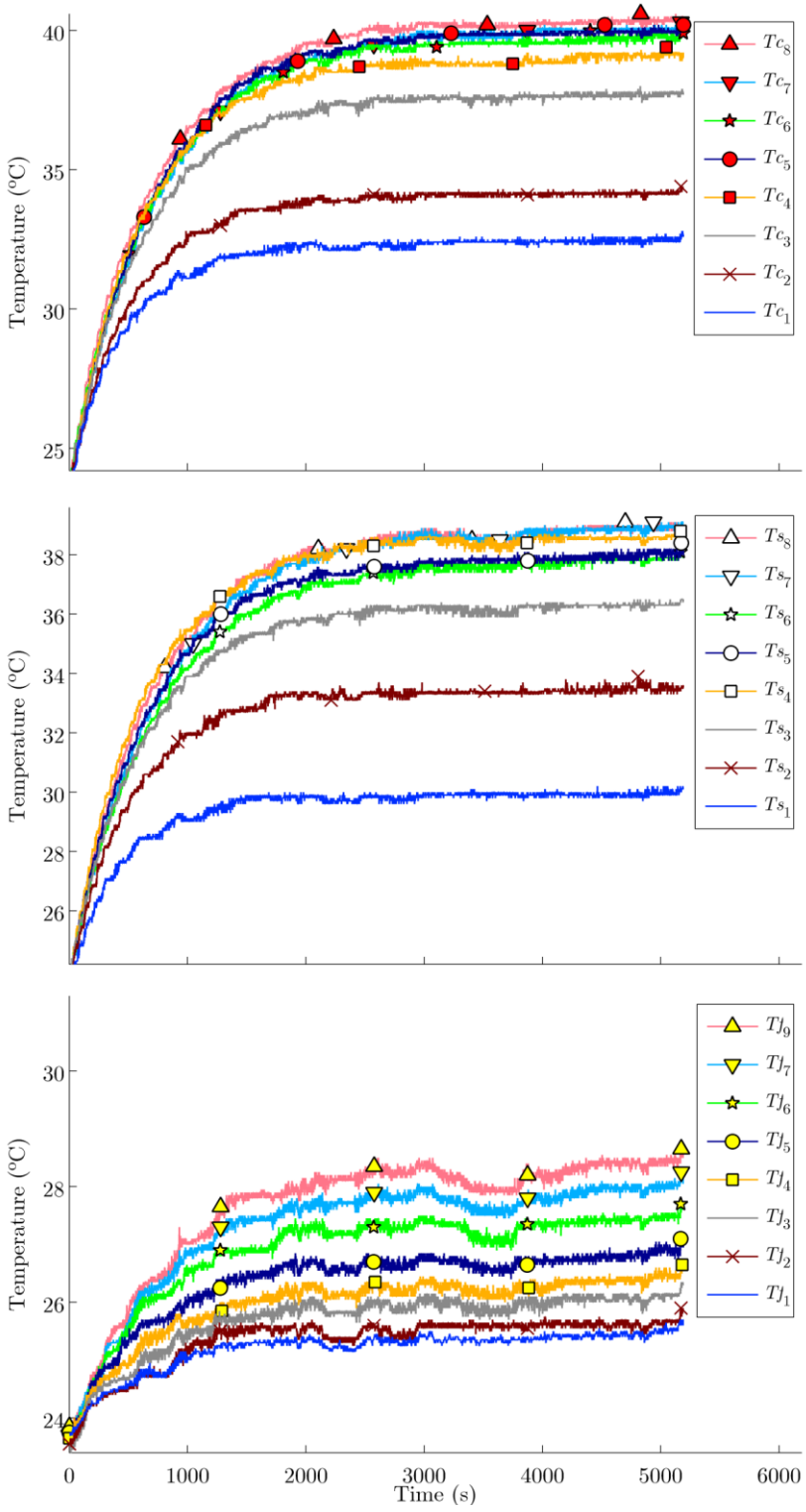

Figure 2.10. SC string temperature measurement for each cell: steady-state T_c (upper graph), T_s (middle graph), and T_f (lower graph).

Considering the steady state T_c, T_s, and T_f from the constant current cycling shown in Figure 2.10 and Figure 2.11, R_u and R_c can be calculated from (2.1) and (2.2). The R value of 0.8 mΩ is taken from the ESR value in the datasheet.

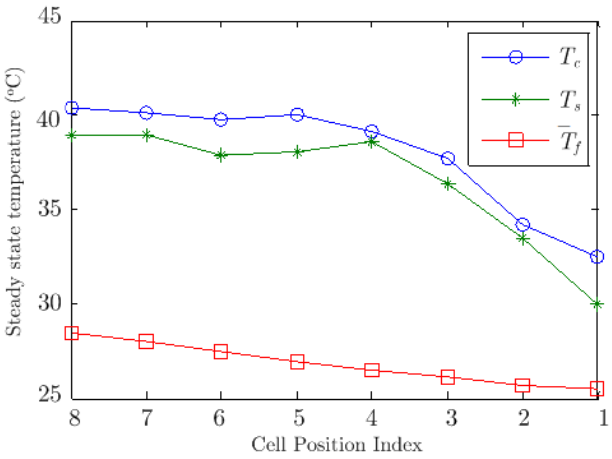

Figure 2.11. Steady-state temperature of each cell in the string.

The value of R_c and R_u for each cell in the string is plotted in Figure 2.12. It can be seen that R_u increases with distance of the cell to the cooling fan, and then it stays relatively constant. This is related to the steady-state surface temperature T_s, shown in Figure 2.11, showing increasing temperature which then turns relatively constant, similar to the presented data in [25], single-row cells data in [83], as well as CFD-simulated data in [24] and [84]. The reason for this similar "pattern" is that the heat transfer coefficient that defines R_u depends on the air flow characteristics such as velocity, turbulence, and flow pattern (e.g., if there exists wake or vortex behind the cells (tubes)). As the total number of the cells increases, the turbulent kinetic energy will gradually reach a steady state after a particular cell; which is the fourth cell in this case.

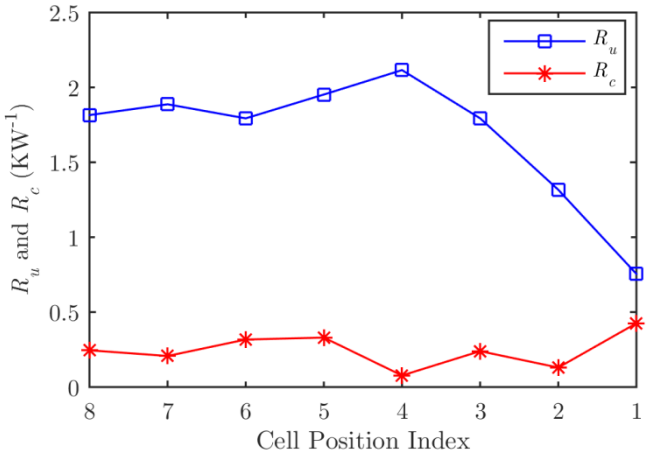

Figure 2.12. R_u and R_c value of each cell in the string.

2.3.2.2. Cell heat capacity (C_c and C_s)

C_c and C_s are related to the thermal properties of the cell material and are not as highly dependent on the air flow properties of the cell material as R_u is. They are also considered relatively constant over lifetime [71].

In this work, the value C_c and C_s are determined based on the transient part of the temperature graph (as in Figure 2.10), optimised by curve fit based on equations (2.1) and (2.2), as has also been done in [25, 85].

These values of C_c and C_s are then assigned to other cell as their values are expected to be similar for each cell. The assigned values for C_c and C_s are 258 and 17 JK^{-1}, respectively.

2.3.2.3. Cooling air capacity ($\rho c_p \dot{V}$ or $\dot{M} c_p$)

The cooling air capacity was discussed in Section 2.2 through equations (2.3) to (2.5). It is related to a certain volume of air flowing, "taking" and transferring the heat released by the cell. It is given by $\left(\rho c_p \dot{V}\right)$ or $\left(\dot{M} c_p\right)$, in which ρ is the air density, c_p is the air specific heat capacity, $\dot{V}$ is the air volumetric flow rate, and $\dot{M}$ is the air mass flow rate.

Both ρ and c_p are dependent on temperature, although within the interval of 0 to 70 °C, the ρ and c_p of air are relatively constant. At 1 atm pressure, ρ of air is 1.292 kg m^{-3} at 0 °C to 1.028 kg m^{-3} at 70 °C, while the c_p is 1006 $J(kg \cdot K)^{-1}$ at 0 °C and 1007 $(kg \cdot K)^{-1}$ at 70 °C [86]. Typically, the temperature at which the air properties are determined is approximated as the arithmetic mean of the surface of the solid boundary wall (T_s in this work) and the free stream temperature (T_f in this work). Hence, the cooling air capacity can be seen as a function of temperature and its varying value can be accommodated in a time-varying state-space thermal model. However, as the scope of this work is a time-invariant model, a constant value is calculated based on ρ and c_p at 35 °C, which is expected to represent the film temperature in the string during operation. With fan airflow rate of 34.1 CFM, the value of calculated $\rho c_p \dot{V}$ is 18.45 $J(K \cdot s)^{-1}$.

2.3.2.4. Cell-to-cell heat conduction (R_{cc})

Apart from the assumption that the heat released from the cell via convection is immediately removed by the air flow, another cell-to-cell heat transfer event via conduction is also considered. R_{cc} is the lumped thermal resistance related to the cell-to-cell heat conduction as well as other possible connections. In our setup, the SC cells are connected via aluminium connection tab. With the approximate tab dimension of 62.55-mm length and 1-mm by 12-mm cross section, and thermal conductivity of 237 $W(mK)^{-1}$ [86], the calculated R_{cc} is 21.99 KW^{-1}.

All parameters of the thermal model obtained as discussed previously are presented in Table 2.3.

Table 2.3. Thermal model parameters.

Parameters	Value
C_c	258 JK^{-1}
C_s	17 JK^{-1}
$\rho c_p \dot{V}$ or $\dot{M}\ c_p$	18.45 $J(Ks)^{-1}$
R_{cc}	21.99 KW^{-1}

2.4. Validation of string lumped thermal model

With the string current and air inlet temperature as the inputs as in (2.8), the output of the thermal model with the determined parameters as discussed previously is evaluated and compared with the experimental data. While constant current cycling in Section 2.3.2 was used for identification, a customised load pattern consisting of different charge-discharge as well as short and long rest periods, depicted in Figure 2.13, was used for validation. The particular load pattern is customised as such to yield fluctuating temperature.

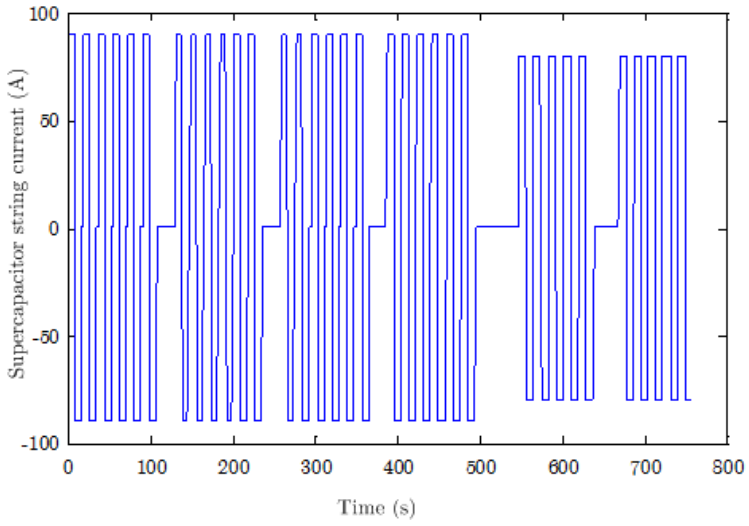

Figure 2.13. Load pattern consisting of charge-discharge and short and long rest periods for generating fluctuating temperature for thermal model validation.

The validation results for the customised load pattern is shown in Figure 2.14, in which the temperatures measured from the SC string are overlaid together with the temperatures simulated based on the thermal model.

The dynamics of both the simulated and measured temperatures are in good agreement. The root-mean-squared error (RMSE; see (2.12)) of identification phase and validation phase are calculated for the time interval of $t = 1$ to 2000 s, assuming that it is the time interval before the steady-state period. The RMSE is presented in Table 2.4, with the overall values less than 1 °C.

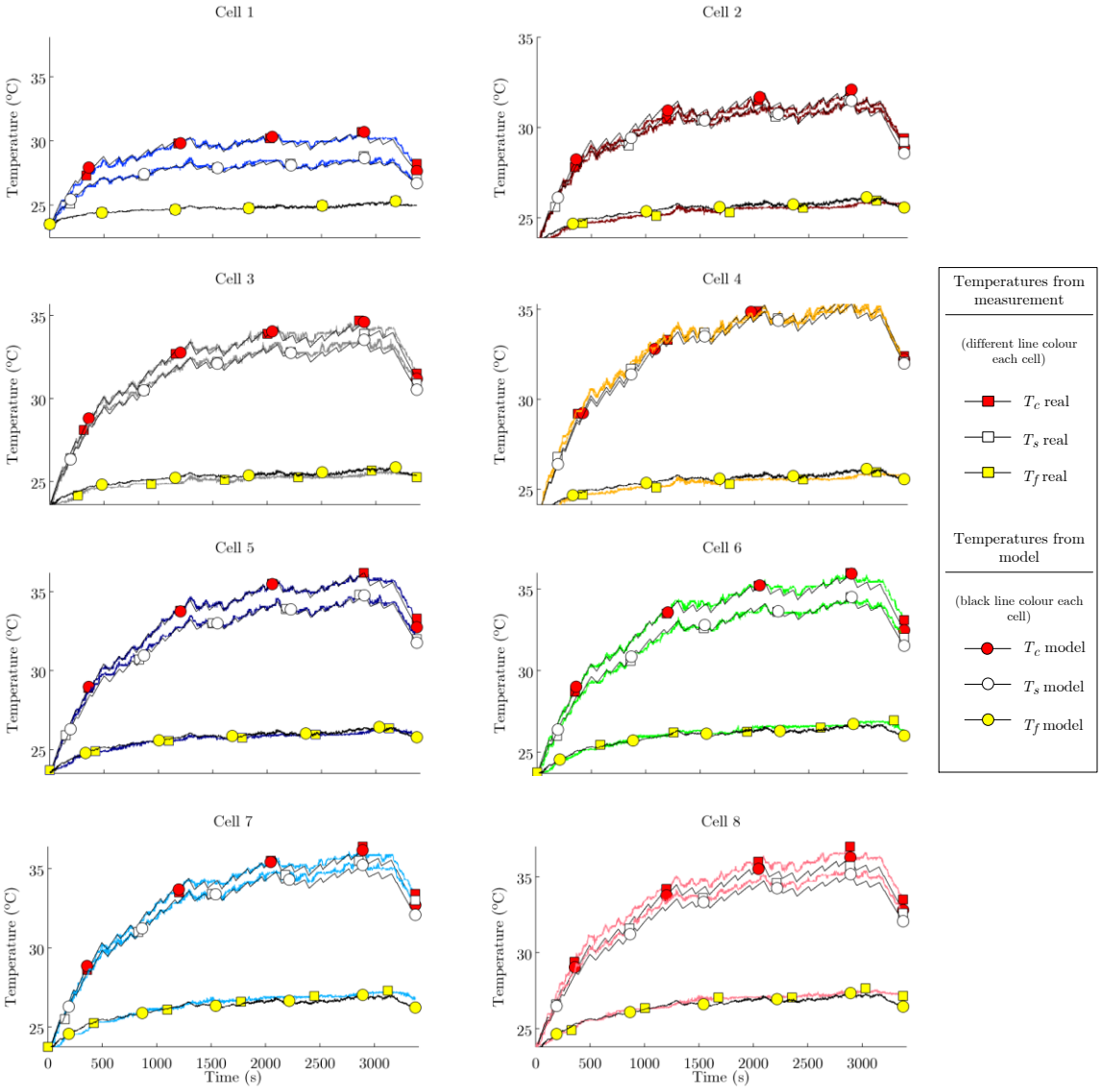

Figure 2.14. T_c, T_s, and T_f from measurement and from model for validation phase.

$$\text{RMSE}=\sqrt{\frac{1}{n}\sum_{i=1}^{n}\left(x_i-\widehat{x}_i\right)^2} \tag{2.12}$$

Table 2.4. RMSE of identification phase and validation phase (before steady-state period)

	RMSE T_c (°C)		**RMSE T_s(°C)**		**RMSE T_f (°C)**	
	Id.	**Val.**	**Id.**	**Val.**	**Id.**	**Val.**
Cell 1	0.18	0.22	0.14	0.16	0	0
Cell 2	0.21	0.21	0.17	0.16	0.18	0.19
Cell 3	0.21	0.18	0.24	0.22	0.17	0.16
Cell 4	0.57	0.33	0.64	0.48	0.15	0.11
Cell 5	0.41	0.22	0.53	0.35	0.09	0.14
Cell 6	0.43	0.30	0.25	0.19	0.22	0.31
Cell 7	0.29	0.26	0.26	0.30	0.31	0.41
Cell 8	0.77	0.75	0.72	0.65	0.35	0.48

Id. : Identification Phase

Val. : Validation Phase

2.5. Summary

In this chapter, the details of cylindrical battery and SC cell considered in the thesis are given and the commonality is discussed. The lumped thermal model for the string consisting of serially connected cells is developed and the model parameters are determined using an SC string setup.

It is shown that the convection resistance R_u can be considered a critical parameter as it is highly dependent on the air flow and the position of the cell in the string.

The validated thermal model yields temperature which is in good agreement with the measured temperature. The model is applicable for other type of forced-cooled electrochemical storage string with cylindrical cells, provided that the thermal parameters value is determined accordingly.

For the remainder of this thesis, the thermal model with parameters value from the validation in this chapter is used for work related to SC string, unless stated otherwise. As for the work related to battery string, the parameters value is obtained from the relevant references, and details will be provided in the related chapters.

Chapter 3. Observability-Analysis-Based Optimal Sensor Placement for String Temperature Estimation

3.1. Introduction

In Chapter 2 [62] a thermal model for an electrochemical storage string was discussed. The thermal model is useful for temperature estimation in order to monitor temperature distribution of a device with a limited number of sensors. The model-based temperature estimation, also commonly named "virtual sensor" or "soft sensor" method, is applied for different applications from ICs [1], power electronics converters [3], electric machines and transformers [5, 6], as well as batteries [8]. The estimation procedure could be open-loop (estimates the states solely based on the model and inputs) or closed-loop (a number of measured outputs is used as feedback to improve the estimation). For a closed-loop estimation, the sensor placement measuring these outputs can influence the estimation performance.

As summarised in Section 1.2.2, few references had examined sensor placement for temperature estimation in storages [8, 18, 36, 37], in which system observability is a common basis for sensor placement. "Observability" itself could be defined according to different criteria; for instance, one related to the system eigenmode [36, 37], or the more common criterion such as the rank of observability matrix [18] as well as the property of observability Gramian, which is investigated in this thesis.

References [18, 71] analysed temperature sensor placement in a string of cylindrical battery cells by evaluating the rank of observability matrix. However, only the number of observable sensor combinations was considered, whereas the information whether particular combinations might be better than the others (or vice versa) was neither analysed nor quantified. It was noted though, that for a

string with more than a particular number of cells, sensor location would also affect observability. Whilst it was not discussed in the aforementioned references, this information could be obtained by quantifying the system observability, in which a system's observability is seen not only as a binary measure (as in the conventional definition based on the rank of observability matrix), but also having different measurable degree, which is feasible by utilising the properties of observability Gramian.

On the other hand, there are several different observability measures or criteria derived from the observability Gramian, such as the one related to the maximum or minimum singular value, the sum of singular values, or the determinant. With some references [26, 27, 29] deducing that the suitability of any specific criteria for a particular system cannot be generalised, one contribution of this thesis is to assess of the suitability of different observability-Gramian-based criteria for string temperature estimation with a limited number of sensors. The performance of the estimation with particular sensor placement or combinations is also evaluated in this chapter.

The remainder of this chapter is organised as follows. A brief summary of the system observability as well as a general instance of string temperature estimation is presented in Section 3.2. The observability Gramian and the observability criteria derived from it are explained in Section 3.3, followed by case studies in Section 3.4 and a summary in Section 3.5.

3.2. System observability and state estimation for string temperature monitoring

3.2.1. System observability

For systems represented in state-space model, observability deals with whether or not the initial state can be observed from the output, or generally, whether the states can be estimated (observed) from knowledge of the input and the output.

There are several equivalent criteria to determine system observability, such as the ones discussed in [87, 88]. One simple and well-known criterion is the observability matrix. For an nth order system with the state-space model as in (2.6), the observability matrix is

$$\mathbf{O}_m = \begin{bmatrix} \mathbf{C} \\ \mathbf{C}\mathbf{A}_c \\ \vdots \\ \mathbf{C}\mathbf{A}_c^{n-1} \end{bmatrix} \tag{3.1}$$

and the system states are observable if the matrix $\mathbf{O}_m$ is of rank n.

Referring to the state-space thermal model in Section 2.2, the string observability for state estimation could be associated with the selection of the measured state. An example using the built 8-cell SC string is given as follows.

It is considered that the surface temperature nodes (T_s) of all eight cells are measured. Therefore, there are feedbacks from eight states out of the total sixteen states (i.e. a total of 24 temperature nodes consisting of sixteen T_c and T_s nodes plus eight T_f nodes not included as states in the state space). Thus, the corresponding $\mathbf{C}$ matrix is an eight-by-sixteen matrix as follows:

$$\mathbf{C} = \begin{bmatrix} 0 & 1 & 0 & 0 & 0 & 0 & 0 & 0 & 0 & 0 & \cdots & 0 \\ 0 & 0 & 0 & 1 & 0 & 0 & 0 & 0 & 0 & 0 & \cdots & 0 \\ \vdots & \vdots & \vdots & \vdots & \vdots & \vdots & \vdots & \vdots & \vdots & \vdots & \ddots & \vdots \\ 0 & 0 & 0 & 0 & 0 & 0 & 0 & 0 & 0 & 0 & \cdots & 1 \end{bmatrix} \tag{3.2}$$

With this configuration, the system is observable. An observer or estimator could be designed to estimate the states based on the measurement. While there are various approaches and considerations in designing the estimator, it is beyond the scope of this thesis. Thus, a basic closed-loop observer and/or a steady-state Kalman filter are used to support the discussion in the thesis.

3.2.2. String temperature estimation

In this subsection, a basic closed loop observer is designed to demonstrate the applicability of the string temperature estimation based on the validated thermal model. It should be noted that a more specific case such as parameter changes due to aging would require a more advanced estimator such as adaptive observer which is beyond the scope of this work, and thus will not be discussed.

The observer has the following form:

$$\begin{aligned} \dot{\hat{\mathbf{x}}} &= \mathbf{A}_c\hat{\mathbf{x}} + \mathbf{B}_c\mathbf{u} + \mathbf{L}\left(\mathbf{y} - \hat{\mathbf{y}}\right) \\ \hat{\mathbf{y}} &= \mathbf{C}\hat{\mathbf{x}} \end{aligned} \tag{3.3}$$

in which $\hat{\mathbf{x}}$ and $\hat{\mathbf{y}}$ are the estimated states and outputs, respectively, and $\mathbf{L}$ is the observer gain. The thermal parameters in the matrices are based on the validated model in Section 2.3 and Section 2.4, while the measurement matrix $\mathbf{C}$ is given in (3.2).

The information of the cells' surface temperature is used as an initial estimate of the states.

As seen in (3.3), the observer gain $\mathbf{L}$ drives the dynamics of the difference (error) between the actual and estimated states. In the pole placement method, the gain $\mathbf{L}$ is determined using the poles (eigenvalues) of the closed loop observer which are selected to yield stability and a desired transient response of this error [89].

In a continuous system, the observer poles are placed further to the left side of the complex plane (or in a discrete system, closer to the origin in the complex plane) as this results in faster observer dynamics. However, there is a trade-off as faster dynamics usually yield higher overshoot. For the discretised system in this work, the poles of the closed loop observer are located closer to the z-plane origin by an absolute value of 0.05 from the original system poles, to yield fast observer dynamics.

The algorithm for the estimation by the observer is implemented in MATLAB and is tested using the experimental data collected from the setup, in the same

way as in [70], [90], and [91]. We use the aforementioned customised pattern in Figure 2.13 for testing the observer performance as the pattern represents the typical SC load pattern for electric vehicle applications, such as in [9], [83], and [92], which incorporates various charges and discharges as well as different rest intervals. The selected pattern can also yield temperature fluctuation, from which the observer performance of capturing temperature dynamics can be evaluated better.

The SC string was initially operated with one cycle of the customised load pattern and subsequently turned off for ten minutes with the fan also turned off, referred to as 'Stage 1' and 'Stage 2', respectively (Figure 3.1). The string was then turned on again with two cycles of the customised load pattern ('Stage 3').

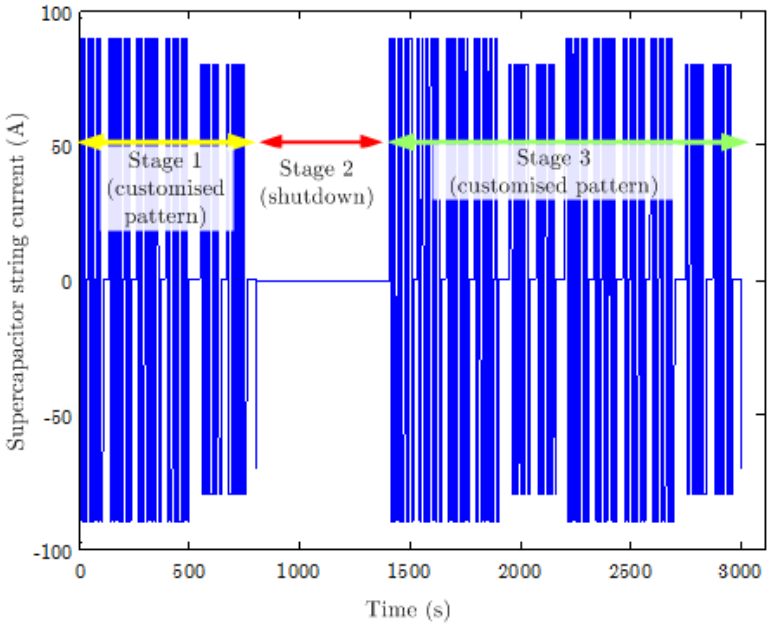

Figure 3.1. Load pattern including 10-minute rest for testing temperature estimation with observer.

This choice of pattern of stages is designed to simulate short shutdown of an electric vehicle (e.g. car) which occurs occasionally. During the shutdown, the cells in the string will cool down under natural convection as the fan is

off. However, for a short shutdown, it is most unlikely that all the cells can cool down completely to the ambient temperature. Hence, when the string is being operated again (e.g. the vehicle is being operated again), as simulated by 'Stage 3', the cells initial states are most likely to be different. Therefore, by using the selected pattern shown in Figure 3.1, the estimation convergence time of the observer under unknown initial condition can be evaluated as well.

The real states as well as the estimates are presented in Figure 3.2. It can be observed that the real and estimated temperatures are in good agreement. The temperature fluctuation can also be captured relatively well by the observer. A few small overpredictions noticeable at the beginning of 'Stage 3' can be explained as follows.

As the whole string is being operated again, the fan also turns on and the cells are quickly cooled down by forced convection, creating drastic temperature decrease. Nevertheless, the estimated temperature quickly converged to the real temperature.

For evaluation purpose, in 'Stage 3' we define t_{conv} as the first time the absolute difference between the true and the estimated states converges and stays within the error bound, which is chosen to be 2.5 % in this case.

Table 3.1 lists this convergence time as well as the root-mean-squared error (RMSE). With the selected observer gain, the estimation error of all states converges to the 2.5 % bound in less than two minutes, while the RMSE is less than 0.4 °C. Overall, during Stage 3 in which the cells initial temperatures were different, the observer delivers satisfactory performance in estimating the cells string temperature.

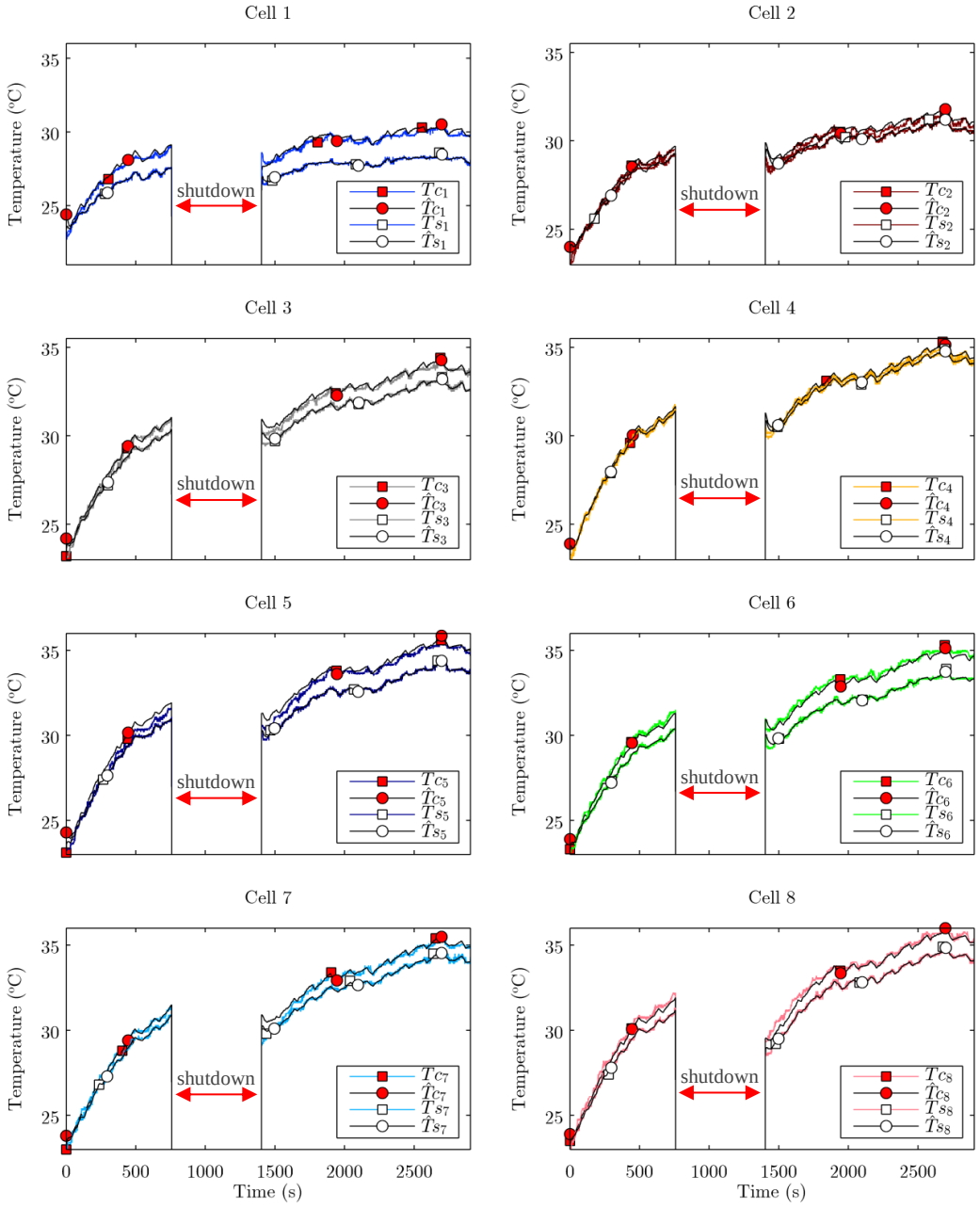

Figure 3.2. Real and estimated states of T_c and T_s of the cells in the string.

Table 3.1. RMSE and convergence time of estimation error for Stage 3 (8-cell SC string with 8 sensors)

	RMSE T_c (°C)	**RMSE T_s(°C)**	**t_{conv} T_c (s)**	**t_{conv} T_s (s)**
Cell 1	0.24	0.11	9	3
Cell 2	0.24	0.18	34	39
Cell 3	0.20	0.12	–*	–*
Cell 4	0.16	0.14	14	11
Cell 5	0.26	0.09	16	–*
Cell 6	0.21	0.11	–*	–*
Cell 7	0.30	0.12	74	14
Cell 8	0.23	0.10	–*	–*

*Estimation error for this state is already within the 2.5% bound since measurement of 'Stage 3' begins.

Using the rank of observability, it is found that the minimum number of sensors ensuring full observability for the SC string is three, and there is more than one combination of three sensors yielding full observability. For example, sensor placement at T_s node of cells 1, 3, 6 (henceforth it will be referred to as (1,3,6) and so on accordingly) will give the same observable system as placement (3,6,8). To analyse whether a combination might have better observability degree than the other, a quantification of the observability is required.

This topic of observability quantification has been discussed in many references, including [26-28, 30, 93, 94] to name a few related to the sensor placement. Observability degree criteria based on observability Gramian matrix are used most often.

3.3. Observability Gramian and observability degree criteria

3.3.1. Observability Gramian

Observability Gramian is an alternative to the conventional observability matrix for analysing system observability. Observability Gramian matrix $\mathbf{W}_O$, of the state-space system (2.6) can be expressed as (3.4).

$$\mathbf{W}_O = \int_0^\infty e^{\mathbf{A}_c{}^T t}\mathbf{C}^T\mathbf{C}e^{\mathbf{A}_c t}dt \tag{3.4}$$

The observability Gramian is positive definite if and only if the n-dimensional pair ($\mathbf{A}_c$, $\mathbf{C}$) is observable, provided that all eigenvalues of $\mathbf{A}_c$ have negative real parts [87]. The statement is thus equivalent with the expression stating that the observability matrix has a full rank.

The observability Gramian solves the Lyapunov equation:

$$\mathbf{A}_c{}^T\mathbf{W}_O + \mathbf{W}_O\mathbf{A}_c + \mathbf{C}^T\mathbf{C} = 0 \tag{3.5}$$

Gramian-based observability criteria are mostly derived from the physical interpretation of the observability Gramian, which is often referred to as the "observation energy". Assuming that the input $u(t) = 0$ and the initial state $\mathbf{x}(0)=\mathbf{x}_0$, the system (2.6) produces the output

$$\mathbf{y}(t) = \mathbf{C}e^{\mathbf{A}_c t}\mathbf{x}_0, \qquad t \geq 0 \tag{3.6}$$

The "energy" E of this output is, based on its Euclidean norm, equal to

$$\begin{aligned} E &= \int_0^\infty \mathbf{y}^T(t)\mathbf{y}(t)dt \\ &= \int_0^\infty \mathbf{x}_0^T(t)e^{\mathbf{A}_c{}^T t}\mathbf{C}^T\mathbf{C}e^{\mathbf{A}_c t}\mathbf{x}_0 dt \\ &= \mathbf{x}_0^T\mathbf{W}_O\mathbf{x}_0 \end{aligned} \tag{3.7}$$

From equation (3.7) it can be deduced that a small value of observation energy indicates small effect of the initial state on the output (with zero input to the system), and vice versa. Another point can also be inferred from equation (3.7). If $\mathbf{W}_O$ is factorised into singular value decomposition as follows:

$$\mathbf{W}_O = \mathbf{U}\Sigma\mathbf{U}^T, \qquad \Sigma = \mathrm{diag}\left(\sigma_1, \sigma_2, ..., \sigma_{n_x}\right) \tag{3.8}$$

where $\mathbf{U}$ is a unitary matrix and $\mathbf{\Sigma}$ is a rectangular diagonal matrix with the diagonal entries σ_i being the singular values of the observability Gramian, then, the energy can be considered to be proportional to the singular values of the observability Gramian. A system with larger observation energy, which comes from larger singular values, implies that it is more observable or more easily observed. "More observable" can be understood as giving more signal response to the sensor from the perturbations in the initial states [26, 27].

3.3.2. Observability degree criteria based on observability Gramian

Different observability scalar quantifications for both linear and non-linear systems have been proposed in many references and a short overview can be found in [28] and [95]. Table 3.2 summarises some of the different observability criteria which are used in references, either individually or combined. The first column shows the criterion based on which the observability is quantified and the second column shows the mathematical expression of the criterion. The third column shows whether the "best" configurations would be the maximum or the minimum of the criterion in the first column, if one is to rank different system configurations based on their observability degree.

Table 3.2. Some observability criteria based on observability Gramian

Criterion	**Equation**		**"Best" configuration**
Spectral radius (SR) [27, 28]	$\mathrm{SR}\left(\mathbf{W}_O\right) = \sigma_{\max}\left(\mathbf{W}_O\right)$	(3.9)	$\{\max\}\mathrm{SR}\left(\mathbf{W}_O\right)$
Trace [26-28, 36]	$\mathrm{trace}\left(\mathbf{W}_O\right) = \sum_{i=1}^{n} \sigma_i\left(\mathbf{W}_O\right)$	(3.10)	$\{\max\}\,\mathrm{trace}\left(\mathbf{W}_O\right)$
Near singularity (NS) [26-28]	$\mathrm{NS}\left(\mathbf{W}_O\right) = \sigma_{\min}\left(\mathbf{W}_O\right)$	(3.11)	$\{\max\}\mathrm{NS}\left(\mathbf{W}_O\right)$
Condition number (CN) [26, 28]	$\mathrm{CN}\left(\mathbf{W}_O\right) = \dfrac{\sigma_{\max}\left(\mathbf{W}_O\right)}{\sigma_{\min}\left(\mathbf{W}_O\right)}$	(3.12)	$\{\min\}\,\mathrm{CN}\left(\mathbf{W}_O\right)$
Determinant (Det) [29, 95]	$\det\left(\mathbf{W}_O\right)$	(3.13)	$\{\max\}\det\left(\mathbf{W}_O\right)$

Different observability criteria may result in different "best" configurations, and a certain criterion may be more suitable for a particular application. SR and trace criteria are strongly influenced by the largest singular value (i.e. the largest "energy"), which can be interpreted as a large response from certain state(s) which can then be observed in the sensor readings. On the other hand, NS criterion is based on the smallest singular value (i.e. the smallest "energy"), which indicates how close a system is to being unobservable (i.e. a singular matrix; hence the name "near singularity"), while CN is affected by both the smallest and the largest singular value. As for criterion based on determinant, some references such as [29, 95, 96] identifies that the determinant criterion is better in capturing information redundancy when dealing with placement of multiple sensors, compared to other criteria. We shall see in the following sections how these criteria suit the application of electrochemical storage string temperature estimation.

3.4. Case study: Eight-cell SC string and twelve-cell battery string

A 12-cell battery string with reference to [18, 71] is also considered in addition to the 8-cell SC string. With more number of cells (and hence more sensor combinations probability), it is expected that the case study could better demonstrate better the sensor placement based on observability Gramian. As only the SC string setup was built in the laboratory, the work related to the battery cell will be based on simulations.

Two cases will be discussed: Observability degree for different total number of sensors in Subsection 3.4.1, and observability degree for a given number of sensors in 3.4.2.

The specification of the battery string is as follows. The cell is the A123 32157 $LiFePO_4$/graphite battery (shown in Figure 2.3.(a)). The cell parameters (in regards to the thermal model in Chapter 2) were taken from [18], while those not explicitly listed were assumed implicitly from the cell's physical dimensions and materials. The parameters values are shown in Table 3.3. As in [18], forced

convection was considered and the value of R_u corresponds to an air flow rate of $9.5 \cdot 10^{-3}$ m^3 s^{-1}, with fixed air flow temperature of 25 °C.

Table 3.3. Battery cell parameters values

Parameters from [18]		**Implicit parameters**	
Parameter	**Value**	**Parameter**	**Value**
C_c	268 JK^{-1}	R_{cc}	1.125 JK^{-1}
C_s	18.8 JK^{-1}	$\dot{M}\ c_p$	11.327 $J(K{\cdot}s)^{-1}$
R_c	1.266 KW^{-1}		
R_u	0.79 KW^{-1}		
R	3.5 mΩ		

3.4.1. Observability degree for different total number of sensors

The purpose of this subsection is to analyse and compare two sensor combinations which are both observable based on the rank of observability matrix. For the 8-cell SC string, the minimum number of sensors yielding full observability is three, while for the 12-cell battery string it is four. The observability degree and the estimation performance between each observable combinations will be compared.

The observability degree comparison of 8-sensor and 3-sensor case for 8-cell SC string is shown in Table 3.4, while the comparison of 12-sensor and 4-sensor case for 12-cell battery string is shown in Table 3.5. It can be observed that while all the cases are observable, they have different degree of observability.

The estimation performances of each case are evaluated using different load patterns as listed in Table 3.6. For brevity, both the temperature RMSE and t_{conv} are averaged according to the number of the states, and the comparison of these two measures for the 8-sensor and the 3-sensor estimation are depicted in Figure 3.3. For both load patterns, the metrics indicate better estimation performance for the 8-sensor case, confirming a higher degree of observability. The comparison graph of battery string is depicted in Figure 3.4, which shows the same trend as

Figure 3.3, thus confirming the different observability degree as well as its influence on the estimation performance.

Table 3.4. Observability degree comparison of 8-cell SC string: 8 sensors vs 3 sensors (3,5,8).

Criterion	8 sensors	3 sensors
SR	237.54	184.60
Trace	1275.21	527.20
NS	0.61	$7.58 \cdot 10^{-8}$
CN	387.40	$2.44 \cdot 10^{9}$
Determinant	$6.33 \cdot 10^{18}$	$6.88 \cdot 10^{-28}$

Table 3.5. Observability degree comparison of 12-cell battery string: 12 sensors vs 4 sensors (2,5,9,10).

Criterion	12 sensors	4 sensors
SR	89.83	36.75
Trace	275.26	86.97
NS	1.64	$4.53 \cdot 10^{-6}$
CN	54.76	$8.11 \cdot 10^{6}$
Determinant	$1.36 \cdot 10^{18}$	$1.71 \cdot 10^{-36}$

Table 3.6. List of the load patterns used for evaluation

	Name	Remarks
SC string	Load Pattern 1	Customised pattern including 10-minute rest (Figure 3.1)
	Load Pattern 2	Constant-current charge-discharge of 85 A.
Battery string	Load Pattern 3a	Customised pattern of charge-discharge and rests (Figure 2.13), normalised to battery current capacity.
	Load Pattern 3b	Same as Load Pattern 3a but with unmatching model parameters of 10 %.
	Load Pattern 4	Constant-current charge-discharge of 50 A, unmatching model parameters of 10 %.

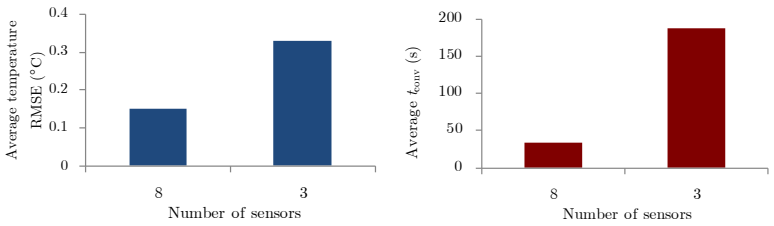

Figure 3.3. Eight-cell SC string estimation performance comparison of 8 sensors and 3 sensors: average RMSE (left figure) and t_{conv} (right figure).

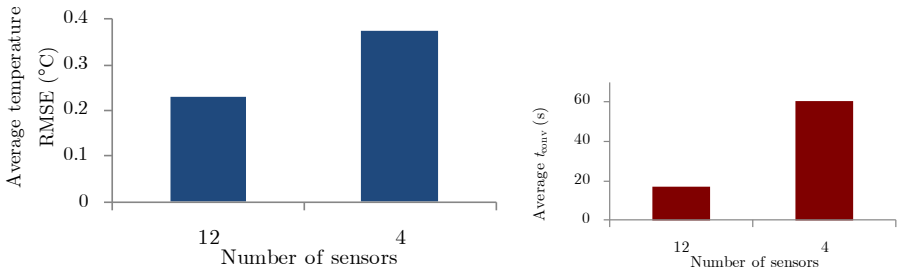

Figure 3.4. Twelve-cell battery string estimation performance comparison of 12 sensors and 4 sensors: average RMSE (left figure) and t_{conv} (right figure).

One notable observation is that there were cases for the system with fewer sensors in which the specified poles could not be assigned; while for the system with more sensors the same particular poles could. Related to this, a number of references [97-99] demonstrated the relationship between the system's distance to uncontrollability (and in related manners, unobservability) to the robustness and sensitivity of the pole-placement problem. The pole placement for a system with small distance to uncontrollability / unobservability was expected to be sensitive to perturbations and face numerical computation difficulties. Hence, this can be a possible reason why, in this work, for a lower observable system, a particular set of poles could not be assigned, although theoretically the system's observability ensures the ability to assign arbitrary sets of poles.

3.4.2. Observability degree for a given number of sensors

We already see how the same observable systems actually have different observability degree yielding in different estimation performance. In this subsection, the similar evaluation will be conducted for different combinations of the same given number of sensors. First, the two of highest rank combinations from each criterion described in Subsection 3.3.2 are selected. The combinations for the SC string and the battery string are illustrated in Figure 3.5 and Figure 3.6, respectively. These combinations will be evaluated with the same manner as in Subsection 3.4.1. One additional criterion, namely "Naïve", is also included. This criterion placed the sensors not based on any observability-based criteria, but intuitively place the sensors in a distributed manner along the string.

It can be observed in Figure 3.5 that there are few combinations which are in the "top two" based on more than one criterion. For example, (3,6,8) which is in the "top two" combinations based on determinant and NS criteria; and (3,5,8) which is in the top two combinations based on NS and CN criteria. As for the battery string, as seen in Figure 3.6, the high-ranked combinations proposed by NS, CN, and determinant criteria are similar as well.

Why these different criteria suggest similar combinations can be explained as follows. Referring to (3.11) and (3.12), NS is directly related to the smallest singular value ($\sigma_{\min}$), while CN are related to both the largest ($\sigma_{\max}$) and the smallest singular value. The data of $\sigma_{\max}$ from each observable combination do not show large interval between different combinations (variation is less than one order of magnitude). On the other hand, there is a big range or interval (several orders of magnitude) seen in the data of $\sigma_{\min}$ from each observable combination. That means, the combinations suggested by CN criterion will depend much more on $\sigma_{\min}$ than on $\sigma_{\max}$. Hence, the suggested combinations will most likely be very similar to the ones based on NS criterion. Nevertheless, this case could be different for other applications with different singular values characteristics.

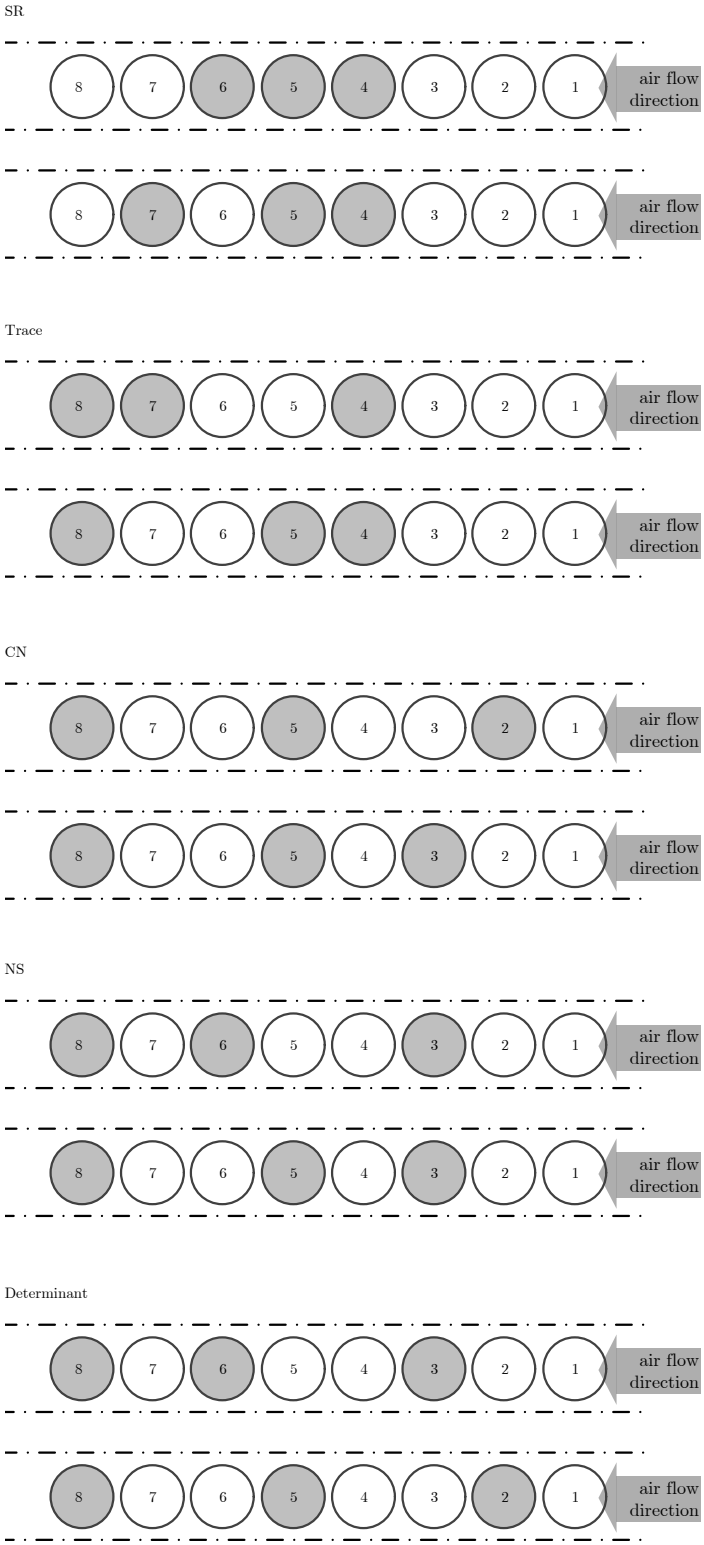

Figure 3.5. Top two sensor combinations proposed by each observability criteria for 8-cell, 3-sensor SC string (cells with sensor are marked).

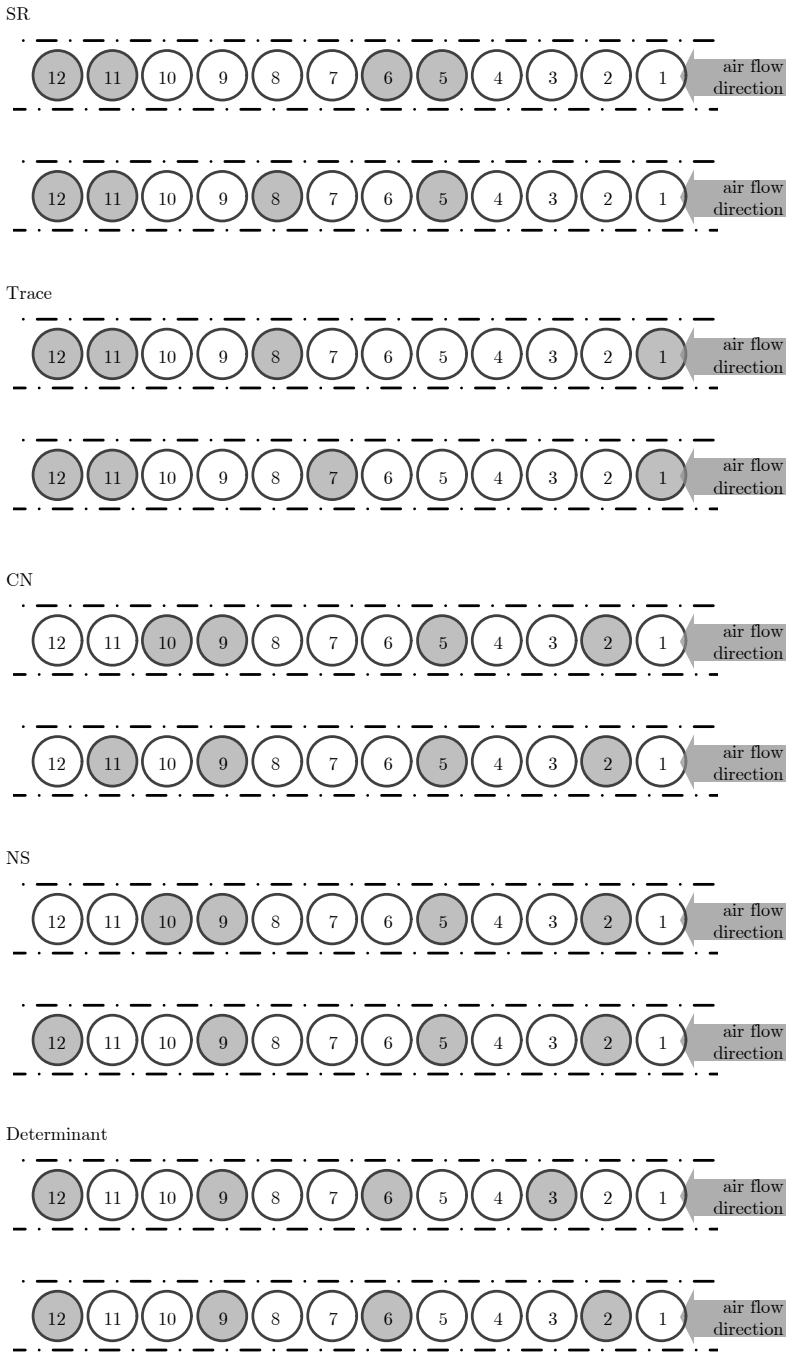

Figure 3.6. Top two sensor combinations proposed by each observability criteria for 12-cell, 4-sensor battery string (cells with sensor are marked).

The determinant criterion (as in (3.13)) is related to one of the properties of a determinant of a matrix [100]: the determinant of a matrix is the product of its eigenvalues. As observability Gramian is a symmetric matrix, its singular values are the same as the absolute value of its eigenvalues. Hence, similar to the CN criterion, the large range of $\sigma_{\min}$ of different combinations will influence the determinant criterion considerably.

On the other hand, the SR (as in (3.9)) and trace (as in (3.10)) criteria are closely related, because the sum of the singular values (which become the basis for trace criterion) are influenced more significantly by the largest singular values than by the smallest ones.

It can be observed from Figure 3.5 and Figure 3.6 that the combinations suggested by SR and trace often include closely placed sensors. In some references [26, 29], this is associated with information redundancy and the nature of the placement based on $\sigma_{\max}$ itself. Nevertheless, the result of the estimation will be analysed to evaluate this matter.

The comparison of average RMSE for different sensor combination in the 8-cell 3-sensor SC string is shown in Figure 3.7, while the comparison of average t_{conv} is shown in Figure 3.8. There are some data not shown in the graph because the estimation of the associated combinations did not perform well (e.g. large overshoots and fluctuations), yielding large value of the metrics RMSE and t_{conv}. The data not shown are combination based on SR and "Naïve" combinations.

Meanwhile, for the 12-cell 4-sensor battery string, the comparisons of the average RMSE and t_{conv} are shown in Figure 3.9 and Figure 3.10, respectively.

Overall, based on the metrics, the naïve-criterion-based combinations delivers the least satisfactory performance, followed by the SR-criterion-based combinations which also yielded high average RMSE and t_{conv}. The combinations with the lowest average RMSE and t_{conv} are those based on CN, NS, and determinant criteria, with values which are slightly lower than those yielded by trace-based combinations.

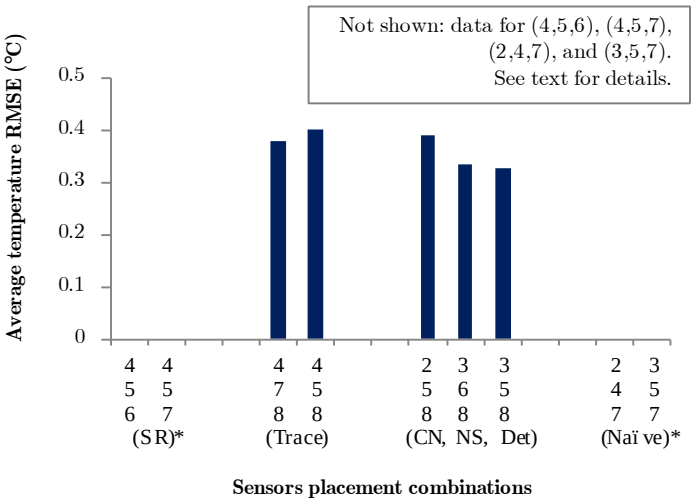

Figure 3.7. Comparison of average RMSE for different sensor combinations in the 8-cell 3-sensor SC string.

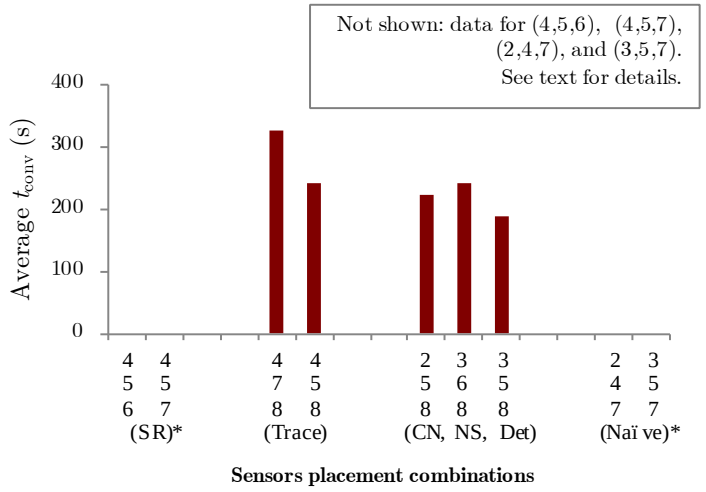

Figure 3.8. Comparison of average t_{conv} for different sensor combinations in the 8-cell 3-sensor SC string.

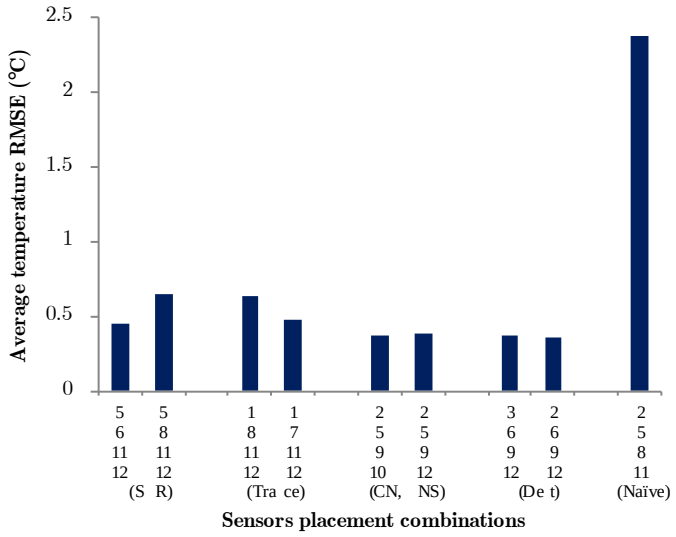

Figure 3.9. Comparison of average RMSE for different sensor combinations in the 12-cell 4-sensor battery string.

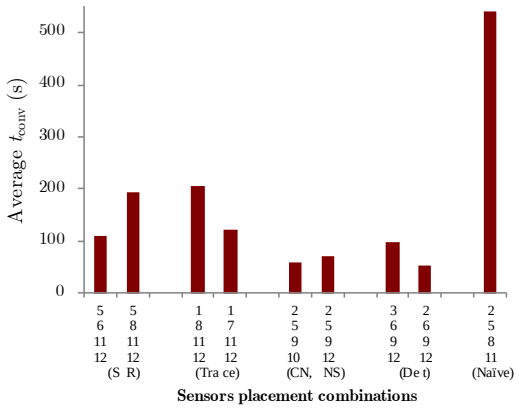

Figure 3.10. Comparison of average t_{conv} for different sensor combinations in the 12-cell 4-sensor battery string.

These results support the notion that observability criteria which depends only on largest singular values (which are related to strong observable states or directions) appear to be unsuitable if the purpose is to monitor the temperature of the whole string. For this purpose, every state has the same importance and

each needs to be observed. Thus, the observability criteria which are more suitable for this purpose are the ones which also consider small singular values, which means they consider all state contribution. Of course, different priority could also yield different purpose, such as in [36] where it proposed the idea of maximising observability of particularly selected states which were considered more important than the other states.

The results also explain sensor placement redundancy which is often included in combinations based on SR and trace criteria. With the fact that the observability Gramian matrix for multiple sensors could be built by adding the observability Gramian matrices for single sensor [29], the SR and trace will most likely suggest similar sensor placement for increasing given number of sensors.

For example, when these criteria are analysed for single sensor placement in the 12-cell battery string, the best single sensor position is at T_s node of cell 12. The next best single sensor position is at cell 1, and the next one is at cell 11. When the criteria are used to propose placement for more sensors, the best placement is most likely to include these three sensor positions (see the four-sensor placement in Figure 3.6). The point that some observability criteria work well for single sensor placement but fail to capture information redundancy in multiple sensor placement was also identified in few references such as [26, 29].

On the other hand, placing sensors in a distributed manner does not necessarily yield better estimation performance. In this work, the combinations based on the naïve criterion, despite of dispersing the placement, actually have lower observability degree based on other criteria. The estimation performance metrics of naïve-criterion-based combinations which are less satisfactory than those of other combinations, also justify the importance of observability degree to estimation performance.

3.5. Summary

In this chapter, different observability degree criteria were applied to finding optimal temperature sensor placement in an electrochemical storage string.

Observability degree of different total number of sensors as well as that of different combinations of a given number of sensors were investigated, and its relation to estimation performance is evaluated. Although all of the tested combinations were observable, employing more sensors was demonstrated to make the system more observable. It was also demonstrated that among all possible observable combinations for the same number of sensors, different observability degree existed.

Based on two estimation performance metrics, namely average estimation RMSE and average convergence time, the data showed a positive correlation between observability degree and estimation performance. Moreover, it can be concluded that for a string temperature monitoring system, where all states need to be observed, the most suitable observability criteria are the ones which also consider smaller singular values (less observable states), such as the CN, NS, and determinant criteria. This is because these criteria ensure that all states, even the less observable ones, can be observed instead of being neglected.

An additional criterion called "Naïve" which intuitively place the sensor in a distributed manner is also evaluated. For the same number of sensors, it is found to have lower observability degree compared to other criteria. Its less satisfactory estimation performance metrics further supports the importance of observability analysis for optimal sensor placement.

Chapter 4. Multiple-Model-Estimator-Based Detection of Cell Abnormal Overheating

4.1. Introduction

As discussed in the previous chapters, one common method for monitoring temperature distribution of a device using a limited number of sensors is by estimating the remaining of the unmeasured temperature nodes based on thermal models. In this chapter, an additional feature will be proposed for the temperature monitoring system with a limited number of sensors: multiple-model-estimator-based detection of cell abnormal overheating.

Among the family of electrochemical storage devices, lithium-ion (Li-ion) batteries are one main type with more various and widespread applications. However, they have safety issues which have been a challenge for their further deployment so far. The increasing requirement for larger size and more aggressive charge-discharge cycles are hindered by Li-ion batteries vulnerability to abusive conditions, such as external heating, overcharge or overdischarge, high current charging as well as mechanical abuse like crush or impurities penetration leading to internal/external short circuit. During the past five years, a lot of Li-ion related fires and explosions were reported [101], including two events of Boeing 787 Dreamliner's battery fires [102], all of which are believed to be caused by thermal runaway, caused by a condition in which the heat produced is higher than the heat removed. In such condition, it is likely that an abnormal chemical reaction will occur due to the increasing temperature. This reaction is most likely exothermic which is a positive feedback and thus the temperature will increase even further. As the external abusive conditions triggering such initial overheating are electrical, thermal, or even mechanical, it is common that a battery management system (BMS) has incorporated sensors related to the three

types of abuse. Temperature monitoring through the temperature sensors is one of the main features in the BMS, as temperature highly affects the battery module operation and lifetime as well as safety.

This work, as well as references [18, 70, 103], used the string current for the temperature estimation. Consider a battery string in an abusive condition where the amount of current changes significantly (e.g. high current charging or external short circuit). Under this condition, it is expected that the estimator can still estimate the temperature correctly. However, certain classes of internal short circuit in a cell may lead to high current situation which probably could not be discriminated from the high operating current [49, 52], or very small short circuit which does not occur continuously [41, 50, 51], or a situation where the battery may appear normal immediately after a charge [104]. This means that a particular cell having internal short circuit may experience localised heating which is likely missed out by the estimation method based on the string current. On the other hand, this localised heating may trigger abnormal exothermic chemical reaction and abusive overheating [53, 101].

While this abnormal localised overheating –henceforth will be referred to as "abnormal overheating"– can be considered as an additional abnormal part in the heat balance equation [53, 54, 101], to the author's knowledge, so far no reference has proposed modelling the additional heat generation as unknown disturbance to the normal condition thermal model. With the possibility that the localised heating occurs at any cell, it is essential to detect not only the disturbance but also the locally overheating cell, hence making it the problem of fault detection and identification (FDI).

Multiple model estimator (MME) is one technique applied for FDI, in which a bank of estimators runs in parallel. The MME method has been demonstrated to be capable of diagnosing various faulty conditions and/or fault location in a satellite [105], aircraft [106-108], as well as microelectromechanical systems (MEMS) [109]. Despite these wide range applications, no references have proposed the MME applicability for detecting localised overheating in an

electrochemical storage string with a limited number of sensors. The use of MME for detecting such localised overheating is proposed in this chapter. The additional abnormal overheating in an internally shorted Li-ion battery cell is modelled as an unknown input disturbance. By augmenting the cell state-space model with the disturbance, the unknown additional overheating caused by the internally shorted cell can be discriminated from the overheating caused by high current operating point. Furthermore, assuming a limited number of cell surface temperature sensors, an MME is proposed to be used to quickly detect that an abnormal overheating event occurred in the battery string as well as to detect the abnormally overheating cell.

It is to be noted that this chapter's main idea originates mainly from abnormal overheating event in Li-ion cell caused by internal short circuit. The extension to the SC cell will be covered in a brief in the subsequent chapters. Thus, "cell" in this chapter is referring to Li-ion cell, unless stated otherwise.

The rest of the chapter is organised as follows. The thermal model used for both the normal and abnormal condition is briefly discussed in Section 4.2, along with an overview of disturbance modelling. Then, an MME method is explained in Section 4.3, with simulation results and discussion presented in Section 4.4. This chapter ends with a summary in Section 4.3.

4.2. Cell abnormal overheating in a string

4.2.1. Modelling of abnormal overheating as unknown disturbance

The heat balance equation such as in (2.1) or (2.2) shows that the generated heat and the released heat determine the energy balance in a cell. When the cell is heated above a certain temperature limit, exothermic chemical reactions can raise its internal temperature. If the cell can dissipate this heat, its temperature will not rise abnormally. Otherwise, the exothermic processes would proceed under adiabatic-like conditions and the cell's temperature will increase rapidly [101]. The rising temperature will further accelerate the chemical reactions,

causing even more heat to be produced, eventually resulting in thermal runaway. As discussed in section 4.1, various conditions can lead to overheating and the particular condition considered in this work is the internal short circuit in a cell.

The energy balance for thermal runaway process or internal short circuit event has been proposed in some technical papers [39, 53, 54, 101]. Although the notation used in the references is slightly different from each other, they basically consider three types of heat source: the Joule heating, the electrochemical reactions during the normal operating conditions and the abusive chemical reaction during a thermal runaway process.

Considering only the dominant heat sources, i.e. the abusive chemical reaction and Joule heating effect, and assuming that the abusive chemical reaction is most likely to occur in the internal part of the cell, the energy balance inside the cell during the thermal runaway caused by internal short circuit is as follows:

$$C_c \frac{dT_c}{dt} = Q_{\text{ab\_chem}} + Q_{\text{joule\_sc}} + Q_{\text{release}} \tag{4.1}$$

in which $Q_{\text{ab\_chem}}$ is the heat representing abusive chemical reaction in the cell, $Q_{\text{joule\_sc}}$ is the Joule heating in the cell during the internal short circuit condition, while Q_{release} is the heat released to the outer part of the cell.

For an internally shorted cell, the Joule heating term represents the energy released due to the internal short circuit. As now there is a short circuit resistance placed in parallel to the cell, the value of the I^2R term in equation (2.1) changes. Since the original thermal model does not consider this larger value of $Q_{\text{joule\_sc}}$, this "additional" term can be considered as an additive unmeasured or unknown disturbance to the normal system.

Similarly, $Q_{\text{ab\_chem}}$ is an additive term to the heat balance under the normal condition and hence it can also be modelled as an unknown disturbance to the normal system. The occurring chemical reaction is related to the characteristics of the internal short circuit, such as location and area of the short. Therefore, the onset temperature at which the chemical reactions are triggered is unpredictable

and highly dependent on the short circuit nature [54]. In this work it is assumed that the onset temperature is relatively high ($>$ 150 °C [101]), i.e. no $Q_{\text{ab\_chem}}$ is assumed to be generated up to this temperature.

4.2.2. Disturbance modelling

In control systems, the unmeasured disturbances –which can lead to steady-state offset– are often handled by augmenting the system with integrators driven by white noise [110-113].

The disturbances can be modelled to enter the system either through the plant inputs or the plant outputs or partially through both [111, 113]. Consider a linear, time-invariant, discrete-time system (4.2) augmented as in (4.3).

$$\begin{aligned} \mathbf{x}(k+1) &= \mathbf{A}\mathbf{x}(k) + \mathbf{B}\mathbf{u}(k) \\ \mathbf{y}(k) &= \mathbf{C}\mathbf{x}(k) \end{aligned} \tag{4.2}$$

$$\begin{aligned} \begin{bmatrix} \mathbf{x}(k+1) \\ \mathbf{d}(k+1) \end{bmatrix} &= \begin{bmatrix} \mathbf{A} & \mathbf{B}_d \\ 0 & \mathbf{I} \end{bmatrix} \begin{bmatrix} \mathbf{x}(k) \\ \mathbf{d}(k) \end{bmatrix} + \begin{bmatrix} \mathbf{B} \\ 0 \end{bmatrix} \mathbf{u}(k) \\ \mathbf{y}(k) &= \begin{bmatrix} \mathbf{C} & \mathbf{C}_d \end{bmatrix} \begin{bmatrix} \mathbf{x}(k) \\ \mathbf{d}(k) \end{bmatrix} \end{aligned} \tag{4.3}$$

In equations (4.2) and (4.3), $\mathbf{x}(k) \in \mathbb{R}^n$ is the state vector of the system at time k with the input vector $\mathbf{u}(k) \in \mathbb{R}^{nu}$ and the measurement vector $\mathbf{y}(k) \in \mathbb{R}^{ny}$ while $\mathbf{d}(k) \in \mathbb{R}^{nd}$ is the disturbance vector which affects the states through the matrix $\mathbf{B}_d \in \mathbb{R}^{n \times nd}$ and the measurements through the matrix $\mathbf{C}_d \in \mathbb{R}^{ny \times nd}$. A pure input disturbance model is achieved by setting $\mathbf{C}_d$ to zero while setting $\mathbf{B}_d$ to zero yields a pure output disturbance model.

Next, the detectability of the augmented system has to be verified. This step is essential as the augmented system should be detectable. Referring to [111, 112], in which detailed guidelines for the design of a general state-space disturbance model are provided, the detectability of the augmented system can be checked using the following condition:

$$\operatorname{rank}\begin{bmatrix} \mathbf{I}-\mathbf{A} & -\mathbf{B}_d \\ \mathbf{C} & \mathbf{C}_d \end{bmatrix} = n + nd \tag{4.4}$$

As the additional abnormal overheating is assumed occurring inside the cell [53, 54, 101], in this work, the system model is augmented with the input disturbance. Hence, for the discretised and augmented form of state-space model in (2.6), for N cells and ny measurements, the matrices $\mathbf{C}_d$ will be a ny-by-nd zero matrix, while $\mathbf{B}_d$ will be a $2N$-by-nd matrix whose elements are zero except for the one associated to the state affected by disturbance. For example, a 2-sensor 6-cell string assuming disturbance affecting T_{c_6} will have the following $\mathbf{C}_d$ and $\mathbf{B}_d$:

$$\begin{aligned} \mathbf{C}_d &= \begin{bmatrix} 0 & 0 \end{bmatrix}^T \\ \mathbf{B}_d &= \begin{bmatrix} 0 & 0 & 0 & 0 & 0 & 0 & 0 & 0 & 0 & 0 & 1 & 0 \end{bmatrix}^T \end{aligned} \tag{4.5}$$

4.2.3. State and Disturbance Estimation

After the additional unknown disturbance vector is added to the original system, an estimator is designed to estimate the states as well as the disturbances. For this purpose, an optimal observer, i.e. a steady-state Kalman filter, is used. It is assumed that the model in (4.3) is augmented with zero-mean white process noise $\mathbf{w}(k)$ and zero-mean white measurement noise $\mathbf{v}(k)$ as:

$$\begin{aligned} \begin{bmatrix} \mathbf{x}(k+1) \\ \mathbf{d}(k+1) \end{bmatrix} &= \begin{bmatrix} \mathbf{A} & \mathbf{B}_d \\ 0 & \mathbf{I} \end{bmatrix} \begin{bmatrix} \mathbf{x}(k) \\ \mathbf{d}(k) \end{bmatrix} + \begin{bmatrix} \mathbf{B} \\ 0 \end{bmatrix} \mathbf{u}(k) + \begin{bmatrix} \mathbf{G} & \mathbf{0} \\ \mathbf{0} & \mathbf{I} \end{bmatrix} \begin{bmatrix} \mathbf{w}(k) \\ \xi(k) \end{bmatrix} \\ \mathbf{y}(k) &= \begin{bmatrix} \mathbf{C} & \mathbf{C}_d \end{bmatrix} \begin{bmatrix} \mathbf{x}(k) \\ \mathbf{d}(k) \end{bmatrix} + \mathbf{v}(k) \end{aligned} \tag{4.6}$$

Let the covariances of $\mathbf{w}(k)$ and $\mathbf{v}(k)$ be $\mathbf{Q}_w$ and $\mathbf{R}$, respectively, and $\mathbf{w}(k)$ and $\mathbf{v}(k)$ are not cross correlated. $\mathbf{G}$ is the noise gain matrix relating the process noise to the state variables and is chosen as $\mathbf{G} = \mathbf{I}$. The disturbance is driven by white noise $\xi(k)$ with covariance $\mathbf{Q}_\xi$.

The states and disturbances are first predicted and then updated by the Kalman filter using the measured output $\mathbf{y}(k)$:

$$\begin{bmatrix} \hat{\mathbf{x}}(k+1 \mid k) \\ \hat{\mathbf{d}}(k+1 \mid k) \end{bmatrix} = \begin{bmatrix} \mathbf{A} & \mathbf{B}_d \\ \mathbf{0} & \mathbf{I} \end{bmatrix} \begin{bmatrix} \hat{\mathbf{x}}(k \mid k) \\ \hat{\mathbf{d}}(k \mid k) \end{bmatrix} + \begin{bmatrix} \mathbf{B} \\ 0 \end{bmatrix} \mathbf{u}_k$$
$$\begin{bmatrix} \hat{\mathbf{x}}(k+1 \mid k+1) \\ \hat{\mathbf{d}}(k+1 \mid k+1) \end{bmatrix} = \begin{bmatrix} \hat{\mathbf{x}}(k+1 \mid k) \\ \hat{\mathbf{d}}(k+1 \mid k) \end{bmatrix} + \begin{bmatrix} \mathbf{M}_x \\ \mathbf{M}_d \end{bmatrix} \left(\mathbf{y}(k) - \begin{bmatrix} \mathbf{C} & \mathbf{C}_d \end{bmatrix} \begin{bmatrix} \hat{\mathbf{x}}(k+1 \mid k) \\ \hat{\mathbf{d}}(k+1 \mid k) \end{bmatrix} \right) \tag{4.7}$$

Provided that the augmented system is detectable, the steady-state Kalman gain can be calculated using standard methods [110-113]. For convenience of gain calculation, the following notations are used:

$$\tilde{\mathbf{A}} = \begin{bmatrix} \mathbf{A} & \mathbf{B}_d \\ \mathbf{0} & \mathbf{I} \end{bmatrix}, \ \tilde{\mathbf{C}} = \begin{bmatrix} \mathbf{C} & \mathbf{C}_d \end{bmatrix}, \ \tilde{\mathbf{M}} = \begin{bmatrix} \mathbf{M}_x \\ \mathbf{M}_d \end{bmatrix} \tag{4.8}$$

and the steady-state gain is calculated as follows:

$$\tilde{\mathbf{M}} = \tilde{\mathbf{P}}\tilde{\mathbf{C}}^{\mathbf{T}} \left(\tilde{\mathbf{C}}\mathbf{P}\tilde{\mathbf{C}}^{\mathbf{T}} + \mathbf{R} \right)^{-1} \tag{4.9}$$

where matrix $\tilde{\mathbf{P}}$ –the error covariance matrix– is the solution to the Riccati equation

$$\tilde{\mathbf{P}} = \tilde{\mathbf{A}}\tilde{\mathbf{P}}\tilde{\mathbf{A}}^{\mathbf{T}} - \tilde{\mathbf{A}}\tilde{\mathbf{P}}\tilde{\mathbf{C}}^{\mathbf{T}} \left(\tilde{\mathbf{C}}\tilde{\mathbf{P}}\tilde{\mathbf{C}}^{\mathbf{T}} + \mathbf{R} \right)^{-1} \tilde{\mathbf{C}}\tilde{\mathbf{P}}\tilde{\mathbf{A}}^{T} + \begin{bmatrix} \mathbf{G}\mathbf{Q}_w\mathbf{G}^T & 0 \\ 0 & \mathbf{Q}_\xi \end{bmatrix} \tag{4.10}$$

4.3. Multiple Model Estimator

In Section 4.2 it was shown how the assumed affecting disturbance was modelled via pure input disturbance model $\mathbf{B}_d$ matrix. When there are N cells in a string, there are N assumptions of a cell affected by input disturbance. This is where the MM method is employed.

For FDI application, typically a bank of estimators runs in parallel, in which each estimator is designed for each possible or selected fault/failure mode [105-108]. Figure 4.1 shown N parallel estimators, each designed for the same system model but augmented with disturbance affecting one of the cells at a time. Each of the estimator model is represented by a parameter a_i where $i = 1, 2, \ldots, N$.

Based on the input **u** and the measured output **y**, the estimators (Kalman filters) produce the state estimates as in (4.7).

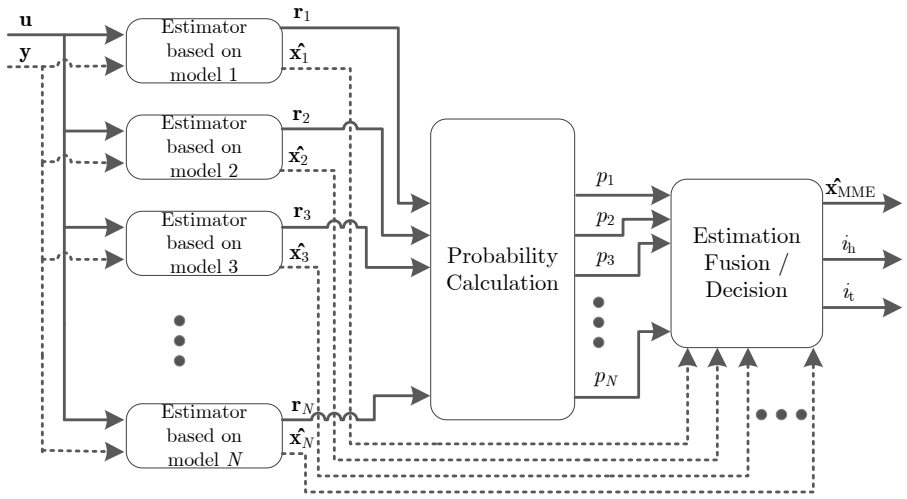

Figure 4.1. Multiple model estimator.

4.3.1. Probability calculation

In order to determine which of the states is affected by the disturbance, a conditional probability $p_i(k)$ is defined as the probability that a assumes the value a_i (i.e., the ith model is the true model), conditioned on the observed measurement history to time step k:

$$p_i\left(k\right) = \Pr\left[a = a_i \mid \mathbf{Y}\left(k\right) = \mathbf{Y}_k\right] \tag{4.11}$$

where $\mathbf{Y}(k\text{-}1) = [\mathbf{y}^T(1) \ \ldots \ \mathbf{y}^T(k\text{-}1)]^T$.

It can be shown that $p_i(k)$ can be evaluated recursively for all i via the iteration [107, 114, 115]:

$$p_i\left(k\right) = \frac{f_{\mathbf{y}(k)|a,\mathbf{Y}(k-1)}\left(\mathbf{y}_k \mid a_i, \mathbf{Y}_{k-1}\right) p_i\left(k-1\right)}{\sum_{j=1}^{I} f_{\mathbf{y}(k)|a,\mathbf{Y}(k-1)}\left(\mathbf{y}_k \mid a_i, \mathbf{Y}_{k-1}\right) p_i\left(k-1\right)} \tag{4.12}$$

where $f_{\mathbf{y}(k)|a,\mathbf{Y}(k-1)}\left(\mathbf{y}_k \mid a_i, \mathbf{Y}_{k-1}\right)$ is the conditional density function of the measurement **y** at time step k, given a certain Kalman filter model and the measurement history $\mathbf{Y}(k\text{-}1)$.

The conditional density function is given by the Gaussian form [107, 115]

$$\begin{aligned} f_{\mathbf{y}(k)|a,\mathbf{Y}(k-1)}\left(\mathbf{y}_k \mid a_i, \mathbf{Y}_{k-1}\right) &= \beta \exp\{\cdot\} \\ \beta &= \frac{1}{(2\pi)^{ny/2}\left|\mathbf{S}_i(k)\right|^{1/2}} \\ \{\cdot\} &= \{-\tfrac{1}{2}\mathbf{r}_i^T(k)\,\mathbf{S}_i^{-1}(k)\,\mathbf{r}_i(k)\} \end{aligned} \tag{4.13}$$

in which $\mathbf{r}_i(k)$ is the estimator residual given as $\mathbf{r}_i\left(k\right) = \mathbf{y}\left(k\right) - \tilde{\mathbf{C}}_i\hat{\mathbf{x}}_i$, $\mathbf{S}_i$ is the residual covariance, and ny is the measurement dimension.

In [115] it was shown that the β term in (4.13) can be removed while still leaving the algorithm to function properly, even reducing certain performance problems. Removing β term means removing inappropriate weighting based on $|\mathbf{S}_i|$ value. Thus, in this work the β term in (4.13) was removed when calculating the probability.

Since the instantaneous probability $p_i(k)$ is dependent on its previous value $p_i(k\text{-}1)$, once $p_i(k)$ reaches zero, it will cause the future time step probability to remain zero. To account for this case and allow every mode to remain active, an artificial lower bound is considered, as proposed by [106, 115, 116].

4.3.2. Estimation fusion/decision

From probability calculation in equations (4.11) to (4.13), it is clear that if a disturbance enters certain state (i.e. one of the cells), a certain mode a_i will generate smaller residuals compared to the other modes, and thus will have higher probability of being the mode that matches the real system. At each time step k, the estimated states in Figure 4.1 are set equal to the states estimated for the model with the highest probability. Similar to [106, 109], the decision logic in the estimation fusion/decision block determines the highest probability model index $i_h(k)$ at each time step k as:

$$i_h\left(k\right) \;=\; \arg\max p_i\left(k\right) \tag{4.14}$$

The final determination of the true mode index $i_t(k)$ is made using a probability threshold p_{thresh} as:

$$i_t\left(k\right) = \arg\left(p_i\left(k\right) > p_{\text{thresh}}\right) \tag{4.15}$$

Hence, the true mode index $i_t(k)$ determines the cell with abnormal overheating.

Based on the simulation results, the probability threshold value was selected as $p_{\text{thresh}} = 0.6$ as it can be expected that once a model's probability reaches this value, the tendency of that being the final true model is high.

4.4. Simulation results

4.4.1. Abnormal overheating simulation base case

The state-space model discussed in Chapter 2 and battery string thermal parameters from Section 3.4 were used for simulating a 6-cell battery cell in MATLAB. As discussed in section 4.2, to account for the heat generation in the real system, an unknown input **p** is considered in the continuous-time state-space model which yields:

$$\begin{aligned} \dot{\mathbf{x}} &= \mathbf{A}_c\mathbf{x} + \mathbf{B}_c\mathbf{u} + \mathbf{B}_{pc}\mathbf{p} \\ \mathbf{y} &= \mathbf{C}\mathbf{x} \end{aligned} \tag{4.16}$$

In (4.16) the matrices $\mathbf{B}_{pc}$ and **p** related the additional unknown heat generation $Q_{\text{add\_sc}} = Q_{\text{joule\_sc}} + Q_{\text{ab\_chem}}$ to one of the states. For example, if the cell 6 is the shorted cell (i.e. there is an additional $Q_{\text{add\_sc}}$ term added to the state), the matrices $\mathbf{B}_{pc}$ and **p** would be[5]:

[5]Alternatively, the additional heat generation can also be realised using $2N$-by-1 $\mathbf{B}_{pc}$ matrix and 1-by-1 **p** matrix.

$$\mathbf{B}_{pc} = \begin{bmatrix} \frac{1}{C_c} & 0 & 0 & 0 & \dots & 0 & 0 \\ 0 & 0 & 0 & 0 & \dots & 0 & 0 \\ 0 & 0 & \frac{1}{C_c} & 0 & \dots & 0 & 0 \\ \vdots & \vdots & \vdots & \vdots & \ddots & \frac{1}{C_c} & 0 \\ 0 & 0 & 0 & 0 & \dots & 0 & 0 \end{bmatrix} \tag{4.17}$$

$$\mathbf{p} = \begin{bmatrix} 0 \\ 0 \\ \vdots \\ Q_{\text{add\_sc}} \\ 0 \end{bmatrix} \tag{4.18}$$

where it can be seen that there is $Q_{\text{add\_sc}}$ in matrix $\mathbf{p}$ which is associated to state T_{c_6}.

Based on the observability analysis, for the 6-cell battery string, the minimum number of temperature sensors which would give an observable system is two. In the simulation the measured nodes are T_{s_3} and T_{s_6}, represented by value of 1 in the $\mathbf{C}$ matrix in (4.19). The simulated configuration is depicted in Figure 4.2.

$$\mathbf{C} = \begin{bmatrix} 0 & 0 & 0 & 0 & 0 & 1 & 0 & 0 & 0 & 0 & 0 & 0 \\ 0 & 0 & 0 & 0 & 0 & 0 & 0 & 0 & 0 & 0 & 0 & 1 \end{bmatrix} \tag{4.19}$$

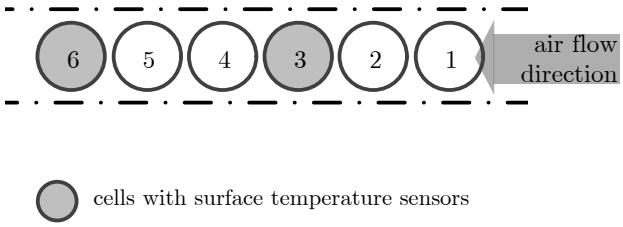

Figure 4.2. Configuration selected for simulation: 6-cell battery string with temperature sensors on cells 3 and 6.

For simulation, it is assumed that loading of the battery starts after a long rest so its initial temperature is the same as the ambient (coolant) temperature (25 °C). Then, the following load pattern is applied: 15-second charge, 5-second rest, 15-second discharge, and another 5-second rest, with the current equal to ±4 C or ±32 A for the 8-Ah battery [117]. After the load pattern is applied for about 2000 seconds, the battery reaches a steady-state operating temperature. Then, it is assumed that at time $t = 2000$ s a disturbance (the abnormal overheating) $Q_{\text{add\_sc}}$ caused by an internal short circuit initiates inside one of the cells of the battery string.

The $Q_{\text{add\_sc}}$ is modelled as a ramp signal with a rate of 5 Ws^{-1} and applied for 350 seconds from the time the disturbance initiates, with the assumption that this heat increment constitutes Joule heating followed by self-generated heating from the abusive chemical reactions. The ramp signal is selected based on the simulation of internal short circuit heat generation in [54, 118] which showed that the generated heat increases almost linearly at a certain rate. Experimentally verified simulation results from the model in [118] also showed a 1-Ah battery could have internal short circuit heat generation at a rate of approximately 0.04 Ws^{-1} to 5.77 Ws^{-1}. Hence, assuming fully charged battery cell in our work, a value of 5 Ws^{-1} is selected which is closer to the simulated maximum rate of possible heat generation.

For Kalman gain calculation, the following covariance matrices are considered:

$$\mathbf{Q}_w = \begin{bmatrix} 0.1 & 0 & \dots & 0 \\ 0 & 0.1 & \dots & 0 \\ \vdots & \vdots & \ddots & \vdots \\ 0 & 0 & 0 & 0.1 \end{bmatrix}, \qquad \mathbf{Q}_\xi = 0.01, \qquad \mathbf{R} = \begin{bmatrix} 0.1 & 0 \\ 0 & 0.1 \end{bmatrix} \tag{4.20}$$

and the steady-state Kalman gain for the augmented state-space model is calculated using (4.9) and (4.10).

The MME consists of six Kalman filters each designed for the same system model but augmented with disturbance affecting one of the cells at a time.

Similarly as in [116], the same matrix $\mathbf{S}_i$ is used for each augmented model, and is chosen as identity matrix $\mathbf{I}$ with the same dimension as the measured output. The initial probability of each augmented model is set to the same value of 1/6. The probability lower bound is set to 0.001. The covariance matrices for all estimators are the same as in (4.20) and the initial state values of the estimators are set to be the same as those of the real system.

4.4.2. Abnormal overheating detection: cell location

As a 6-cell battery string with only two temperature sensors was considered, the following two cases have been analysed. In the first case (Subsection 4.4.2.1) the shorted cell is a cell with the temperature sensor and in the second case (Subsection 4.4.2.2) the shorted cell is a cell without the temperature sensor. The results show how the probability of each augmented model evolves over time as well as the resulting states estimation for the dominant (highest) probability model.

4.4.2.1. Shorted cell is the cell with the temperature sensor

Figure 4.3 shows the probabilities $p_i(k)$ of each of the six augmented models which are used by the estimation decision block to identify the dominant probability as in (4.14). It can be seen that once the disturbance in cell 6 is introduced at time $t = 2000$ s, p_6 (the probability value of the augmented mode 6 being the true mode) increases over time to 1, while the probabilities of the others tend to 0. The probability $p_6(k)$ reaches the threshold value of 0.6 at $t = 2044$ s (after 44 seconds).

During the normal condition (before the disturbance enters), theoretically, each augmented model will have the same probability. In reality, because the residual error of each augmented model is not identical, there is a slight difference in the probability and hence the detector (see (4.14)) identifies the augmented mode 1 as having a slightly dominant probability over the others. The temperatures are estimated based on the dominant (highest) probability model

and are shown in Figure 4.4. It can be seen that before the estimation decision block yields the true model a_6, the system assumes that the true model is a_1; thus the temperature of each node of cell 1 is slightly overestimated. The probability of the true mode evolves into dominance quickly as the shorted cell 6 is the cell with the temperature sensor and hence any temperature abnormality in this cell is sensed immediately.

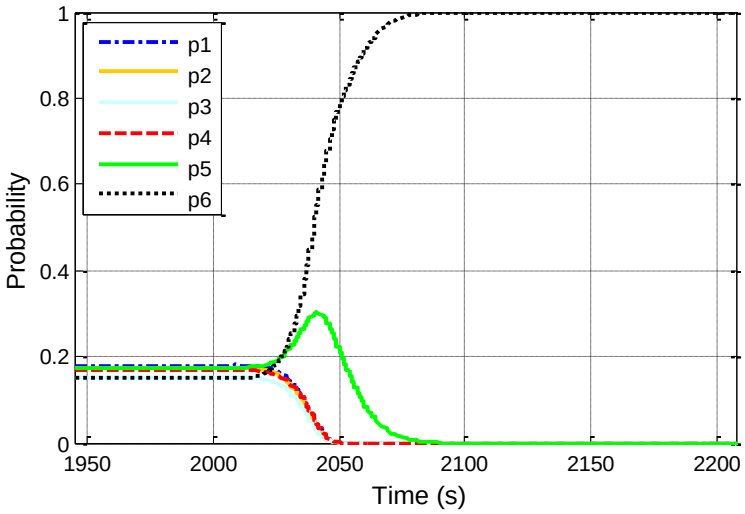

Figure 4.3. Probabilities of all six augmented models when abnormal overheating (disturbance) occurs in cell 6 at $t = 2000$ s (temperature sensors are placed on cells 3 and 6).

For the case when cell 3 is the shorted cell, the MME identifies the location of the abnormal overheating, i.e. $p_3(k)$ is greater than p_{thresh}, at $t = 2049$ s (after 49 s), as shown in Figure 4.5.

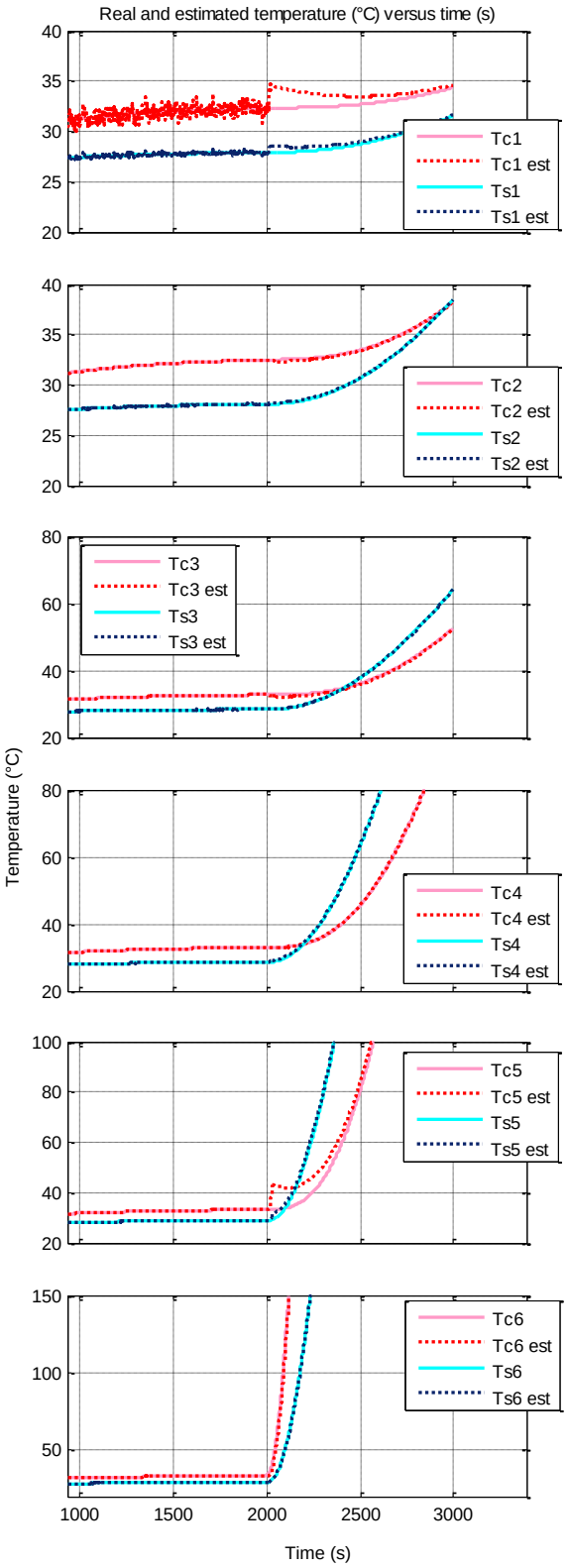

Figure 4.4. Comparison of real temperatures and temperature estimated by the MME when abnormal overheating occurs in cell 6 (temperature sensors are placed on cells 3 and 6).

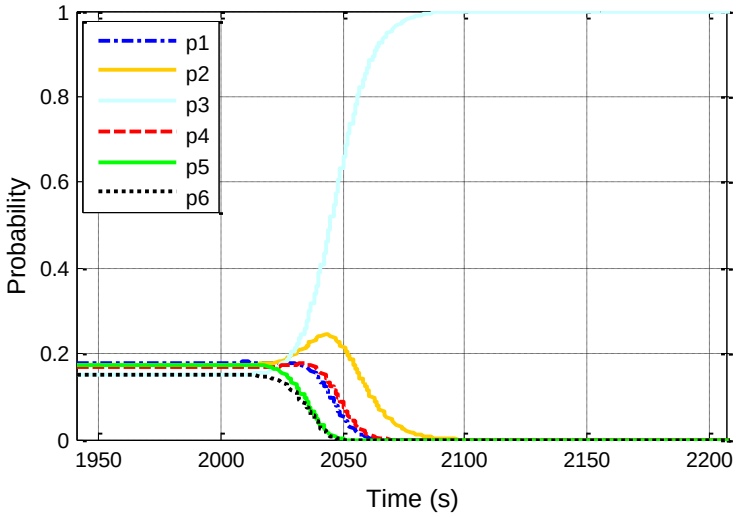

Figure 4.5. Probabilities of all six augmented models when abnormal overheating (disturbance) occurs in cell 3 at $t = 2000$ s (temperature sensors are placed on cells 3 and 6).

4.4.2.2. Shorted cell is the cell without the temperature sensors

From the previous discussion, it can be expected that if the abnormal overheating occurs in any cell at which temperature is not measured, it may take longer time until the sensor on the other cell senses the temperature abnormality.

First, the results for the case when cell 4 is overheating are shown. The probabilities of all six augmented models in Figure 4.6 show that the model a_4 takes a longer duration until its probability dominates over the other models (72 s after disturbance enters cell 4). When cell 4 experiences localised overheating, the speed of heat propagation to the nearest cell(s) with sensors depends on the heat rate and the heat transfer rate. With the selected value of the additional overheating in this simulation, p_4 value exceeds the probability threshold 0.6 at t = 2144 s (144 seconds after the disturbance affects the cell 4). The real and estimated temperatures for this case are shown in Figure 4.7.

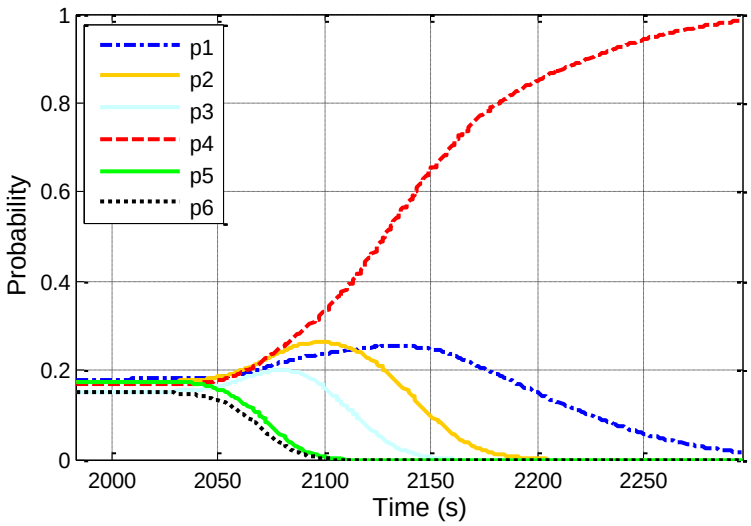

Figure 4.6. Probabilities of all six augmented models when abnormal overheating (disturbance) occurs in cell 4 at $t = 2000$ s (temperature sensors are placed on cells 3 and 6).

The probability evolutions for other cases are shown in Figure 4.8 (abnormal overheating in cell 2), Figure 4.9 (abnormal overheating in cell 5), and Figure 4.10 (abnormal overheating in cell 1). It can be noted that the MME takes considerably long time to determine that the abnormal overheating originated in cell 1. Summary of all overheating cell detection times based on the selected probability value threshold is given in the third column of the summary table (Table 4.1) in Subsection 4.4.3.

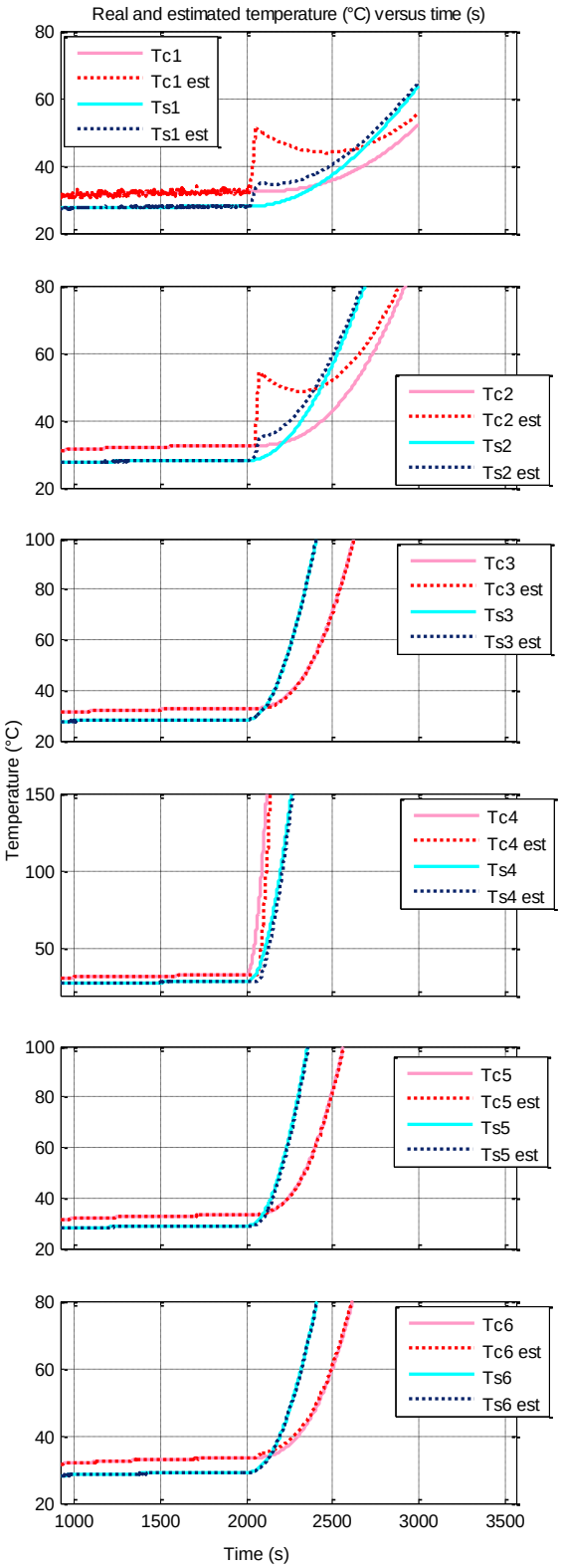

Figure 4.7. Comparison of real temperatures and temperature estimated by the MME when abnormal overheating occurs in cell 4 (temperature sensors are placed on cells 3 and 6).

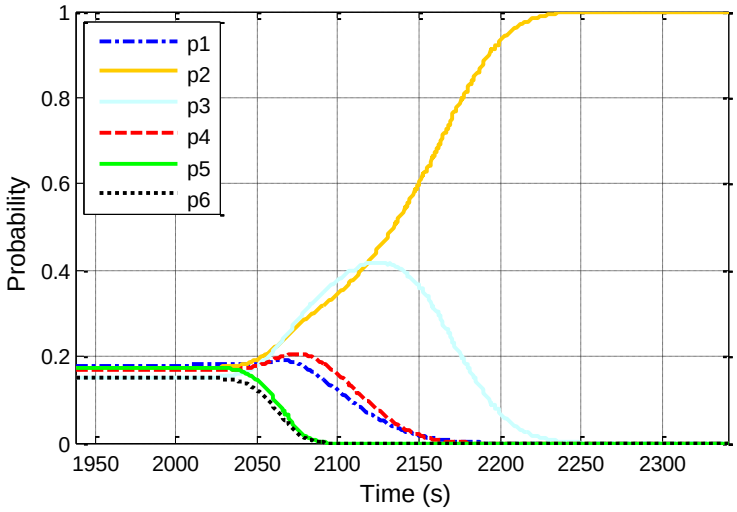

Figure 4.8. Probabilities of all six augmented models when abnormal overheating (disturbance) occurs in cell 2 at $t = 2000$ s (temperature sensors are placed on cells 3 and 6).

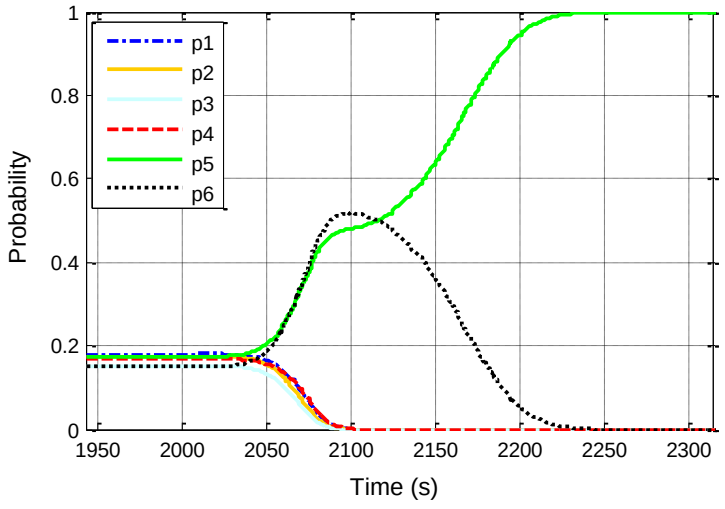

Figure 4.9. Probabilities of all six augmented models when abnormal overheating (disturbance) occurs in cell 5 at $t = 2000$ s (temperature sensors are placed on cells 3 and 6).

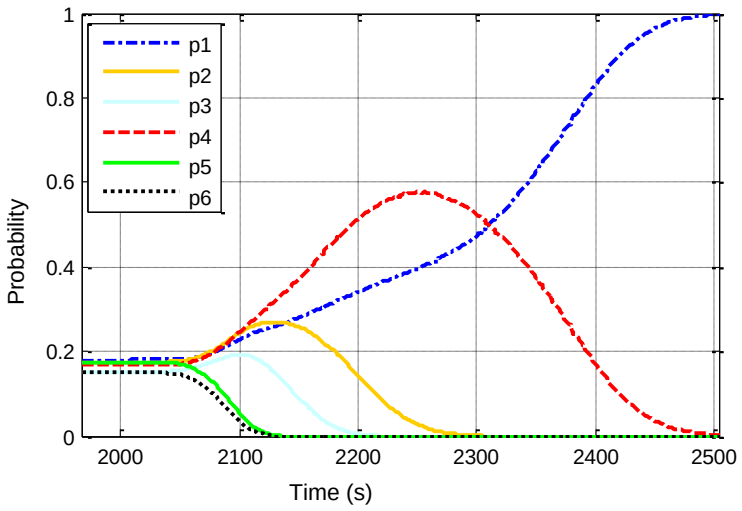

Figure 4.10. Probabilities of all six augmented models when abnormal overheating (disturbance) occurs in cell 1 at $t = 2000$ s (temperature sensors are placed on cells 3 and 6).

4.4.3. Abnormal overheating detection: the event

Despite the delay in detecting at which cell the abnormal overheating occurs, based on the estimation, the MME can immediately recognise that the temperature is increasing at different rate for different cells. A threshold can then be set as a basis for overheating alert for the BMS that an abnormal temperature rise is occurring in the battery string. This threshold can be battery cell temperature and/or the temperature difference between cells [24], and/or the temperature difference between the battery and the ambience. Here, the threshold is chosen to be the estimated core temperature difference between the cells. The maximum core temperature difference between adjacent cells during normal operation is assumed to be 1 °C (assumption based on simulation of the particular model) and hence for the 6-cell string, the threshold of core temperature difference is set to be 6 °C. Based on this threshold, the MME can alert that the highest core temperature of one cell is beyond the normal temperature difference. For example, Figure 4.11 shows a detail of the estimated core temperatures for the case when abnormal overheating occurs in cell 4. Even

before the MME has not decided yet which cell is overheating (as the probability threshold has not been reached yet), it can be seen that the estimated T_c of each cells exceeds the difference threshold. In this case, the abnormal temperature difference is detected at $t = 2037$ s (after 37 s).

Hence, using this method, the abnormal overheating event can be detected earlier before the MME identifies the particular overheating cell. Summary of all abnormal overheating detection times based on the estimated core temperature difference threshold is given in the second column of Table 4.1.

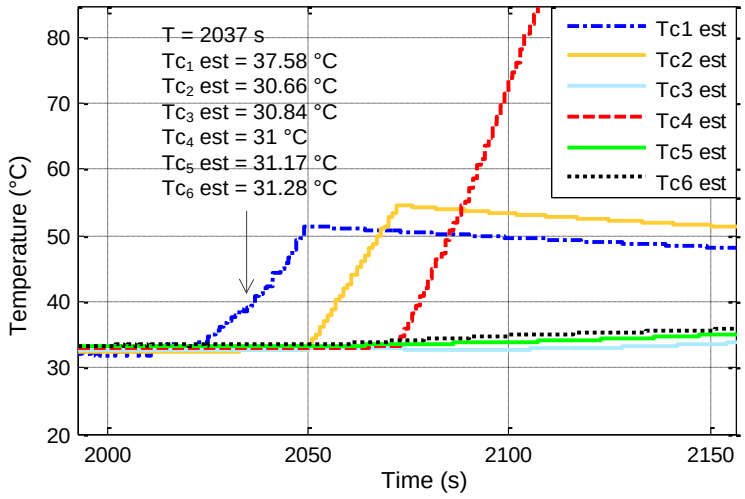

Figure 4.11. Detail of estimated core temperatures for the case when abnormal overheating (disturbance) occurs in cell 4 at $t = 2000$ s (temperature sensors are placed on cells 3 and 6).

For comparison, consider a conventional battery string in which each cell has a dedicated surface temperature sensor. Setting the threshold of surface temperature difference to 6 °C, the abnormal overheating detection time is shown in the fourth column of Table 4.1. It can be seen that relying on the surface temperature measurement takes longer time to detect abnormal overheating, as the measured surface temperature abnormal rise is in fact triggered by the core temperature abnormal rise. Considering the recently developed approach of embedding micro temperature sensors within the battery cell [119, 120], the

temperature estimation method is expected to perform better in the future, as the directly measured core temperature can be a better feedback for the estimator.

Table 4.1. Abnormal overheating detection simulation results

Abnormally overheating cell	**MME-based detection**		**Non-MME-based (assuming surface temperature sensors on each cell) detection time (s)**
	Overheating event detection time (s)	**Ovserheating cell location detection time (s)**	
Cell 1	47	345	64
Cell 2	34	151	70
Cell 3*	20	49	70
Cell 4	37	144	70
Cell 5	48	144	71
Cell 6*	27	44	60

*cell with surface temperature sensors for MME-based detection

4.4.4. MME performance for other cases

In the previous subsection, the case of one cell undergoing abnormal overheating was examined. If the possibility of more than one cell undergoing abnormal overheating is also considered, from the point of view of MME, additional modes (models) need to be added to the existing MME modes. However, assuming that the probability of more than one cell undergoing abnormal overheating caused by internal short circuit is small, it should be adequate to consider only the modes representing one cell undergoing abnormal overheating at a time.

Nevertheless, two adjacent cells undergoing abnormal overheating is simulated, employing the same MME (with only six modes) as discussed previously. Result in Table 4.2 show that even though the existing MME is used it can still detect both the abnormal overheating event and location of the overheating for the case of two adjacent cells having abnormal overheating.

Table 4.2. Detection time of abnormal overheating occurring in two adjacent cells

Abnormally overheating cell	**MME-based detection**		
	Overheating event detection time (s)	**Ovserheating location detected**	**Ovserheating cell location detection time (s)**
Cell 1 and 2	31	Cell 2	121
Cell 2 and 3*	20	Cell 3	44
Cell 3* and 4	46	Cell 3	46
Cell 4 and 5	32	Cell 5	90
Cell 5 and 6*	26	Cell 6	40

*cell with surface temperature sensors for MME-based detection

4.5. Summary

In this chapter, we propose to model the abnormal overheating caused by internally shorted cell in a battery string as an unknown input disturbance to the normal system model. For estimation purpose, the system state-space model is further augmented by an input disturbance model. An MME with several modes (augmented models) was built to detect an overheating cell using a limited number of temperature sensors. Including in the design parameters are thresholds of mode probability and temperature.

From simulations, it was shown that the MME can be used to detect which of the cells is overheating as well as to detect the abnormal overheating event in the battery string. Further exploration of the MME-based abnormal overheating detector as well as the experimentation will be presented in the subsequent chapters.

Chapter 5. Experimentation and Further Exploration of MME-Based Overheating Detection

5.1. Introduction

In Chapter 4 [61], abnormal overheating of a cell in a battery string (i.e. localised overheating) was modelled as an unknown disturbance, and with a limited number of temperature sensors, an MME was built to identify the overheating event as well as its location in the string. The idea of detecting an abnormal local hot spot in a string using the limited number of sensors is applicable to any other forced-cooled electrochemical storage string or stack consisting of a number of cells. In this chapter, the MME will be applied and tested experimentally for the SC string setup that has been introduced in Chapter 2 [62].

SCs failure modes, in particular thermal-related ones, have not been analysed in detail in many references, especially compared to batteries. As has also been explained in Subsection 1.2.3, although in general SCs are considered having less thermal risk, there are still some factors that could lead to SCs thermal hazard [55-58]. Moreover, the energy density of SCs –including its battery-hybrid type Li-ion capacitor– is reportedly getting higher, even as high as 85 Wh kg^{-1} [59, 60], and this signifies increasing thermal risk as well.

As shown in Chapter 2, from thermal dynamics point of view, as the Li-ion batteries string and the SCs string share the similar configuration (a string or stack of cylindrical cells, enclosed and forced-cooled), the thermal model and hence the thermal dynamics are similar. While the temperature distribution resulting from SCs failure modes has not been covered in references, it is assumed that it would be similar to Li-ion batteries, with few differences, e.g. in duration and magnitude, due to different thermal parameters value.

In addition, the experimentation of the MME-based overheating detection was purposely performed on an SCs string for safety reason, as, compared to batteries string, it has less risk of fire or thermal catastrophe.

Another main focus of this chapter is to further explore different design parameters, such as the Kalman filter covariance matrices of the noise model, the so-called "convergence factor", and the detection threshold. How the selection of these values affects the detection performance will also be investigated. As the application of MME in this work is quite specific, overview of the relevant literature will be presented directly in the section discussing further exploration of the MME design.

Hence, the organisation of the remainder of this chapter is as follows. Further exploration of the MME-based detection including performance evaluation and improvement is discussed in Section 5.2. The performance of the estimator/detector system is tested on the experimental setup using heaters for emulating cell overheating, which is explained in Section 5.3. Finally, the summary of this chapter is presented in Section 5.4.

5.2. Further exploration of the MME-based overheating detection design

In this section, further details not covered in Chapter 4 are investigated. This includes addition of the normal mode and the influence of noise assumption as well as convergence factor on the detection performance. Understandably, the proper choice of these parameters is very much dependent on the specific system [121, 122].

5.2.1. Additional mode representing normal condition

Many references made use of the MM method for sensor / actuator failure detection which is usually represented by making the value of a particular parameter related to that sensor or actuator to be zero (i.e. it represents the loss of a sensor or actuator). A fully functional system is represented by a nominal mode with the nominal parameter, and is usually referred to as the normal mode.

In this work, the failure (fault), instead of being represented by "zeroed" or lost parameter, is more suitable to be represented by additional parameter as previously discussed in Section 4.2 (i.e. the augmented models). This is similar to the application of MM strategy for disturbance rejection in [116]. Therefore, during the normal condition (no fault) each representing mode supposedly has very similar probability, given that the initial probability for each mode is the same. However, as the residual error of each mode at each time step is not identical, there would be a slight difference in the probability (as also shown in the simulations in Section 4.4 and also in [116]). A slight dominant probability of a mode, depending on the parameter selection, might keep increasing towards bigger value during a very long time interval and pass the probability threshold which might trigger false fault alarm.

Therefore, to improve the proposed method in Chapter 4, one mode representing the normal condition based on the original state-space model without augmented disturbance is added. Considering that the normal condition should be the default condition of the system, the initial probability of this normal mode is set to be quite high or even set to unity. An example to demonstrate this functionality will be given altogether in Subsection 5.2.2.

5.2.2. Multiplying probability with estimated disturbance for decision algorithm improvement

As shown in Figure 4.1, after probability p_i is calculated, it is fed into the so-called "Estimation Fusion/Decision" block which gives the decision of the system condition. Previously, p_i was solely used for decision algorithm in which the dominant p_i was taken into account and compared to a probability threshold (cf. equations (4.14) and (4.15)). Despite the successful overheating detection performance based on this, there are some possible cases in which the abnormal overheating extent is relatively small and causes the mode probability to evolve very slowly.

This can be demonstrated by simulation of an example with the following details. The base case for the simulation is the forced-cooled, enclosed 8-cell SC string with layout shown in Figure 5.1, with parameters as described in Chapter 2.

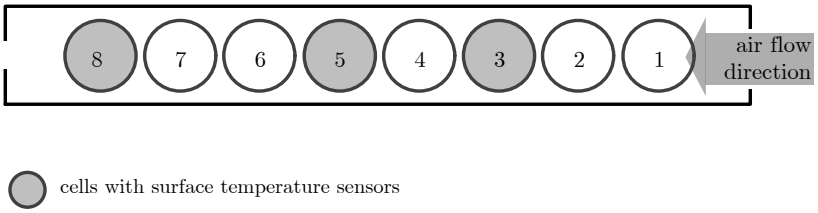

Figure 5.1. Base case for simulation and experiment: Eight-cell SC string with each grey-coloured cell having surface temperature sensor.

The load pattern is a constant current charge discharge pattern of 88 A. The simulated overheating cell is cell 1, as this can be considered the worst case for the detection, because it is the cell nearest to the cooling fan which makes the abnormally increasing temperature more difficult to sense (see Chapter 4). The additional heat source is set at $t = 2100$ s, yielding a temperature increment at cell 1 of approximately 30 °C in 300 seconds, which can be considered as a small extent of overheating.

To simulate the noises, the measurement noise with diagonal covariance matrix $\mathbf{R}$ with diagonal elements of 0.01 and the process noise with diagonal covariance matrix $\mathbf{Q}_w$ with diagonal elements of 0.0001 are added to the system. The process noise value is selected by manual tuning and comparing the simulation and experiment data.

As for the Kalman filter, the values of the covariance matrices will greatly affect the estimator gain and hence the estimation. For a base case simulation, the Kalman filter noise covariance matrix is set to be the same as the aforementioned simulated additional noise. $\mathbf{Q}_{\xi,}$ is set to be 0.00001 while the convergence factor K is chosen to be 5.

With the aforementioned parameters value, the probability evolution calculated by the MME is shown in Figure 5.2.

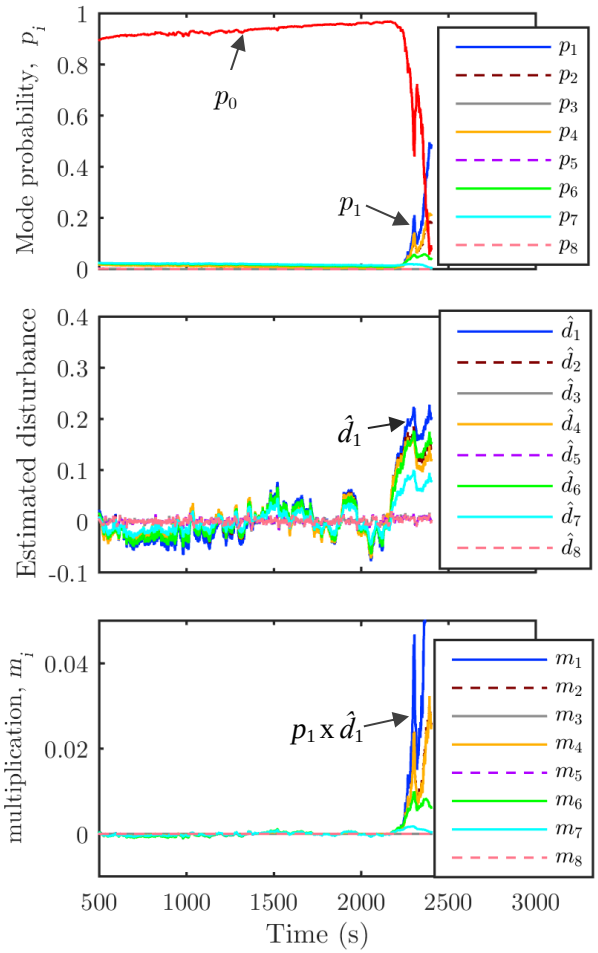

Figure 5.2. Evolution p_i (upper graph), estimated disturbance $\hat{d}_i$ (middle graph), and mode probability multiplied by estimated disturbance m_i (lower graph) for the case of overheating at cell 1 at $t = 2100$ s.

It can be seen that p_0 (normal mode probability) increases to 1 from its initial value of 0.8. When the cell 1 overheating occurs at $t = 2100$ s, p_0 starts decreasing and p_1 (cell 1 overheating mode probability) starts increasing. It might take some time before p_1 reaches the probability threshold although the overheating event can already be detected. Hence, the estimated disturbance is also utilised here for decision making.

When abnormal overheating occurs, the estimated disturbance is most likely to increase, in addition to the increment of particular disturbance-related p_i. On the other hand, during the normal condition, the disturbance-related p_i (i.e. all p_i other than p_0) is expected to evolve to a small value, which is also how the $\hat{d}_I$ is expected to be. Therefore, a multiplication of p_i with $\hat{d}_i$ (notated here as m_i) could "amplify" the small value of both p_i with $\hat{d}_i$ during normal condition as well as their increasing values when abnormal overheating takes place. Based on simulations and/or experiments, the threshold value of m_i, m_{thresh}, for abnormal overheating and location detection can be set. If all m_i are smaller than m_{thresh} then the true mode is most likely to be mode 0 (normal condition). Otherwise if any of m_i is larger than $m_{\text{thresh,}}$ it indicates that abnormal overheating is occurring.

It can be noted that the selection of m_{thresh} also poses a trade-off between a false alarm (if the m_{thresh} value is small) and a long detection time (if the m_{thresh} value is big). One alternative for this issue is to set a "duration threshold" t_{thresh}, such that an abnormal overheating is confirmed once the m_{thresh} is passed for a particular duration of time, for example 5 seconds.

Moreover, the possible overheating location can be determined based on the mode being closest to the "true mode" (real system), which is the mode with the dominant m_i. The final determination of the index of the mode being closest to the true system, $i_t(k)$, can be given as

$$i_t(k) = \begin{cases} 0, & m_i(k) < m_{\text{thresh}} \\ 0, & \left(m_i(k) > m_{\text{thresh}}\right) \text{AND (duration} < t_{thresh}) \\ \arg\max m_i(k), & \left(m_i(k) > m_{\text{thresh}}\right) \text{AND (duration} > t_{thresh}) \end{cases} \quad (5.1)$$

This determined mode can be used for the temperature estimation functionality, for which the state-space model of the corresponding determined mode is used.

5.2.3. Influence of $\mathbf{Q}_w$, $\mathbf{Q}_\xi$, R, and K to the detection

In this subsection, the influence of different parameters of the MME to p_i, d_i, and m_i is investigated. The base case is the same as explained in the Subsection 5.2.2. and the graph is shown in Figure 5.2.

Setting large **R** value implies that the noise in the measurement is considered to be large as well, resulting in small estimator gain as the estimator does not rely much on the measurement. On the other hand, setting large $\mathbf{Q}_w$ value implies that the uncertainty and/or noise in the process are considered to be large, resulting in large estimator gain as the estimator "relies" more on the measured output than on the states. While setting **R** value can be based on the measurement devices' accuracy, setting $\mathbf{Q}_w$ value can be more complicated due to limited knowledge of model inaccuracy and noises.

One notable observation is that simulation results show that when the Q/R ratio for the Kalman filter is the same, the corresponding p_i, d_i, and m_i are also the same. The Q/R ratio gives insight on how the noise or uncertainty in the process compared to the noise or uncertainty on the measurement. In fact, in many cases, it is the Q/R ratio, instead of actual values of Q and R, which determines the estimator response and hence is more of concern [116, 123-125]. In this study, for example, setting the $\mathbf{R}$ = diag (0.1, 0.1, 0.1); the $\mathbf{Q}_w$ = diag (0.001, 0.001, ..., 0.001); and $\mathbf{Q}_\xi$ = 0.0001 gives comparatively the same graph as in Figure 5.2. For comparison purpose, these values are used as the base case.

Figure 5.3(a) shows p_i, d_i, and m_i if the elements of **R** are increased. This means larger measurement noise is assumed and hence larger residual covariance is expected, which consequently causes the residual-based probability to be more fluctuating. This in turn also causes m_i to have large fluctuation.

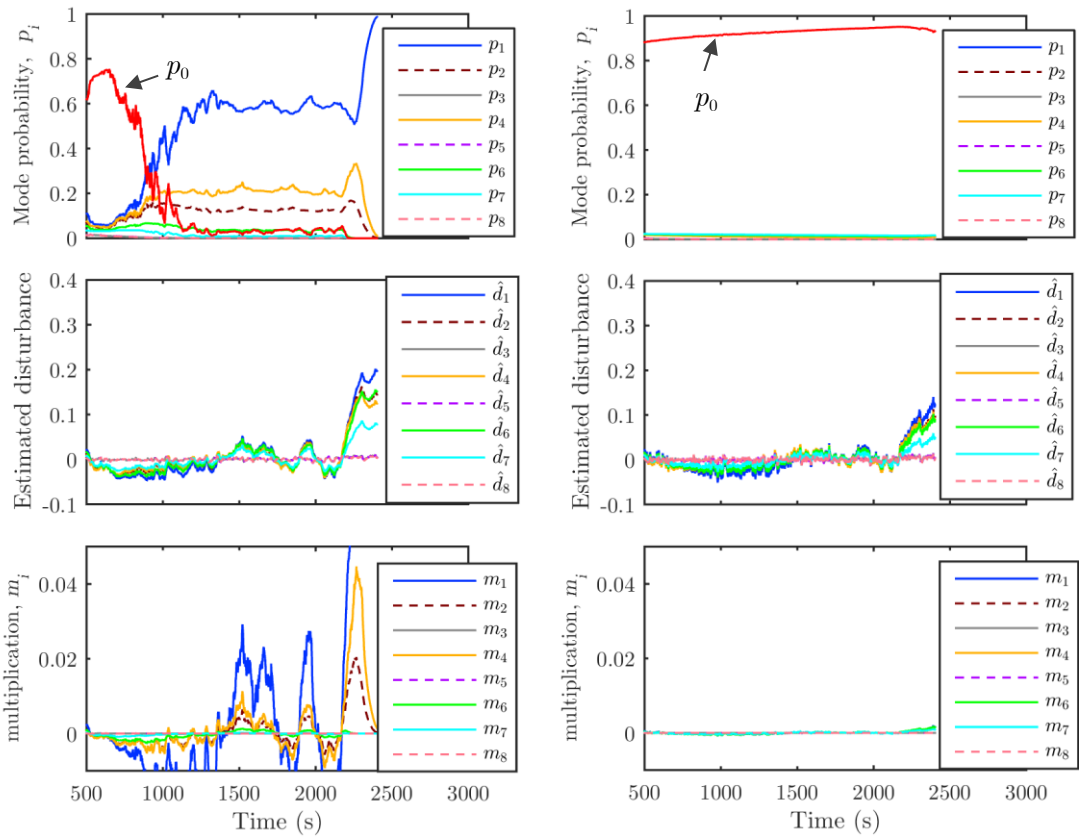

(a) (b)

Figure 5.3. Evolution of p_i (upper graph), $\hat{d}_i$ (middle graph), and m_i (lower graph) for the case of overheating at cell 1 at $t = 2100$ s. (a) $\mathbf{R}$ = diag (1, 1, 1). (b) $\mathbf{Q}_w$ = diag (0.01, 0.01, ..., 0.01).

The influence of assuming larger $\mathbf{Q}_w$ elements is shown in Figure 5.3(b). Larger $\mathbf{Q}_w$ elements imply larger process noise or parameter uncertainty and this yields in smaller estimated disturbance, as the estimator would expect that there is quite large variation in the real state variable and the difference between $\mathbf{y}$ and is mainly due to this large process noise. This yields smoother but smaller m_i as opposed to Figure 5.4(a).

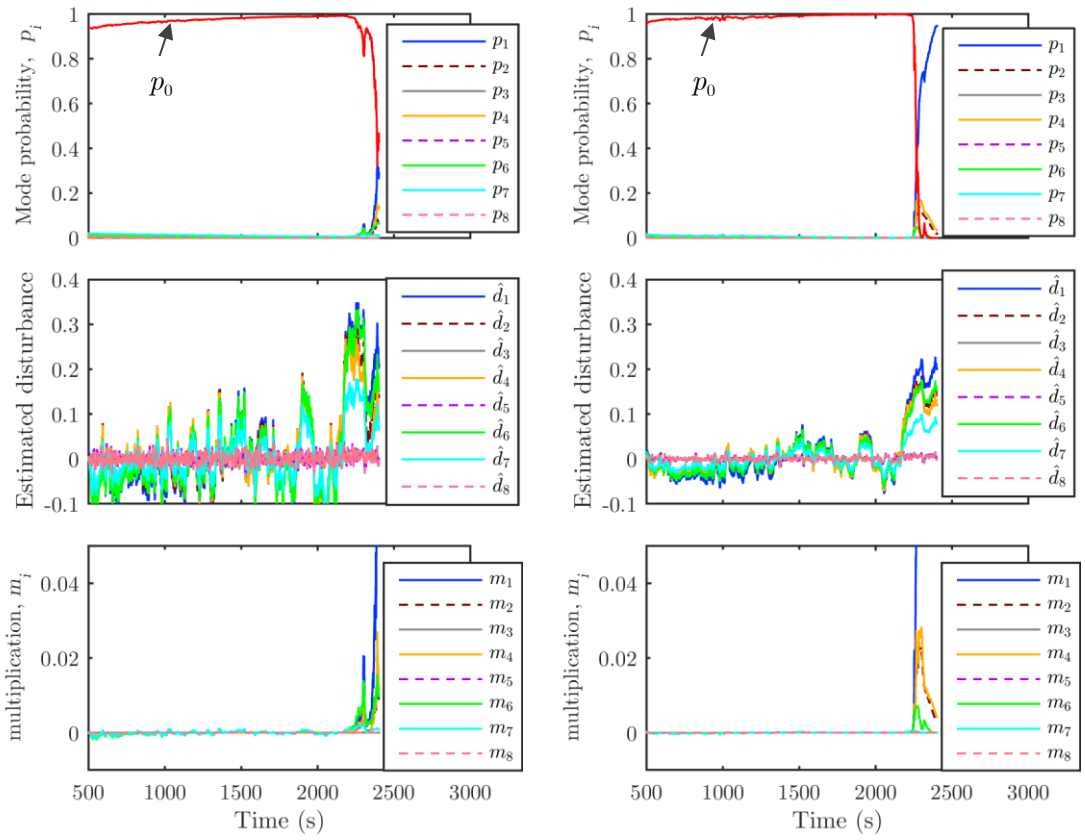

Figure 5.4. Evolution of p_i (upper graph), $\hat{d}_i$ (middle graph), and m_i (lower graph) for the case of overheating at cell 1 at $t = 2100$ s. . (a) $\mathbf{Q}_\xi = 0.001$. (b) $K = 20$.

In Figure 5.4(a), the effect of larger disturbance covariance $\mathbf{Q}_\xi$ is shown in the graphs, which is obviously seen in the large variation of the estimated disturbance. In Figure 5.4(b), the effect of the higher value of the convergence factor is depicted, and shows faster probability convergence but also larger fluctuation, as expected.

These figures can give a straightforward comparison to assist parameters value selection. Obviously, different priority (such as preference of fast detection or sensitivity) as well as different assumed system noise will yield different value selection.

5.3. Experimental studies

To evaluate the MME-based overheating detection scheme experimentally, an overheating experiment was carried out on the SC string setup. The setup, shown in Figure 5.5, with a zoomed view of a cell shown in Figure 5.6, consists of eight 650-F Maxwell BCAP0650 supercapacitors with three thermocouples each, enclosure with a fan installed at one side, and Arbin SC tester (type BT-ML) controlled with a computer.

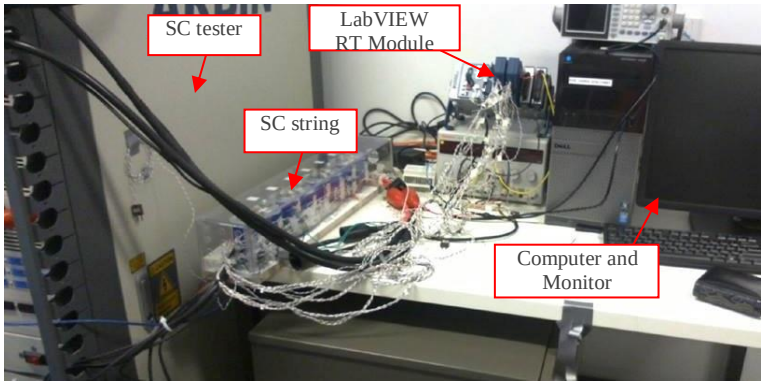

Figure 5.5. The experimental setup.

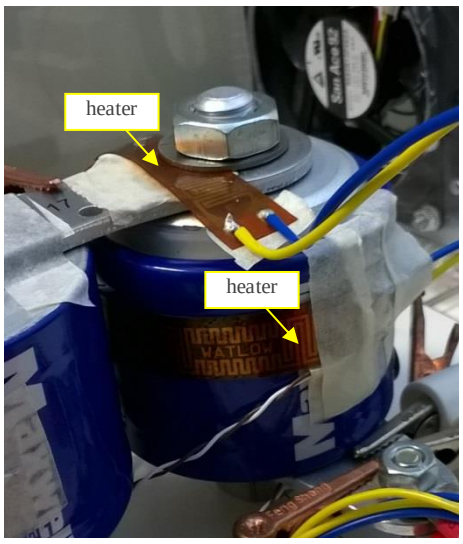

Figure 5.6. Heaters placed on the SC cell.

For the real-time application purpose, the previously discussed algorithm is rebuilt in LabVIEW 2014 Real-Time Module using cDAQ-9132 type real time controller, two NI 9214 thermocouple modules, and one NI 9205 analogue input module. In an ideal case, the experimental setup should emulate the described abnormal overheating by using a heating source installed internally inside the cell. However, this is practically very difficult to implement without physically damaging the cell and hence affecting the model parameters.

For this reason, instead, a strip polyimide heater is installed on the core/terminal thermal node T_c and the surface thermal node T_s (see Figure 5.6) and the heater power is controlled to emulate the temperature increment based on the overheating modelling. The heaters are placed in cell 1. The load pattern used for the experiment is a constant current charge discharge of 88 A.

A small temperature increase of around 30 to 50 °C with a long duration (around 300 s) is selected for the experiment. To achieve this, the heater input voltage is changed in a ramp-like increment profile consisting of three levels of value at $t = 2100$ s, $t = 2200$ s and 2300 s. With this input, the resulted d_i, p_i, and m_i up to $t = 2400$ s are shown in Figure 5.7 and Figure 5.8.

One notable highlight from the experimental result is regarding the initial condition. At the very beginning of the operation (i.e. when the SC string as well as the temperature estimator is turned on), it might take some time before the estimated states converge from the assumed initial values to the estimated values. This is most likely to happen when the system is turned on not having the condition of thermal equilibrium; for example in electric vehicle application, it gets turned on after it is off for a short period. In this case the assumed initial values of the states (cells temperature) might not be a good approximation of the real temperature of each cell which have already increased and differed. This relatively big difference at the initial time can manifest in the estimated disturbance as well as the calculated probability, as can also be seen in Figure 5.7 ($t = 0$ to around $t = 400$ s). It can be noted that if the system is started from a

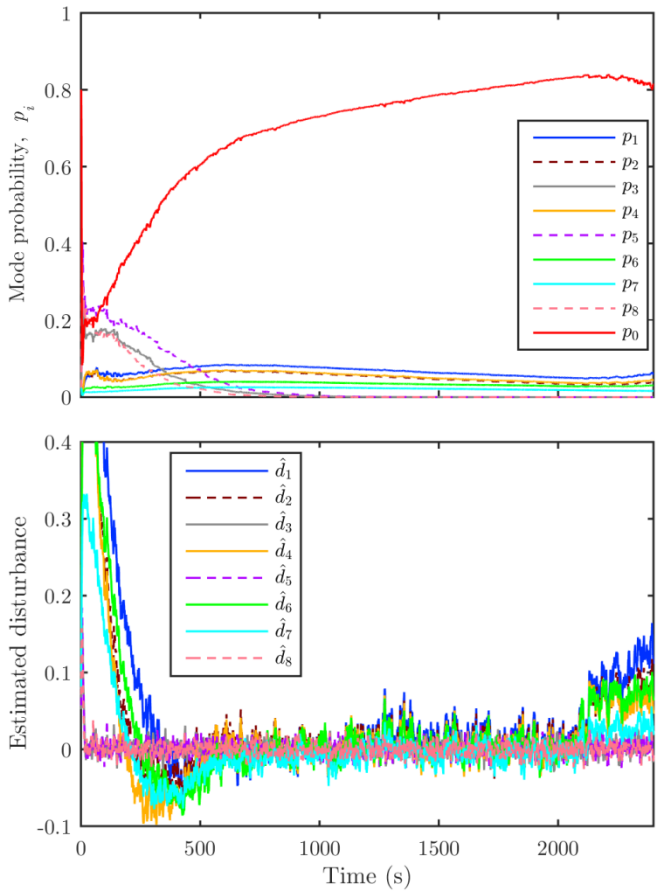

Figure 5.7. Evolution of $\hat{d}_i$ and p_i (overheating at cell 1 occurs at t = 2100 s).

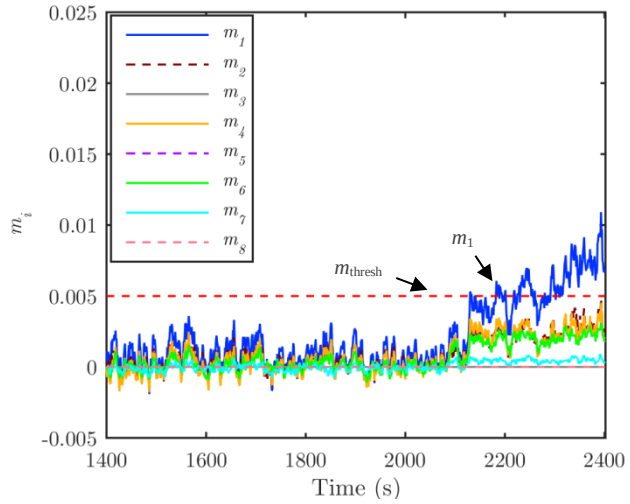

Figure 5.8. Evolution of m_i (overheating at cell 1 occurs at t = 2100 s).

thermal equilibrium (e.g. started after a long shutdown), this issue is most likely not to happen.

To address this issue, a kind of "initial time threshold" t_{thresh} can be set to disregard the m_i value bigger than m_{thresh} most likely caused by the presumed initial state value instead of real disturbance. This setting of t_{thresh} and m_{thresh}, however, poses a trade-off between the initial disturbance being undetected and a false alarm.

For this experiment, with the selected $m_{\text{thresh}} = 0.005$ and $t_{\text{thresh}} = 5$ seconds, the overheating in cell 1 is detected after 90 s. For clarity, the following graphs are redrawn and shown from $t = 1400$ s to 2400 s: the evolution of m_i in Figure 5.8, real and estimated temperature of cells 1 and 2 in Figure 5.9, and real and estimated temperature of cells 3 to 8 in Figure 5.10.

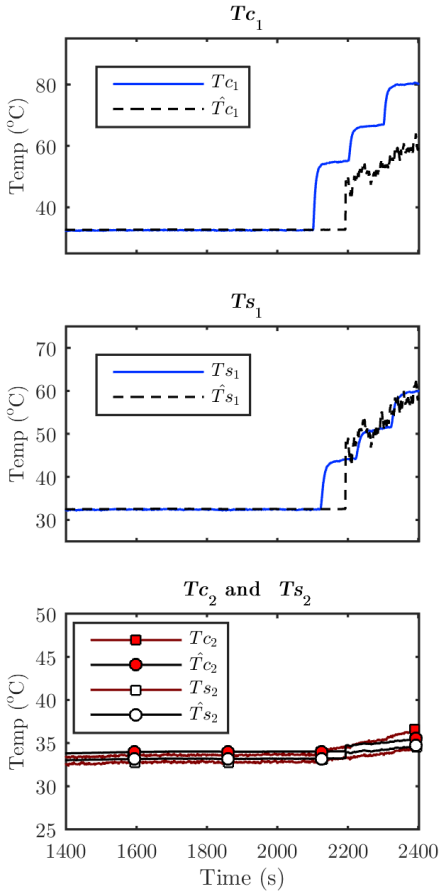

Figure 5.9. Real and estimated temperatures of cells 1 and 2 (overheating at cell 1 occurs at t = 2100 s).

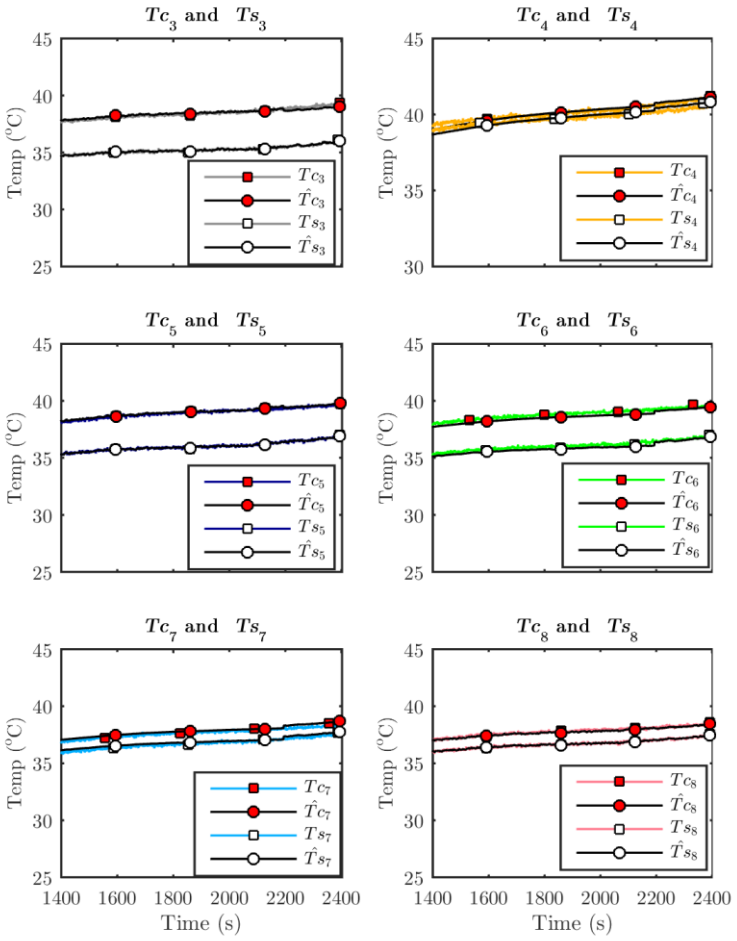

Figure 5.10. Real and estimated temperatures of cells 3 to 8 (overheating at cell 1 occurs at t = 2100 s).

As for the temperature estimation, since now the true mode decision is based on the m_i instead of solely on the p_i, as given in (5.1), the gain and the model used for estimation are based on the determined "true mode". In Figure 5.9 it can be seen that the estimator is still trying to estimate the temperature using the normal mode model up to 2190 seconds, and then it switches to mode 1.

It can be noted here that abnormal overheating indication by the estimator can be used as an early warning and initiate appropriate protection mechanism. Hence, the temperature estimation after this point is shown in Figure 5.9 and Figure 5.10 for illustrative purpose only; when the abnormal overheating event is not accommodated.

5.4. Summary

This chapter explored performance of MME-based abnormal overheating detection in an SC string with a limited number of sensors based on simulation and experimental results. Various parameters of the MME, such as the assumed noise model for the Kalman filter and the MME convergence factor, were tested to illustrate how this choice posed a trade-off between false alarm and missed detections. The presented overheating experiment results are intended to analyse how the MME method performs in an overheating event in a real setup and show that it can be a workable solution for abnormal overheating detection in a string.

Chapter 6. Abnormal Overheating Detectability Analysis Based on Cross-Gramian

6.1. Introduction

In Chapter 4 [61], a multiple-model-based method has been proposed for cell abnormal overheating detection in a string, and further explored and evaluated in Chapter 5 [63]. Meanwhile in Chapter 3 [65], different observability Gramian-based criteria have been evaluated and implemented to determine optimal sensor placement for temperature estimation in a string. Accordingly, it is interesting to study sensor placement not only for the string temperature estimation, but also for the abnormal overheating detection. As the abnormal overheating is represented as additional disturbances in the **B** matrix, the different location possibilities are represented by different **B** matrices of the system state-space model. Hence, the observability Gramian only is not enough to measure or interpret how much the disturbance will affect or be visible in the outputs, as it is dependent on the **A** and **C** matrices only.

The cross-Gramian, on the other hand, having the information from the **A**, **B**, and **C** matrices, is often used to analyse the association between a particular input to a particular output in the field of decentralised control [126, 127]. This concept can be used to quantify how much a particular additional disturbance will be visible in particular outputs.

Hence, in this work, the cross-Gramian matrix is used as the basis to analyse the association between the possible disturbance with specific sensor location. Several criteria based on the matrix are tested to assess the suitability for this particular application, with consideration of the conclusion obtained in Chapter 3 as well. The disturbance – output association is further evaluated by the detection performance of some disturbance scenarios.

The chapter's remainder is organised as follows. The disturbance detectability analysis based on cross-Gramian is explained in Section 6.2, and further implemented and evaluated for sensor placement in Section 6.3. Finally, this chapter is summarised in Section 6.4.

6.2. Disturbance detectability analysis based on cross-Gramian

Referring to section 4.4, the matrices $\mathbf{B}_{pc}$ and $\mathbf{p}$ are related to the additional abnormal heat sources in the simulation and thus added to the original state-space model as shown in (4.16). The "assignment" of the overheating cell is done through both matrices as in (4.17) and (4.18). Alternatively, a $2N$-by-1 $\mathbf{B}_{pc}$ matrix and a 1-by-1 $\mathbf{p}$ matrix can also be constructed to assign the cell being modelled as having abnormal overheating.

For example, modelling an overheating in cell 2 yields $\mathbf{B}_{pc}$ to have all zero elements except for the element related to the T_{c_2} state (i.e. the 3rd element in reference to (2.7)). Matrix $\mathbf{p}$ would have a value representing the $Q_{\text{add\_sc}}$ magnitude.

$$\mathbf{B}_{pc} = \begin{bmatrix} 0 & 0 & \dfrac{1}{C_c} & 0 & 0 & \ldots & 0 \end{bmatrix}^T \tag{6.1}$$

With N cells, there are N possible disturbance locations which are represented by N different $\mathbf{B}_{pc}$ matrixes. For convenience, the notations in equation (4.16) are rewritten as

$$\dot{\mathbf{x}} = \mathbf{A}_c\mathbf{x} + \tilde{\mathbf{B}}_c\tilde{\mathbf{u}}, \qquad \mathbf{y} = \mathbf{C}\mathbf{x} \tag{6.2}$$

where

$$\tilde{\mathbf{B}}_c = \begin{bmatrix} \mathbf{B}_c & \mathbf{B}_{pc} \end{bmatrix}, \qquad \tilde{\mathbf{u}} = \begin{bmatrix} \mathbf{u} & \mathbf{p} \end{bmatrix}^T \tag{6.3}$$

6.2.1. Cross-Gramian

For the system in (6.2), given that $\mathbf{A}_c$ matrix is stable, the observability Gramian $\mathbf{W}_O$ is defined by (3.4), while the controllability Gramian $\mathbf{W}_C$ is defined by

$$\mathbf{W}_c = \int_0^\infty e^{\mathbf{A}_c t} \tilde{\mathbf{B}}_c \tilde{\mathbf{B}}_c{}^T e^{\mathbf{A}_c{}^T t} dt \tag{6.4}$$

$\mathbf{W}_O$ quantifies how a system's states influence the outputs, thus it depends on the matrices $\mathbf{A}_c$ and $\mathbf{C}$. On the other hand, how a system's states can be brought or controlled to particular values via the inputs is quantified by $\mathbf{W}_C$, thus it depends on the matrices $\mathbf{A}_c$ and $\tilde{\mathbf{B}}_c$. The "combination" of the two matrices can be seen as combining both the controllability and observability information into a single matrix called the cross-Gramian matrix $\mathbf{W}_{CO}$ [126-129]. Given that the system (6.2) has the same number of inputs and outputs (i.e. a square system), $\mathbf{W}_{CO}$ is defined as[6]:

$$\mathbf{W}_{co} = \int_0^\infty e^{\mathbf{A}_c t} \tilde{\mathbf{B}}_c \mathbf{C} e^{\mathbf{A}_c t} dt \tag{6.5}$$

Involving the output matrix $\mathbf{C}$ and the input matrix $\tilde{\mathbf{B}}_c$, the cross-Gramian has been used for the input-output mapping / pairing in the field of decentralised control. For disturbance detectability study in this work, $\mathbf{W}_{CO}$ matrix is useful because the analysis of different sensors placement (represented by different $\mathbf{C}$ matrices) needs to be performed for the N different possibilities (represented by different $\tilde{\mathbf{B}}_c$ matrices).

---

[6]To compute cross-Gramian of a non-square system, one interesting approach proposed by some references such as [125-127] is to use the concept from input-output pairing in decentralised control, where a MIMO system is decomposed into a set of SISO subsystems, from which the cross-Gramian can be computed.

6.2.2. Different criteria of disturbance detectability based on the cross-Gramian

Subsection 3.3.2 discussed several observability criteria based on observability Gramian. Similarly, the valuable information of the Gramian matrix can be extracted from its properties as well such as rank, determinant, eigenvalues, or singular values. In addition to the literature overview related to observability criteria (see Section 3.3), the following references quantifies controllability (as well as both controllability and observability via cross-Gramian) using criterion related to the maximum or minimum eigenvalues or singular values [65, 130, 131], the sum of eigenvalues or singular values [65, 126, 131], or determinant of the matrix [65, 95, 131].

In Chapter 3 it was concluded that suitable observability criteria for string temperature estimation are those which also considers smallest singular values, which are CN, NS, and determinant criteria. Nevertheless, criterion which depends considerably on the largest singular values will also be included for evaluation in this chapter to confirm its suitability for sensor placement considering disturbance detectability.

Three criteria based on the cross-Gramian matrix are selected for comparison: CN and determinant (depends considerably on the smallest singular values; see (3.12) and (3.13)); and trace (depends considerably on the largest singular values; see (3.10)).

6.3. Implementation for sensors placement

This section discusses sensor placement suggested by the three criteria and the corresponding overheating detection performance. For this purpose, an SC string of eight cells with three sensors is considered.

6.3.1. Suggested combinations based on different criteria

First, $\mathbf{W}_{CO}$ matrix of each different sensors placement combinations and different abnormal overheating possibilities is generated. The three different

criteria are then derived from these matrices. Sensor placement combinations are then ranked. With N overheating location possibilities, there are N sets of ranked combinations based on particular criterion. Next, for each criterion, five highest ranked combinations are selected and listed on a matrix to analyse the "dispersion" of the high-ranked combinations for particular overheating location case. The most suggested combinations based on the criteria of determinant, CN, and trace, are shown in Table 6.1, Table 6.2, and Table 6.3, respectively.

Table 6.1. List of five highest-ranked sensors placement combinations based on determinant criterion

Overheating Location	Sensors Placement Combinations												
	1 4 8	2 3 8	2 4 7	2 4 8	2 5 7	2 5 8	2 6 8	3 5 8	3 6 7	3 6 8	3 7 8	4 5 8	4 6 8
Cell 1			✔	✔	✔		✔	✔					
Cell 2					✔	✔	✔	✔					✔
Cell 3					✔	✔		✔	✔	✔			
Cell 4				✔		✔	✔	✔		✔			
Cell 5							✔	✔	✔	✔		✔	
Cell 6				✔		✔	✔	✔		✔			
Cell 7					✔	✔		✔		✔			✔
Cell 8	✔	✔		✔		✔					✔		
No Overheating				✔			✔	✔				✔	✔

Red colour: Combinations selected for performance

The sensors combinations are listed in the columns and each different overheating location is listed in different rows. In each row there are five highest-ranked combinations marked by a tick mark (✔), from which we can see the combinations marked the most (i.e. being suggested as the best sensors combinations for most of the overheating cases). For example, in Table 6.1, for the case of overheating at cell 2, the five highest-ranked combinations are (2,5,7), (2,5,8), (2,6,8), (3,5,8), and (4,6,8).

It can be seen in Table 6.1, that there are a few combinations suggested by most of the overheating cases, such as (2,5,8) and (3,5,8). These combinations are marked with red colour. The same procedure is carried out for Table 6.2 and Table 6.3, where the combinations suggested the most in various cases are marked with green and blue colour in Table 6.2 and Table 6.3, respectively. These combinations are then listed in Table 6.4, and in the next subsection, the detection performance is compared. Note the difference of suggested combinations by the three criteria. A more detailed discussion on this is presented in Subsection 6.3.3. Two combinations not based on any criteria, but selected "naïvely" or intuitively are also added to the Table 6.4. In this naïve placement, sensors are "evenly distributed". These combinations are (1,5,8) and (2,4,7).

Table 6.2. List of five highest-ranked sensors placement combinations based on CN criterion

Overheating Location	Sensors Placement Combinations																				
	136	146	246	248	258	268	348	358	367	368	378	456	457	458	467	468	478	567	568	578	678
Cell 1										✔			✔		✔				✔	✔	
Cell 2										✔				✔			✔		✔	✔	
Cell 3						✔				✔						✔	✔		✔		
Cell 4										✔	✔							✔	✔		✔
Cell 5						✔				✔	✔					✔	✔				
Cell 6				✔	✔		✔	✔						✔							
Cell 7					✔			✔		✔				✔		✔					
Cell 8	✔	✔	✔						✔			✔									
No Overheating									✔							✔	✔		✔	✔	

Green colour: Combinations selected for performance evaluation.

Table 6.3. List of five highest-ranked sensors placement combinations based on trace criterion

Overheating Location	Sensors Placement Combinations																										
	1 2 6	1 2 7	1 2 8	1 3 7	1 3 8	1 7 8	2 3 6	2 3 7	2 3 8	2 4 7	2 4 8	2 5 6	2 6 7	2 7 8	3 4 6	3 4 7	3 4 8	3 5 6	3 6 7	4 5 6	4 5 7	4 5 8	4 6 7	4 7 8	5 6 7	5 6 8	5 7 8	6 7 8
Cell 1	✔	✔	✔	✔	✔																						
Cell 2							✔	✔	✔	✔	✔																
Cell 3								✔	✔						✔	✔	✔										
Cell 4															✔	✔				✔	✔	✔					
Cell 5												✔						✔		✔					✔	✔		
Cell 6													✔						✔				✔		✔		✔
Cell 7						✔								✔										✔			✔	✔
Cell 8						✔								✔										✔			✔	✔
No Overheating						✔					✔			✔										✔				✔

Blue colour: Combinations selected for performance evaluation.

6.3.2. Detection Performance Comparison

In Table 6.4, each row corresponds to a particular combination most suggested by a particular criterion. Then, the detection performance is compared using the following scenario. The abnormal overheating is modelled and simulated as presented in Chapter 4. Each combination is tested for all possible overheating locations. The additional heat source $Q_{\text{ab\_chem}}$ emulating abnormal overheating is set to initiate at $t = 2100$ s. A value of 50 W which yields relatively small heat increment (approximately 40 °C in 300 seconds at the expected hottest cell) is selected, in order to also confirm the detection sensitivity. The detection algorithm is based on MME and the decision is made from multiplication of the mode probability p_i and the estimated disturbance $\hat{d}_i$ (the multiplication is notated as m_i) as explained in Section 5.2. The threshold of this multiplication m_{thresh} as well as the time threshold t_{thresh} are selected to be 0.005 and 5 seconds, respectively.

Table 6.4. Detection Performance Comparison

Sensors Combinations based on criterion:		Overheating Location							
		Cell 1	Cell 2	Cell 3	Cell 4	Cell 5	Cell 6	Cell 7	Cell 8
Determinant	2,5,8	✚✚			✚✚			✚✚	
	3,5,8	✚✚	✚✚		✚			✚✚	
	3,6,8	✚✚	✚✚			✚✚		✚✚	
CN	4,6,8	✚		✚✚		✚		✚✚	
	5,6,8	✚	✚		✚✚			✚✚	
Trace	6,7,8	✚				✚✚			
	1,7,8						✚✚		
"Naïve" (Not based on any criterion)	1,5,8				✚✚			✚✚	
	2,4,7	✚✚		✚			✚		

The mark "✚" is defined as a performance indicator, in which the first "✚" means that the overheating is detected in less than the specified time (here, it is selected to be 180 seconds). The second "✚" means that the overheating location detected is correct. The table column in black colour indicates an SC cell having a sensor, for which case any overheating in those cells is detected almost immediately. (Note: Using the aforementioned simulation scenario, the overheating in a cell with sensor is detected in less than 20 s). For example, the (3,5,8) combination for the case of overheating at cell 2 gives "✚✚": the estimator/detector can detect an overheating in less than 180 s and the detected overheating location is correct. While for the case of overheating at cell 4, "✚" means that an overheating is detected in less than 180 s, but the location cannot be correctly determined.

6.3.3. Discussion

Analysing Table 6.1, Table 6.2, and Table 6.3, it can be seen that generally, the determinant measure suggested a more "evenly distributed" placement compared to the other two criteria. The trace criterion suggested sensors placement close to each other and it always includes a cell location corresponding to the simulated overheating cell (e.g. for overheating location at cell 1, the suggested combinations always include locating the sensor at cell 1). This can be understood as the trace criterion is based on the sum of the singular values,

which is highly affected by the largest singular value. For each overheating scenario, the largest singular value corresponds to the possible sensor placement on the overheating cell. This explains the suggested sensor locations in Table 6.3. Similarly, the CN criterion is also based on the largest singular value, but with taking into account the smallest singular values as well, which results in suggested locations in Table 6.2.

As for Table 6.4, based on the detection performance indicator discussed in Subsection 6.3.2, it can be seen that (3,6,8) give the best performance among other listed combinations, for which there is one overheating scenario (i.e. overheating in cell 4) which is detected in a longer time than the specified detection time. These combinations are most suggested by both the determinant and CN criteria. Next, it can be seen that the rest of the combinations suggested by both criteria deliver relatively similar performance, for which there is one overheating scenario detected at longer time than the specified detection time, and one or two overheating locations are misdetected.

The combinations that are most suggested by the trace criterion deliver less satisfying performance. It can be understood that the selection of sensors locations next or close to each other (e.g. in (6,7,8) or (1,7,8)) result in such redundant information which in turn makes it difficult to distinguish information from the other cells. On the other hand, although the "naïve" combinations placed the sensors in a distributed manners, they give less satisfying performance. The non-linearity of the temperature distribution of the cells in the string becomes the main reason for this, which confirms the usefulness of using the Gramian matrix for analysing the input-to-state-to-output relationship as the basis for the optimal sensors placement.

6.4. Summary

In this chapter, sensors placement for temperature estimation was studied for the purpose of abnormal overheating detection. The abnormal overheating was

modelled as an unknown additional disturbance. How the disturbance can be observed at the outputs was quantified via the cross-Gramian matrix, which then became the basis for placing the sensors. Three selected criteria based on the cross-Gramian were used and the suggested sensors placement was evaluated with different overheating simulation scenarios. Based on the specified detection performance indicator, the determinant and CN criteria delivered the most satisfying results compared to the combinations suggested by the trace criterion. These criteria consider both the most and the least observable states, which were also concluded in Chapter 3 to be the most suitable criteria for the purpose of string temperature monitoring.

A "naïve" sensor placement which intuitively placed the sensors in an evenly distributed manner along the string was also included in the evaluation matrix. This placement gave less satisfying result, as did the placement suggested by the trace criterion. These observations have confirmed the usefulness of analysing the input-to-state-to-output relationship using the cross-Gramian matrix and evaluating suitable criteria for sensors placement.

Chapter 7. Conclusions and Future Directions

7.1. Conclusions

This thesis specifically focuses on a temperature monitoring and diagnostic system for a string of electrochemical energy storage cells with a limited number of temperature sensors.

First, in Chapter 2 a thermal model of the forced-cooled string consisting of cylindrical electrochemical cells has been discussed and validated using a built SC setup. The validated model is also applicable for other types of electrochemical storage string with cylindrical cells, provided that the thermal parameters are determined accordingly. A model-based temperature monitoring system that estimates the whole string temperature based on the validated model was then utilised in the subsequent chapters.

The string observability has been analysed in Chapter 3 for the purpose of optimal sensor placement for the string temperature estimation. Different criteria based on the observability Gramian have been evaluated and it has been concluded that the suitable observability criteria for electrochemical string temperature estimation is the one which also considers the smallest singular values of the observability Gramian matrix.

In Chapter 4, method for detecting cell abnormal overheating in the forced-cooled string has been proposed. It is based on modelling of the abnormal overheating as an input disturbance and using a bank of parallel estimators called multiple model estimator (MME). The overheating simulation results have shown that the MME could detect both the overheating event and location in the string.

However, the proposed MME-based overheating detection method has longer detection time for smaller extent of overheating, or dissimilar mode probability (of abnormal overheating) during normal condition. Hence, in Chapter 5, two approaches have been proposed to shorten the detection time. One is by including

additional mode associated with normal condition; and the other one is by multiplying probability with estimated disturbance. Effect of variation of the MME parameters on the detection performance has also been explored. In the same chapter, the proposed MME has been experimentally verified using the built SC setup. The experimental results showed that the MME could be a workable solution to detect an abnormally overheating cell.

Finally, in Chapter 6, the previously discussed observability-analysis-based optimal sensor placement is adapted for the abnormal overheating detectability in the string. Instead of analysing the relationship and energy from the state to the output as discussed in Chapter 3, this chapter analysed the input-to-state-to-output relationship using the cross-Gramian matrix. Performance evaluation of the estimation and detection showed that disturbance detectability criteria which also considers the smallest singular value of the cross-Gramian matrix delivered the most satisfactory detection performance compared to other criteria. Along with Chapter 3, this chapter have also demonstrated the use of Gramian matrices as the basis for sensor placement.

7.2. Future directions

This thesis has developed and verified a lumped thermal model for a string of cylindrical electrochemical storage cells, as well as proposing the use of Gramian matrices as the basis of sensor placement for the string temperature monitoring and diagnostics. MME has also been proposed and experimentally evaluated to detect cell abnormal overheating. From the results presented in this thesis, some future works can be devised in the following directions:

1. **Extending the work to a 2-dimensional (2-D) and/or 3-dimensional (3-D) stack:** This thesis considered a 1-dimensional (1-D) storage string. The described research work is also applicable to a 2-D stack in which the temperature distribution in the spanwise direction (perpendicular to the air flow) is relatively small. A model considering detailed temperature

distribution in the spanwise direction would further enhance the 2-D model accuracy. Furthermore, sensor placement and overheating detection methods proposed in this thesis would have to be verified for their applicability to the 2-D and/or 3-D stack.

2. **Considering thermal parameters variation over time and/or space:** The parameters of thermal model in this thesis are assumed to be constant. However, some of the parameters such as the cell internal resistance can change over time. Hence, an adaptive thermal model or a time-varying model would be able to track the model's parameters over time.

3. **Improving the temperature estimation and overheating detection by modelling the shutdown period:** In this thesis, one challenge related to string temperature monitoring and diagnostics is the initial estimate, especially when there is already an unknown temperature distribution in the string (e.g. after a short shutdown). An advanced thermal model taking into account different cooling stages (including the off stage during the shutdown period), combined with a timer-like feature, could model the thermal dynamics during the shutdown period. Hence, it can enhance the accuracy of the initial estimate when the string is started up and therefore improve the overheating detection during initial operation.

4. **Evaluation and strategies for the MME with a high number of cells:** For an N-cell string, the MME for detecting abnormal overheating proposed in this thesis have N number of modes (plus 1 normal mode). Thus, for a string having a high number of cells, strategies for designing an effective MME need to be considered. Performance and possible issues related to a high number of modes also needs to be evaluated further.

5. **More detailed evaluation of the abnormal overheating modelling:** In this thesis, the abnormal overheating considered is the localised overheating caused by an internal short circuit and modelled as an input disturbance in the internal temperature node. With the growing –albeit slowly– numbers of references reporting data from short-circuit experiments, the modelling proposed in this thesis could be further improved; for example by adjusting the $Q_{\text{add\_chem}}$ value over time.

6. **Improved abnormal overheating experimentation:** Due to practical challenges and for safety reasons, heater strips have been used in this thesis to emulate the temperature increment caused by internal short circuit. While researches on the methods for performing experimental simulation of short-circuit are still growing, an improved experimental method with higher repeatability would contribute more to evaluation of the proposed method.

7. **Incorporating the temperature monitoring and diagnostics with electrical parameters measurement:** The works in this thesis are specifically based on thermal parameters. The advantage is that they can also be applied to thermal-related monitoring systems of other devices or equipment. On the other hand, electrical parameters measurement/monitoring is a typical feature included for batteries and SCs systems. As most of the string failure modes are related to the electrical parameters, incorporating these parameters for the string abnormality diagnostics could improve the detection performance.

Bibliography

[1] S. Sharifi and T. S. Rosing, "Accurate Direct and Indirect On-Chip Temperature Sensing for Efficient Dynamic Thermal Management," *IEEE Trans. Comput.-Aided Design Integr. Circuits Syst.,* vol. 29, pp. 1586-1599, 2010.

[2] Z. Changyun, G. Zhenyu, S. Li, R. P. Dick, and R. Joseph, "Three-Dimensional Chip-Multiprocessor Run-Time Thermal Management," *IEEE Trans. Comput.-Aided Design Integr. Circuits Syst.,* vol. 27, pp. 1479-1492, 2008.

[3] C. Huifeng, J. Bing, V. Pickert, and C. Wenping, "Real-Time Temperature Estimation for Power MOSFETs Considering Thermal Aging Effects," *IEEE Trans. Device Mater. Rel.,* vol. 14, pp. 220-228, 2014.

[4] M. Musallam and C. M. Johnson, "Real-Time Compact Thermal Models for Health Management of Power Electronics," *IEEE Trans. Power Electron. ,* vol. 25, pp. 1416-1425, 2010.

[5] S. Nategh, H. Zhe, A. Krings, O. Wallmark, and M. Leksell, "Thermal Modeling of Directly Cooled Electric Machines Using Lumped Parameter and Limited CFD Analysis," *IEEE Trans. Energy Convers.,* vol. 28, pp. 979-990, 2013.

[6] Z. Wei, A. E. Goulart, M. Falahi, and P. Rondla, "Development of a Low-Cost Self-Diagnostic Module for Oil-Immerse Forced-Air Cooling Transformers," *IEEE Trans. Power Del.,* vol. 30, pp. 129-137, 2015.

[7] A. Salah, J. Gaber, R. Outbib, O. Serres, and H. El-Sayed, "Modeling and Simulation of PEM Fuel Cell Thermal Behavior on Parallel Computers," *IEEE Trans. Energy Conv.,* vol. 25, pp. 768-777, 2010.

[8] X. Ying, "Model-Based Virtual Thermal Sensors for Lithium-Ion Battery in EV Applications," *IEEE Trans. Ind. Electron.,* vol. 62, pp. 3112-3122, 2015.

[9] M. Al Sakka, H. Gualous, J. Van Mierlo, and H. Culcu, "Thermal modeling and heat management of supercapacitor modules for vehicle applications," *J. Power Sources,* vol. 194, pp. 581-587, 12/1/ 2009.

[10] S. Vazquez, S. M. Lukic, E. Galvan, L. G. Franquelo, and J. M. Carrasco, "Energy Storage Systems for Transport and Grid Applications," *IEEE Trans. Ind. Electron.,* vol. 57, pp. 3881-3895, 2010.

[11] M. Uno and K. Tanaka, "Accelerated charge-discharge cycling test and cycle life prediction model for supercapacitors in alternative battery applications," *IEEE Trans. Ind. Electron.,* vol. 59, pp. 4704-4712, 2012.

[12] W. Lajnef, J. M. Vinassa, O. Briat, H. E. Brouji, S. Azzopardi, and E. Woirgard, "Quantification of ageing of ultracapacitors during cycling tests with current profile characteristics of hybrid and electric vehicles applications," *IET Electric Power Appl.,* vol. 1, p. 683, 2007.

[13] A. Eddahech, M. Ayadi, O. Briat, and J.-M. Vinassa, "Online parameter identification for real-time supercapacitor performance estimation in automotive applications," *International J. of Electrical Power and Energy Systems,* vol. 51, pp. 162-167, 10// 2013.

[14] A. Etxeberria, I. Vechiu, H. Camblong, and J. M. Vinassa, "Hybrid Energy Storage Systems for renewable Energy Sources Integration in microgrids: A review," in *IPEC, 2010 Conference Proceedings*, 2010, pp. 532-537.

[15] K. W. Wee, S. S. Choi, and D. M. Vilathgamuwa, "Design of a renewable - hybrid energy storage power scheme for short-term power dispatch," in *Electric Utility Deregulation and Restructuring and Power Technologies (DRPT), 2011 4th International Conference on*, 2011, pp. 1511-1516.

[16] B. Hredzak, V. G. Agelidis, and J. Minsoo, "A Model Predictive Control System for a Hybrid Battery-Ultracapacitor Power Source," *IEEE Trans. Power Electron, ,* vol. 29, pp. 1469-1479, 2014.

[17] G. Xiong, A. Kundu, and T. S. Fisher, "Thermal Management in Electrochemical Energy Storage Systems," in *Thermal Effects in Supercapacitors*, ed Cham: Springer International Publishing, 2015, pp. 1-10.

[18] X. Lin, H. Fu, H. E. Perez, J. B. Siege, A. G. Stefanopoulou, Y. Ding*, et al.*, "Parameterization and Observability Analysis of Scalable Battery Clusters for Onboard Thermal Management," *Oil Gas Sci. Technol. – Rev. IFP Energies nouvelles,* vol. 68, pp. 165-178, 2013.

[19] "125V Modules Datasheet," ed: Maxwell Technologies.

[20] N. Ultracapacitors, "NESSCAP® Ultracapacitor Products 125V MODULES," ed: Nesscap Ultracapacitors.

[21] (June). *A123 Systems Power Core Pack (110kW).* Available: http://www.a123systems.com/products-systems-power-core-pack.htm

[22] S. Park and D. Jung, "Battery cell arrangement and heat transfer fluid effects on the parasitic power consumption and the cell temperature distribution in a hybrid electric vehicle," *J. Power Sources,* vol. 227, pp. 191-198, 4/1/ 2013.

[23] I. Voicu, H. Louahlia, H. Gualous, and R. Gallay, "Thermal management and forced air-cooling of supercapacitors stack," *Applied Thermal Engineering,* vol. 85, pp. 89-99, 6/25/ 2015.

[24] R. Mahamud and C. Park, "Reciprocating air flow for Li-ion battery thermal management to improve temperature uniformity," *J. Power Sources,* vol. 196, pp. 5685-5696, 7/1/ 2011.

[25] A. Hijazi, P. Kreczanik, E. Bideaux, P. Venet, G. Clerc, and M. Di Loreto, "Thermal Network Model of Supercapacitors Stack," *IEEE Trans. Ind. Electron.,* vol. 59, pp. 979-987, 2012.

[26] C. Sumana and C. Venkateswarlu, "Optimal selection of sensors for state estimation in a reactive distillation process," *J. of Process Control,* vol. 19, pp. 1024-1035, 6// 2009.

[27] F. W. J. van den Berg, H. C. J. Hoefsloot, H. F. M. Boelens, and A. K. Smilde, "Selection of optimal sensor position in a tubular reactor using robust degree of observability criteria," *Chem. Eng. Sci.,* vol. 55, pp. 827-837, 2000.

[28] A. K. Singh and J. Hahn, "Determining Optimal Sensor Locations for State and Parameter Estimation for Stable Nonlinear Systems," *Industrial & Eng. Chemistry Research,* vol. 44, pp. 5645-5659, 2005.

[29] M. Serpas, G. Hackebeil, C. Laird, and J. Hahn, "Sensor location for nonlinear dynamic systems via observability analysis and MAX-DET optimization," *Computers & Chem. Eng.,* vol. 48, pp. 105-112, 1/10/ 2013.

[30] M. Weickgenannt, S. Neuhaeuser, B. Henke, W. Sobek, and O. Sawodny, "Optimal sensor placement for state estimation of a thin double-curved shell structure," *Mechatronics,* vol. 23, pp. 346-354, 4// 2013.

[31] J. Borggaard, J. Burns, and L. Zietsman, "On using LQG performance metrics for sensor placement," in *American Control Conference (ACC), 2011*, 2011, pp. 2381-2386.

[32] J. Ranieri, A. Vincenzi, A. Chebira, D. Atienza, and M. Vetterli, "EigenMaps: Algorithms for optimal thermal maps extraction and sensor placement on multicore processors," in *Design Automation Conference (DAC), 2012 49th ACM/EDAC/IEEE*, 2012, pp. 636-641.

[33] A. N. Nowroz, R. Cochran, and S. Reda, "Thermal monitoring of real processors: Techniques for sensor allocation and full characterization," in *Design Automation Conference (DAC), 2010 47th ACM/IEEE*, 2010, pp. 56-61.

[34] A. J. Lee and U. M. Diwekar, "Optimal sensor placement in integrated gasification combined cycle power systems," *Applied Energy,* vol. 99, pp. 255-264, 11// 2012.

[35] H. Cheng, X. Li, J. Jiang, Z. Deng, J. Yang, and J. Li, "A nonlinear sliding mode observer for the estimation of temperature distribution in a planar solid oxide fuel cell," *International Journal of Hydrogen Energy,* vol. 40, pp. 593-606, 1/5/ 2015.

[36] N. A. Samad, J. B. Siegel, A. G. Stefanopoulou, and A. Knobloch, "Observability analysis for surface sensor location in encased battery cells," in *American Control Conference (ACC), 2015*, 2015, pp. 299-304.

[37] P. Wolf, S. Moura, and M. Krstic, "On optimizing sensor placement for spatio-temporal temperature estimation in large battery packs," in *Decision and Control (CDC), 2012 IEEE 51st Annual Conference on*, 2012, pp. 973-978.

[38] L. Maodeng, W. Dayi, and H. Xiangyu, "Study on the observability analysis based on the trace of error covariance matrix for spacecraft autonomous navigation," in *Control and Automation (ICCA), 2013 10th IEEE International Conference on*, 2013, pp. 95-98.

[39] X. Feng, C. Weng, M. Ouyang, and J. Sun, "Online internal short circuit detection for a large format lithium ion battery," *Applied Energy,* vol. 161, pp. 168-180, 1/1/ 2016.

[40] B. Xia, C. Mi, Z. Chen, and B. Robert, "Multiple cell lithium-ion battery system electric fault online diagnostics," in *Transportation Electrification Conference and Expo (ITEC), 2015 IEEE*, 2015, pp. 1-7.

[41] M. Ouyang, M. Zhang, X. Feng, L. Lu, J. Li, X. He*, et al.*, "Internal short circuit detection for battery pack using equivalent parameter and consistency method," *Journal of Power Sources,* vol. 294, pp. 272-283, 10/30/ 2015.

[42] A. Sidhu, A. Izadian, and S. Anwar, "Adaptive Nonlinear Model-Based Fault Diagnosis of Li-Ion Batteries," *IEEE Trans. on Ind. Electron.,* vol. 62, pp. 1002-1011, 2015.

[43] R. Wang, "Lithium ion battery failure detection using temperature difference between internal point and surface," M.S. Thesis, Purdue University, West Lafayette, United States, 2011.

[44] D. Torregrossa, K. E. Toghill, V. Amstutz, H. H. Girault, and M. Paolone, "Macroscopic indicators of fault diagnosis and ageing in electrochemical double layer capacitors," *J. of Energy Storage,* vol. 2, pp. 8-24, 8// 2015.

[45] J. Li, G. Wang, L. Wu, and X. Li, "On-line fault-diagnosis study: Model-based fault diagnosis for ultracapcitors," in *2014 Prognostics and System Health Management Conference (PHM-2014 Hunan)*, 2014, pp. 158-162.

[46] A. E. Mejdoubi, A. Oukaour, H. Chaoui, Y. Slamani, J. Sabor, and H. Gualous, "Online Supercapacitor Diagnosis for Electric Vehicle Applications," *IEEE Trans. on Veh. Technol.,* vol. PP, pp. 1-1, 2015.

[47] V. K. Muddappa and S. Anwar, "Electrochemical model based fault diagnosis of li-ion battery using fuzzy logic," in *ASME 2014 International Mechanical Engineering Congress and Exposition*, 2014, pp. V04BT04A048-V04BT04A048.

[48] M. A. Rahman, S. Anwar, and A. Izadian, "Electrochemical model based fault diagnosis of a lithium ion battery using multiple model adaptive estimation approach," in *Industrial Technology (ICIT), 2015 IEEE International Conference on*, 2015, pp. 210-217.

[49] D. H. Doughty, "Battery Safety and Abuse Tolerance," in *Handbook of Battery Materials*, ed: Wiley-VCH Verlag GmbH & Co. KGaA, 2011, pp. 905-938.

[50] G. Pistoia, "Chapter 18: Safety of Lithium-Ion Batteries," in *Lithium-Ion Batteries: Advances and Applications*, ed Oxford, UK: Elsevier, 2013.

[51] K. Yokotani, "Battery system and method for detecting internal short circuit in battery system," US 8,643,332 B2, 2014, Feb 4., 2014.

[52] W. A. Hermann and S. I. Kohn, "Detection of over-current shorts in a battery pack using pattern recognition," US 8,618,775 B2, 2013, Dec 31, 2013.

[53] H. Maleki and J. N. Howard, "Internal short circuit in Li-ion cells," *J. Power Sources,* vol. 191, pp. 568-574, 6/15/ 2009.

[54] S. Santhanagopalan, P. Ramadass, and J. Zhang, "Analysis of internal short-circuit in a lithium ion cell," *J. Power Sources,* vol. 194, pp. 550-557, 10/20/ 2009.

[55] G. Walden, J. Stepan, and C. Mikolajczak, "Safety considerations when designing portable electronics with Electric Double-Layer Capacitors (Supercapacitors)," in *Product Compliance Engineering (PSES), 2011 IEEE Symposium on*, 2011, pp. 1-5.

[56] T. Brousse, P.-L. Taberna, O. Crosnier, R. Dugas, P. Guillemet, Y. Scudeller*, et al.*, "Long-term cycling behavior of asymmetric activated carbon/MnO2 aqueous electrochemical supercapacitor," *J. Power Sources,* vol. 173, pp. 633-641, 11/8/ 2007.

[57] A. I. Belyakov and D. A. Sojref, "High power supercapacitor's solutions for reliable power supply," in *Power Engineering, Energy and Electrical Drives, 2009. POWERENG '09. International Conference on*, 2009, pp. 348-352.

[58] M. Ayadi, O. Briat, A. Eddahech, R. German, G. Coquery, and J. M. Vinassa, "Thermal cycling impacts on supercapacitor performances during calendar ageing," *Microelectronics Reliability,* vol. 53, pp. 1628-1631, 9// 2013.

[59] W. Zhang, C. Ma, J. Fang, J. Cheng, X. Zhang, S. Dong*, et al.*, "Asymmetric electrochemical capacitors with high energy and power density based on graphene/CoAl-LDH and activated carbon electrodes," *RSC Advances,* vol. 3, pp. 2483-2490, 2013.

[60] C. Liu, Z. Yu, D. Neff, A. Zhamu, and B. Z. Jang, "Graphene-Based Supercapacitor with an Ultrahigh Energy Density," *Nano Letters,* vol. 10, pp. 4863-4868, 2010/12/08 2010.

[61] V. Lystianingrum, B. Hredzak, and V. G. Agelidis, "Multiple model estimator based detection of abnormal cell overheating in a Li-ion battery string with

minimum number of temperature sensors," *J. Power Sources,* vol. 273, pp. 1171-1181, 1/1/ 2015.

[62] V. Lystianingrum, B. Hredzak, V. G. Agelidis, and V. S. Djanali, "On Estimating Instantaneous Temperature of a Supercapacitor String Using an Observer Based on Experimentally Validated Lumped Thermal Model," *IEEE Trans. Energy Conv.,* vol. PP, pp. 1-11, 2015.

[63] V. Lystianingrum, B. Hredzak, and V. G. Agelidis, "Multiple-Model-Based Overheating Detection in a Supercapacitors String," *IEEE Trans. Energy Conv.,* vol. PP, pp. 1-1, 2016.

[64] V. Lystianingrum, V. G. Agelidis, and B. Hredzak, "State of health and life estimation methods for supercapacitors," in *Power Engineering Conference (AUPEC), 2013 Australasian Universities*, 2013, pp. 1-7.

[65] V. Lystianingrum, B. Hredzak, V. G. Agelidis, and V. S. Djanali, "Observability degree criteria evaluation for temperature observability in a battery string towards optimal thermal sensors placement," in *Intell. Sensors, Sensor Netw. Inf. Process. (ISSNIP), 2014 IEEE Ninth International Conf.*, 2014, pp. 1-6.

[66] V. Lystianingrum, B. Hredzak, and V. G. Agelidis, "Abnormal Overheating Detectability Analysis Based on Cross Gramian for a Superacapacitors String," in *Power & Energy Society General Meeting, 2015 IEEE*, 2016.

[67] H. Gualous, H. Louahlia, and R. Gallay, "Supercapacitor Characterization and Thermal Modelling With Reversible and Irreversible Heat Effect," *IEEE Transactions on Power Electronics,* vol. 26, pp. 3402-3409, 2011.

[68] A. Taniguchi, N. Fujioka, M. Ikoma, and A. Ohta, "Development of nickel/metal-hydride batteries for EVs and HEVs," *J. Power Sources,* vol. 100, pp. 117-124, 11/30/ 2001.

[69] "Electrochemical Supercapacitor Design, Fabrication, and Operation," in *Electrochemical Supercapacitors for Energy Storage and Delivery*, ed: CRC Press, 2013, pp. 203-246.

[70] L. Xinfan, H. E. Perez, J. B. Siegel, A. G. Stefanopoulou, L. Yonghua, R. D. Anderson, *et al.*, "Online Parameterization of Lumped Thermal Dynamics in Cylindrical Lithium Ion Batteries for Core Temperature Estimation and Health Monitoring," *IEEE Trans. Control Syst. Technol.,* vol. 21, pp. 1745-1755, 2013.

[71] X. Lin, "Adaptive Estimation of Thermal Dynamics and Charge Imbalance in Battery Strings," Ph.D Thesis, The University of Michigan, Ann Arbor, United States, 2014.

[72] H. Gualous, H. Louahlia-Gualous, R. Gallay, and A. Miraoui, "Supercapacitor Thermal Modeling and Characterization in Transient State for Industrial Applications," *IEEE Trans. Ind. Appl.,* vol. 45, pp. 1035-1044, 2009.

[73] C. Park and A. K. Jaura, "Dynamic Thermal Model of Li-Ion Battery for Predictive Behavior in Hybrid and Fuel Cell Vehicles," 2003.

[74] J. Pyrhonen, T. Jokinen, and V. Hrabovcova, *Design of Rotating Electrical Machines*: Wiley, 2009.

[75] T. Jokinen and J. Saari, "Modelling of the coolant flow with heat flow controlled temperature sources in thermal networks [in induction motors]," *IEE Proceedings - Electric Power Applications,* vol. 144, pp. 338-342, 1997.

[76] Z. Kolondzovski, P. Sallinen, and A. Arkkio, "Thermal analysis of a high-speed PM machine using numerical and thermal-network method," in *Electrical Machines (ICEM), 2010 XIX International Conference on*, 2010, pp. 1-6.

[77] M. Chen, J. Gao, Z. Kang, and J. Zhang, "Design Methodology of Large-Scale Thermoelectric Generation: A Hierarchical Modeling Approach," *J. Thermal Science Eng. Applications,* vol. 4, pp. 041003-041003, 2012.

[78] "Maxwell K2 Series Ultracapacitors Datasheet," ed: Maxwell Technologies.

[79] "User Manual for 125 V Modules," ed: Maxwell Technologies.

[80] F. P. Incropera, *Fundamentals of heat and mass transfer*: John Wiley, 2007.

[81] J. H. Lienhard, *A heat transfer textbook*: Prentice Hall PTR, 1981.

[82] K. Youngki, S. Mohan, J. B. Siegel, A. G. Stefanopoulou, and D. Yi, "The Estimation of Temperature Distribution in Cylindrical Battery Cells Under Unknown Cooling Conditions," *IEEE Trans. Control Syst. Technol.,* vol. 22, pp. 2277-2286, 2014.

[83] J. Lustbader, "Thermal Evaluation of a High-Voltage Ultracapacitor Module for Vehicle Applications," presented at the Advanced Capacitor World Summit, San Diego, CA, 2008.

[84] X. Li, F. He, and L. Ma, "Thermal management of cylindrical batteries investigated using wind tunnel testing and computational fluid dynamics simulation," *J. Power Sources,* vol. 238, pp. 395-402, 9/15/ 2013.

[85] C. Forgez, D. Vinh Do, G. Friedrich, M. Morcrette, and C. Delacourt, "Thermal modeling of a cylindrical LiFePO4/graphite lithium-ion battery," *Journal of Power Sources,* vol. 195, pp. 2961-2968, 5/1/ 2010.

[86] Y. A. Çengel, "Appendix 1: Property Tables and Charts (SI Units)," in *Introduction to Thermodynamics and Heat Transfer*, 2 ed: McGraw-Hill, 2008.

[87] C.-T. Chen, *Linear System Theory and Design*, 3rd ed.: Oxford University Press, 1999.

[88] B. N. Datta, "Numerical Methods for Linear Control Systems - Design and Analysis," ed: Elsevier.

[89] N. S. Nise, *Control Systems Engineering*: Wiley, 2010.

[90] L. Lezhang, W. Le Yi, C. Ziqiang, W. Caisheng, L. Feng, and W. Hongbin, "Integrated System Identification and State-of-Charge Estimation of Battery Systems," *IEEE Trans. Energy Convers.,* vol. 28, pp. 12-23, 2013.

[91] G. L. Plett, "Extended Kalman filtering for battery management systems of LiPB-based HEV battery packs: Part 3. State and parameter estimation," *J. Power Sources,* vol. 134, pp. 277-292, 8/12/ 2004.

[92] D. Linzen, S. Buller, E. Karden, and R. W. De Doncker, "Analysis and evaluation of charge-balancing circuits on performance, reliability, and lifetime of supercapacitor systems," *IEEE Trans. Ind. Appl.,* vol. 41, pp. 1135-1141, 2005.

[93] S. Leleu, H. Abou-Kandil, and Y. Bonnassieux, "Piezoelectric actuators and sensors location for active control of flexible structures," *IEEE Trans. Instrum. Meas.,* vol. 50, pp. 1577-1582, 2001.

[94] H. K. Mathews and L. C. Kammer, "Reliability-Driven Sensor Selection via Observability Indices," in *American Control Conf.*, 2007, pp. 3715-3720.

[95] Q. Junjian, S. Kai, and K. Wei, "Optimal PMU Placement for Power System Dynamic State Estimation by Using Empirical Observability Gramian," *IEEE Trans. Power Systems,* vol. 30, pp. 2041-2054, 2015.

[96] L. DeVries and D. A. Paley, "Observability-based optimization for flow sensing and control of an underwater vehicle in a uniform flowfield," in *2013 American Control Conference*, 2013, pp. 1386-1391.

[97] N. J. Higham, M. Konstantinov, V. Mehrmann, and P. Petkov, "The sensitivity of computational control problems," *IEEE Control Systems,* vol. 24, pp. 28-43, 2004.

[98] V. Mehrmann and H. Xu, "An analysis of the pole placement problem II. The multi-input case," *Electronic Transactions on Numerical Analysis,* vol. 5, pp. 77-97, 1997.

[99] J. W. Demmel, "On condition numbers and the distance to the nearest ill-posed problem," *Numerische Mathematik,* vol. 51, pp. 251-289, 1987.

[100] C. Moler, "Chapter 10. Eigenvalues and Singular Values," in *Numerical Computing with MATLAB*, ed: The MathWorks, 2008.

[101] Q. Wang, P. Ping, X. Zhao, G. Chu, J. Sun, and C. Chen, "Thermal runaway caused fire and explosion of lithium ion battery," *J. Power Sources,* vol. 208, pp. 210-224, 6/15/ 2012.

[102] P. E. Ross, "Boeing's battery blues [News]," *IEEE Spectrum,* vol. 50, pp. 11-12, 2013.

[103] M. Debert, G. Colin, G. Bloch, and Y. Chamaillard, "An observer looks at the cell temperature in automotive battery packs," *Control Eng Pract.,* vol. 21, pp. 1035-1042, 8// 2013.

[104] June 2014). Corrosion, Shedding, and Internal Short Circuit. Available: http://batteryuniversity.com/learn/article/corrosion_shedding_and_internal_short

[105] N. Tudoroiu and K. Khorasani, "Satellite fault diagnosis using a bank of interacting Kalman filters," *IEEE Trans. Aerosp. Electron. Syst.,* vol. 43, pp. 1334-1350, 2007.

[106] N. Meskin, E. Naderi, and K. Khorasani, "A Multiple Model-Based Approach for Fault Diagnosis of Jet Engines," *IEEE Trans. Control Syst. Technol.,* vol. 21, pp. 254-262, 2013.

[107] T. E. Menke and P. S. Maybeck, "Sensor/actuator failure detection in the Vista F-16 by multiple model adaptive estimation," *IEEE Trans. Aerosp. Electron. Syst.,* vol. 31, pp. 1218-1229, 1995.

[108] R. Jifeng and X. R. Li, "Variable-Structure Multiple-Model Approach to Fault Detection, Identification, and Estimation," *IEEE Trans. Control Syst. Technol.,* vol. 16, pp. 1029-1038, 2008.

[109] A. Izadian and P. Famouri, "Fault Diagnosis of MEMS Lateral Comb Resonators Using Multiple-Model Adaptive Estimators," *IEEE Trans. Control Syst. Technol.,* vol. 18, pp. 1233-1240, 2010.

[110] V. L. Bageshwar and F. Borrelli, "On a Property of a Class of Offset-Free Model Predictive Controllers," *IEEE Trans. Autom. Control,* vol. 54, pp. 663-669, 2009.

[111] K. R. Muske and T. A. Badgwell, "Disturbance modeling for offset-free linear model predictive control," *J. Process Control,* vol. 12, pp. 617-632, 8// 2002.

[112] G. Pannocchia and J. B. Rawlings, "Disturbance models for offset-free model-predictive control," *AIChE Journal,* vol. 49, pp. 426-437, 2003.

[113] M. R. Rajamani, J. B. Rawlings, and S. J. Qin, "Achieving state estimation equivalence for misassigned disturbances in offset-free model predictive control," *AIChE Journal,* vol. 55, pp. 396-407, 2009.

[114] P. D. Hanlon and P. S. Maybeck, "Multiple-model adaptive estimation using a residual correlation Kalman filter bank," *IEEE Trans. Aerosp. Electron. Syst.,* vol. 36, pp. 393-406, 2000.

[115] P. S. Maybeck and P. D. Hanlon, "Performance enhancement of a multiple model adaptive estimator," *IEEE Trans. Aerosp. Electron. Syst.,* vol. 31, pp. 1240-1254, 1995.

[116] M. Kuure-Kinsey and B. W. Bequette, "Multiple Model Predictive Control Strategy for Disturbance Rejection†‡," *Ind. Eng. Chem. Res.,* vol. 49, pp. 7983-7989, 2010/09/01 2010.

[117] (April 2014). *A123 32157 Lithium Ion Battery Specification.* Available: http://www.a123rc.com/goods-474-

High+Quality+Original+Lithium+Ion+Battery+LiFePO4+Battery+(A123+32157).html

[118] W. Fang, P. Ramadass, and Z. Zhang, "Study of internal short in a Li-ion cell-II. Numerical investigation using a 3D electrochemical-thermal model," *Journal of Power Sources,* vol. 248, pp. 1090-1098, 2/15/ 2014.

[119] Z. Li, J. Zhang, B. Wu, J. Huang, Z. Nie, Y. Sun, *et al.*, "Examining temporal and spatial variations of internal temperature in large-format laminated battery with embedded thermocouples," *J. Power Sources,* vol. 241, pp. 536-553, 11/1/ 2013.

[120] M. S. K. Mutyala, J. Zhao, J. Li, H. Pan, C. Yuan, and X. Li, "In-situ temperature measurement in lithium ion battery by transferable flexible thin film thermocouples," *J. Power Sources,* vol. 260, pp. 43-49, 8/15/ 2014.

[121] B. Chaudhuri, R. Majumder, and B. C. Pal, "Application of multiple-model adaptive control strategy for robust damping of interarea oscillations in power system," *IEEE Trans. Control Syst. Technol.,* vol. 12, pp. 727-736, 2004.

[122] J. Gertler, *Fault Detection and Diagnosis in Engineering Systems*: Taylor & Francis, 1998.

[123] J. Barros and E. Perez, "Automatic Detection and Analysis of Voltage Events in Power Systems," *IEEE Trans. Instrum. Meas.,* vol. 55, pp. 1487-1493, 2006.

[124] Z. Tao, M. Woodside, and M. Litoiu, "Performance Model Estimation and Tracking Using Optimal Filters," *IEEE Trans. Softw. Eng.,* vol. 34, pp. 391-406, 2008.

[125] Z. Pingping, C. Badong, and J. C. Principe, "Learning Nonlinear Generative Models of Time Series With a Kalman Filter in RKHS," *IEEE Trans. Signal Process.,* vol. 62, pp. 141-155, 2014.

[126] M. E. Salgado and A. Conley, "MIMO interaction measure and controller structure selection," *Int. J. Cont.,* vol. 77, pp. 367-383, 2004/03/10 2004.

[127] C. Himpe and M. Ohlberger, "A Note on the Cross Gramian for Non-Symmetric Systems," *arXiv preprint arXiv:1501.05519,* 2015.

[128] H. R. Shaker and J. Stoustrup, "An interaction measure for control configuration selection for multivariable bilinear systems," *Nonlinear Dynamics,* vol. 72, pp. 165-174, 2013.

[129] K. V. Fernando and H. Nicholson, "On the structure of balanced and other principal representations of SISO systems," *IEEE Trans. Autom. Cont.,* vol. 28, pp. 228-231, 1983.

[130] J. Huber, H. Kopecek, and M. Hofbaur, "Sensor selection for fault parameter identification applied to an internal combustion engine," in *Cont. Appl. (CCA), 2014 IEEE Conf.*, 2014, pp. 89-96.

[131] F. L. Cortesi, T. H. Summers, and J. Lygeros, "Submodularity of energy related controllability metrics," in *Decision Cont. (CDC), 2014 IEEE 53rd Annual Conf.*, 2014, pp. 2883-2888.